UNIVERSITY OF CALIFORNIA, SAN DIEGO

Structural Design of Non-Structural Components:

Modified Electrodes for Thermal Runaway Mitigation of Lithium-Ion Battery

A dissertation submitted in partial satisfaction of the

requirements for the degree Doctor of Philosophy

in

Structural Engineering

by

Anh Vu Tu Le

Committee in charge:

Professor Yu Qiao, Chair
Professor Olivia A. Graeve
Professor Hyunsun Alicia Kim
Professor Francesco Lanza Di Scalea
Professor Ying Shirley Meng

2017

The dissertation of Anh Vu Tu Le is approved, and it is acceptable in quality and form for publication on microfilm and electronically:

_____

_____

_____

_____

_____

Chair

University of California, San Diego

2017

DEDICATION

To my family.

TABLE OF CONTENTS

LIST OF ABBREVIATIONS

EV	Electric vehicle
LIB	Lithium-ion battery
TRM	Thermal-runaway mitigation
CDI	Cracking/debonding initiator
TSB	Thermally sensitive binder
AM	Active material
NMC	Lithium nickel manganese cobalt oxide
AG	Artificial graphite
CB	Carbon black (conductive additive)
AM:B:CB	Mass ratio among the solid components of the electrode, i.e. active material : binder : carbon black.
PVDF	Poly(vinylidene fluoride)
PVDF-HFP	Poly(vinylidene fluoride -co- hexafluoropropylene)
CNT	Carbon nanotubes
MWCNT	Multiwall carbon nanotube
EC	Ethylene Carbonate
EMC	Ethyl Methyl Carbonate

LIST OF SYMBOLS

M_W	Molecular weight
m_i	initial mass of polymer sample
m_g	mass of polymer gel, dried from pipetted solution
m_d	mass of dissolved polymer portion
$D,\%$	weight percentage of dissolved polymer, m_d , with respect to m_i
m_p	mass of undissolved polymer portion
m_{sw}	mass of swollen polymer portion remaining in the 'sample unit'
m_u	initial mass of the sample 'unit,' with polymer sample
$m_{u,ref}$	initial mass of the sample 'unit,' without polymer sample
SI	Swelling index
R_d	Resistance of the electrode stack, oven-dried
R_c	Resistance of the electrode stack, compressed
R_s	Resistance of the electrode stack, compressed, soaked in EMC
R_i	Resistance of the electrode stack, after impact
R_I	Internal Ohmic resistance of coin cell
ΔH_f	Heat of fusion

LIST OF FIGURES

LIST OF TABLES

ACKNOWLEDGEMENTS

I would like to acknowledge Professor Yu Qiao for his support as my supervisor. His guidance is invaluable.

I would also like to acknowledge the help from my teammates in the Multifunctional Materials Research Laboratory, who supported me in an immeasurable way.

This research is funded by the Advanced Research Projects Agency–Energy (ARPA-E). We are also grateful to our collaborators , Professor Y. Shirley Meng and her research group (University of California, San Diego), Dr. Jiang (John) Fan and Dr. Dengguo Wu (American Lithium Energy Corp.), Professor Xi Chen (Columbia University), and Professor Yanbao Ma (University of California, Merced).

Chapters 1, in part, is reproduced from Journal of Applied Physics 118, 2015. Le, Anh; Wang, Meng; Shi, Yang; Noelle, Daniel; Qiao, Yu; Lu, Weiyi. “Effects of additional multiwall carbon nanotubes on impact behaviors of LiNi0. 5Mn0. 3Co0. 2O2 battery electrodes.” AIP Publishing LLC, 2015; with the permission of AIP Publishing. The dissertation author was the primary investigator and author of this paper.

Chapters 1, in part, is reproduced from Journal of Physics D: Applied Physics 48, 2015. Le, Anh V.; Wang, Meng; Shi, Yang; Noelle, Daniel; Qiao, Yu. “Heat generation of mechanically abused lithium-ion batteries modified by carbon black micro-particulates.” © IOP Publishing. Reproduced with permission. All rights reserved. The dissertation author was the primary investigator and author of this paper.

Chapter 1, in part, is reproduced from the under-review manuscript. Le, Anh V.; Wang, Meng; Shi, Yang; Noelle, Daniel J.; Yoon, Hyojung; Meng, Ying S.; Wu, Dengguo; Fan, Jiang; Qiao, Yu. "Heat Generation of Mechanically Abused Lithium-Ion Battery Cell Based on Thermally Sensitive Cathode Binder."The dissertation author was the primary investigator and author of this manuscript.

Chapters 2, in part, is reproduced from Journal of Applied Physics 118, 2015. Le, Anh; Wang, Meng; Shi, Yang; Noelle, Daniel; Qiao, Yu; Lu, Weiyi. "Effects of additional multiwall carbon nanotubes on impact behaviors of LiNi0. 5Mn0. 3Co0. 2O2 battery electrodes." AIP Publishing LLC, 2015; with the permission of AIP Publishing. The dissertation author was the primary investigator and author of this paper.

Chapters 2, in part, is reproduced from Journal of Physics D: Applied Physics 48, 2015. Le, Anh V.; Wang, Meng; Shi, Yang; Noelle, Daniel; Qiao, Yu. "Heat generation of mechanically abused lithium-ion batteries modified by carbon black micro-particulates." © IOP Publishing. Reproduced with permission. All rights reserved. The dissertation author was the primary investigator and author of this paper.

Chapter 2, in part, is reproduced from the under-review manuscripts: (1) Le, Anh V.; Wang, Meng; Shi, Yang; Noelle, Daniel J.; Yoon, Hyojung; Meng, Ying S.; Wu, Dengguo; Fan, Jiang; Qiao, Yu. "Heat Generation of Mechanically Abused Lithium-Ion Battery Cell Based on Thermally Sensitive Cathode Binder;" (2) Le, Anh V.; Wang, Meng; Noelle, Daniel J.; Shi, Yang; Yoon, Hyojung; Zhang, Minghao; Meng, Ying S.; Qiao, Yu.

"Effects of Macromolecular Configuration of Thermally Sensitive Binder in Lithium Ion Battery." The dissertation author was the primary author of these manuscripts.

Chapters 3, in part, is reproduced from Journal of Applied Physics 118, 2015. Le, Anh; Wang, Meng; Shi, Yang; Noelle, Daniel; Qiao, Yu; Lu, Weiyi. "Effects of additional multiwall carbon nanotubes on impact behaviors of LiNi0. 5Mn0. 3Co0. 2O2 battery electrodes." AIP Publishing LLC, 2015; with the permission of AIP Publishing. The dissertation author was the primary investigator and author of this paper.

Chapters 3, in part, is reproduced from Journal of Physics D: Applied Physics 48, 2015. Le, Anh V.; Wang, Meng; Shi, Yang; Noelle, Daniel; Qiao, Yu. "Heat generation of mechanically abused lithium-ion batteries modified by carbon black micro-particulates." © IOP Publishing. Reproduced with permission. All rights reserved. The dissertation author was the primary investigator and author of this paper.

Chapter 4, in part, is reproduced from the under-review manuscripts: (1) Le, Anh V.; Wang, Meng; Shi, Yang; Noelle, Daniel J.; Yoon, Hyojung; Meng, Ying S.; Wu, Dengguo; Fan, Jiang; Qiao, Yu. "Heat Generation of Mechanically Abused Lithium-Ion Battery Cell Based on Thermally Sensitive Cathode Binder;" (2) Le, Anh V.; Wang, Meng; Noelle, Daniel J.; Shi, Yang; Yoon, Hyojung; Zhang, Minghao; Meng, Ying S.; Qiao, Yu. "Effects of Macromolecular Configuration of Thermally Sensitive Binder in Lithium Ion Battery." The dissertation author was the primary author of these manuscripts.

Chapter 4, in part, is currently being prepared for submission for publication of the material: (1) Le, Anh V.; Wang, Meng; Noelle, Daniel J.; Shi, Yang; Meng, Ying S.; Qiao,

Yu. “Mitigating Thermal Runaway of Lithium-ion Battery by Using Thermally Sensitive Binder;” (2) Le, Anh V.; Chung, Hyeseung; Wang, Meng; Noelle, Daniel J.; Shi, Yang; Yoon, Hyojung; Meng, Ying S.; Qiao, Yu. “Effects of Electrode Composition on Lithium-ion Battery Based on Thermally Sensitive Binder.” The dissertation author was the primary investigator and author of these manuscripts.

Chapter 5, in parts, is currently being prepared for submission for publication of the material: Le, Anh V.; Chung, Hyeseung; Wang, Meng; Noelle, Daniel J.; Shi, Yang; Yoon, Hyojung; Meng, Ying S.; Qiao, Yu. “Effects of Electrode Composition on Lithium-ion Battery Based on Thermally Sensitive Binder.” The dissertation author was the primary investigator and author of this material.

VITA

2012 Bachelor of Science, University of Illinois at Urbana-Champaign

2014 Master of Science, University of California, San Diego

2017 Doctor of Philosophy, University of California, San Diego

PUBLICATIONS

Le, A.V., Wang, M., Shi, Y., Noelle, D., Qiao, Y. and Lu, W., 2015. Effects of additional multiwall carbon nanotubes on impact behaviors of LiNi0. 5Mn0. 3Co0. 2O2 battery electrodes. *Journal of Applied Physics*, *118*(8), p.085312.

Le, A.V., Wang, M., Shi, Y., Noelle, D.J. and Qiao, Y., 2015. Heat generation of mechanically abused lithium-ion batteries modified by carbon black micro-particulates. *Journal of Physics D: Applied Physics*, *48*(38), p.385501.

Le, A.V., Wang, M., Shi, Y., Noelle, D.J., Yoon H., Meng, Y.S., Wu, D., Fan, J. and Qiao, Y. Heat Generation of Mechanically Abused Lithium-Ion Battery Cell Based on Thermally Sensitive Cathode Binder. *Under Review.*

Le, A.V., Wang, M., Noelle, D.J., Shi, Y., Yoon H., Zhang, M., Meng, Y.S. and Qiao, Y. Effects of Macromolecular Configuration of Thermally Sensitive Binder in Lithium Ion Battery. *Under Review.*

Le, A.V., Wang, M., Noelle, D.J., Shi, Y., Meng, Y.S. and Qiao, Y. Mitigating Thermal Runaway of Lithium-ion Battery by Using Thermally Sensitive Binder. *Currently being prepared.*

Le, A.V., Chung, H., Wang, M., Noelle, D.J., Shi, Y., Yoon H., Meng, Y.S. and Qiao, Y. Effects of Electrode Composition on Lithium-ion Battery Based on Thermally Sensitive Binder. *Currently being prepared.*

Wang, M., Le, A.V., Noelle, D.J., Shi, Y., Yoon, H., Zhang, M., Meng, Y.S. and Qiao, Y., 2016. Effects of electrode pattern on thermal runaway of lithium-ion battery. *International Journal of Damage Mechanics*, p.1056789516660176.

Wang, M., Le, A.V., Shi, Y., Noelle, D.J., Yoon, H., Zhang, M., Meng, Y.S. and Qiao, Y., 2016. Effects of angular fillers on thermal runaway of lithium-ion battery. Journal of Materials Science & Technology, 32(11), pp.1117-1121.

Wang, M., Le, A.V., Shi, Y., Noelle, D.J., Wu, D., Fan, J., Lu, W. and Qiao, Y., 2017. Sigmoidal current collector for lithium-ion battery. Journal of Applied Physics, 121(1), p.015303.

Shi, Y., Noelle, D.J., Wang, M., Le, A.V., Yoon, H., Zhang, M., Meng, Y.S. and Qiao, Y., 2016. Exothermic behaviors of mechanically abused lithium-ion batteries with dibenzylamine. *Journal of Power Sources*, *326*, pp.514-521.

Shi, Y., Noelle, D.J., Wang, M., Le, A.V., Yoon, H., Zhang, M., Meng, Y.S. and Qiao, Y., 2016. Role of Amines in Thermal-Runaway-Mitigating Lithium-Ion Battery. ACS Applied Materials & Interfaces, 8(45), pp.30956-30963.

Qiao, Y., Lu, W., Shi, Y. and Lee, A., The Regents of The University of California, 2014. Mitigating thermal runaway in lithium ion batteries using damage-initiating materials or devices. U.S. Patent Application 14/893,893.

ABSTRACT OF THE DISSERTATION

Structural Design of Non-Structural Components:

Modified electrodes for Thermal-Runaway Mitigation of Lithium-Ion Battery

by

Anh Vu Tu Le

Doctor of Philosophy in Structural Engineering

University of California, San Diego, 2017

Professor Yu Qiao, Chair

In recent years, as the automotive industry is shifting towards electric vehicles (EVs), lithium-ion battery (LIB) has attracted increasing attention for its high

energydensity, relatively long cycle life, and relatively low cost per kW-h. In a LIB cell, under normal operating condition, the polymer membrane separator hosts the electrolyte for lithium ion transport between the anode and the cathode, while blocking the internal electron transport. However, such a membrane structure is point sensitive and may be damaged under extreme conditions, leading to internal shorting and thermal runway.

To mitigate thermal runaway of LIB cells, robust composite electrodes with either cracking/debonding initiation (CDI) additives or thermally sensitive binders (TSBs) were systematically investigated. Both of the thermal-runaway mitigation (TRM) mechanisms were integrated into the active electrode layer. When a battery was internally shorted, TRM process was activated, which disintegrated the components of electrode and limited the discharge current and Joule heating rate, preventing the cell from reaching the onset temperature of thermal runaway. The CDI was triggered mechanically, and the TSB was triggered thermally.

The testing results suggested that TSB was more effective than CDI; it reduced the peak temperature increase in a damaged LIB cell by approximately 50%. The triggering temperature was around 100 ^{o}C, conservatively lower than the onset of thermal runaway. The TSB mechanism was also tested for compatibility with high-energy battery chemistries and demonstrated promising results.

CHAPTER 1 - INTRODUCTION

1.1. BACKGROUND AND SIGNIFICANCE

1.1.1. ELECTRIC VEHICLE (EV)

Conventional internal combustion engine (ICE) vehicles have been widely used for over 100 years. However, the exhaust of various pollutants, including carbon monoxide (CO), unburned hydrocarbons (HC), and nitrogen oxides (NO_x), has raised increasing concern (Abdel-Rahman, 1998). With a rapid increase in world population, global warming, and constraints on energy resources, there have been more stringent regulations on the fuel economy. For instance, in 2016, the U.S. Energy Information Administration (EIA) reported that transportation is among the two energy-related sectors with the largest carbon dioxide (CO_2) emission, which led to an increase in the stringency of fuel economy and Green House Gas (GHG) emission standards for both light vehicles and heavy trucks (Khaligh & Li, 2010). As a result, electric vehicle (EV), hybrid electric vehicle (HEV), plug-in hybrid electric vehicle (PHEV), and fuel cell vehicle (FCV) have attracted more and more attention from the governments, automakers, and customers (Chan, 2007).

Among various types of electric vehicles, battery-powered electric vehicle (BEV) exhibits a number of advantages: zero emission, high energy efficiency, independence on crude oils, and commercial readiness. There are still a few major issues, however, before BEV can be more successful on the market: relatively short range, high initial cost, battery management, and charging facilities (Chan, 2007). Moreover, recent Life Cycle Analyses (LCAs) revealed that 'materials production' was a main contributor to CO_2 emissions and

energy costs for EVs (Larcher & Tarascon, 2015). A ‘greener and more sustainable’ battery is feasible with (1) the development of eco-efficient synthesis processes of inorganic compounds; (2) the promotion of ‘green chemistry’ using natural sources to synthesize organic-compounds for renewable electrodes; and (3) the new technologies beyond Li-ion such as Li-S, Li-air, Na-ion and redox flow systems (Larcher & Tarascon, 2015).

1.1.2. Energy Storage Systems (ESS) for EV

The EV industry has investigated several energy storage systems such as lead-acid battery, nickel metal hydride (NiMH) battery, lithium-ion battery (LIB), Ni-Zn, Ni-Cd, etc. Among these systems, lead–acid battery technology is most mature, which has been implemented for more than 50 years. However, there are several limitations, including low cycle life at deep discharge and low power density (Olson & Sexton, 2000; Edwards & Kinney, 2001). NiMH battery is another common ESS. NiMH batteries have twice the amount of energy density compared to that of lead-acid batteries and may be operated in a wide temperature and voltage windows. They are environmentally friendly and can be recycled. However, the major issues of NiMH system are the memory effect and the low rate capability (Viera, et al., 2006). Nickel-Cadmium (Ni-Cd) batteries have long cycle life and little memory effect even with deep charge-discharge cycles. While the specific energy density is quite high, there is still concern over the high cost and environmental issue over disposal (Gao & Ehsani, 2002; Viera, et al., 2006).

Ni–Zn and Li-ion batteries show considerable potential to replace NiMH systems (Khaligh & Li, 2010). Over the past decade, several active researches have geared towards

developing battery technologies beyond lithium-ion, such as Li-S, Li-Air and Na-ion. However, these technologies are still in their infantry (Luntz, 2015).

1.1.3. Lithium Ion Battery: Advantages and Disadvantages

The promise of Li-ion battery (LIB) lies in its high specific energy, wide power range, and excellent cost-performance balance, enabling its use in various applications ranging from Watt-hours to Megawatt-hours (Larcher & Tarascon, 2015). For instance, Li-ion batteries have shown high specific energy of 100-250 Wh/kg (Panasonic, 2011), long battery life of 1000 cycles (Chalk & Miller, 2006), 3-5 times higher specific power than that of existing NiMH battery (EnerDel Corporation, 2005), and the ability to go up to 4,990 W/kg in an instant pulse (100-C rate) (Green Car Congress, 2005).

There are still several remaining problems for LIB before it can be more broadly deployed, among which a major issue is fire safety. It is critical that reliability and safety issues related to handling, storage, and operation of batteries can be resolved (Scrosati & Garche, 2010). Specifically, thermal runaway must be mitigated. The focus of this study is to develop internal thermal-runaway mitigation (TRM) mechanisms in LIB cells.

1.1.4. Thermal runaway

Lithium-ion battery offers high energy density. For instance, a commercial Li-ion battery can store up to 160 Wh/kg, which is roughly twice that of an alkaline battery or a Ni-Cd rechargeable battery (St. John, 2016). However, when it is coupled with flammable organic electrolyte, new challenges have arisen regarding the storage and handling of LIB systems. Even though the probability of lithium battery failure is low, only around 1 in 5-

10 million, the failure mode can be highly destructive in an uncontrolled manner (Orendorff, , et al., 2011). Recent massive product recalls of portable notebook computer and cell phone batteries have increased public awareness for battery safety (Mikolajczak, et al., 2012).

Thermal runaway is defined as "rapid self-heating of a cell derived from the exothermic chemical reaction of the highly oxidizing positive electrode and the highly reducing negative electrode" (Mikolajczak, et al., 2012). It is usually a three-stage process: (i) First, anodic reaction starts at around 90 °C, with decomposition of the solid-electrolyte interface (SEI) at 120 °C, temperature increase causing the breakdown of the organic solvents in electrolyte, and releasing flammable hydrocarbon gases. (ii) In the second stage, exothermic reactions at the positive electrode start as the temperature rises over 140 °C, and oxygen rapidly evolves. (iii) Finally, the positive electrode decomposes, releasing oxygen that enables aggressive burning of both the electrolyte and the gases present inside the cell, causing fire and/or even explosion (Lisbona & Snee, 2011). Thermal runaway can occur with any battery chemistry, as the cell to releases the stored energy in an uncontrolled rate (Mikolajczak, et al., 2012). The higher energy, the more heat would be generated and the more dangerous the reactions may be.

The three main components of a LIB cell are the positive electrode (cathode), the negative electrode (anode), and the electrolyte. To store a large amount of energy, the cathode is normally made with lithium metal oxides, in which the valence bonds between the oxygen and the metal components are relatively weak and easily broken, releasing O_2. Differential scanning calorimetry (DSC) has shown that high-energy-density lithium cobalt

oxide (LCO) starts to decompose at a temperature as low as 150 ^{o}C(Lawson, 2005). The decomposition reaction of the cathode material is highly exothermic, leading to excessive self-heating (~100 ^{o}C/min) and pressure build-up in the battery cell.(Lisbona & Snee, 2011; Golubkov, et al., 2014)

Another issue associated with thermal runaway is the release of toxic fluoro-organic compounds resulting from the reactions between the electrolyte and the unprotective cathode materials. This poses a risk to larger lithium-ion battery systems, such as EV battery packs (Hammami, et al., 2003).

1.2. Lithium-Ion Battery (LIB)

1.2.1. Battery cell components and electrochemistry

As lithium-ion technology is advancing rapidly, new developments of materials and cell configuration have been proposed to meet various system requirements for a broad range of consumer electronics and industrial applications. Figure 1.1, adapted from (Templeton, 2015), shows the three main components of battery cell which remain unchanged: cathode, anode and electrolyte. In the charged state, lithium ions are stored in the anode. During discharge, lithium ions are transported internally from anode to cathode via an organic electrolyte stored in a porous membrane separator. At the same time, electrons flow externally from the current collector of the anode to the current collector of the cathode, generating electrical energy to power the external device. (Automotive Energy Supply Corporation (AESC) , 2013).

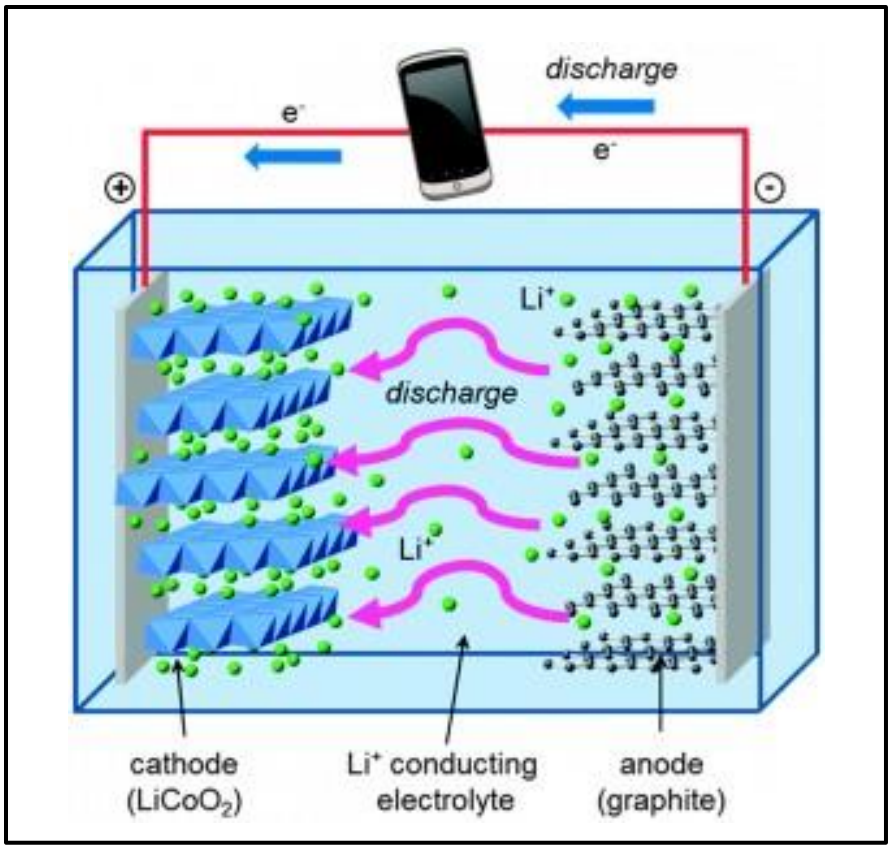

Figure 1.1. Lithium-ion battery mechanism.

For each electrode, the component that participates in the electrochemical reaction to produce lithium ions is referred to as the "active material." The active material (AM) is commercially available in powder form. The AM particles are bound together by a polymer binder, forming a porous particulate composite, which is often referred to as active layer, or anode/cathode, respectively. To improve the electrical conductivity of active layer, some conductive additives, most often carbon black (CB) nanopowders, may be added. The active layer is coated on a current collector, which is a copper (Cu) foil for anode and an aluminum (Al) foil for cathode. (Daniel, 2008; Osiak, et al., 2014)

For anode, the most common active material is graphite. Recently, there has been tremendous research effort to incorporate silicon into the system. Because silicon allows three-dimensional lithium insertion, silicon anode can store a significantly higher amount of energy compared to graphite anode. However, for the same reason, it is also much more vulnerable to mechanical stresses due to excessive volume expansion and contraction associated with the lithiation and de-lithiation processes, respectively. Other anode chemistries such as titanium oxides, tin and other metal oxides, are still in development stage. (Goriparti, et al., 2014) The active anode material used in this study was artificial graphite, EQ-Lib-CMSG, with the particle size ~ 20 μm, obtained from MTI Corp(MTI Corp., 2013, b).

Lithium-ion batteries are often categorized per the cathode chemistry, or the active material of the positive electrode. For high-energy applications, such as energy storage system for EVs, lithium-metal oxides are often employed. The metal component may be nickel, manganese, cobalt, or a combination thereof, as these materials have good lithium insertion/intercalation properties(He, et al., 2012). While Lithium Cobalt Oxide (LCO) is the original commercial type, cobalt is an expensive material, and LCO is the most thermally unstable active material below 200 ^{o}C(Lawson, 2005). Commercial Lithium Iron Phosphate (LFP) offers high power and safest battery chemistry, as the oxygen valence bond is much more stable than that of the metal oxides at high temperature (Takahashi, et al., 2005). However, the energy density of LFP is much lower than other available materials. With economy, energy, and safety being taken into consideration, our study employed a Lithium Nickel Manganese Cobalt Oxide (NMC), NCM-04ST as the cathode

active material. The composition of this material was $LiNi_{0.5}Mn_{0.3}Co_{0.2}O_2$ and its average particle size was ~ 10 μm. The material was obtained from TODA America (Le, et al., 2015, a, b). This material was later referred to as NMC532.

1.2.2. INTERNAL SHORTING: INITIATION, PROCESS, RESULT

As discussed above, thermal runaway is a major safety concern for any LIB system. The catastrophic event is often initiated by internal shorting, in which the two opposite electrodes come into direct contact. Internal shorting may be caused by overcharging, overheating, mechanical abuse, poor cell design, etc. or a combination thereof (Mikolajczak, et al., 2012).

In a working battery cell, a porous polymer membrane is sandwiched between the anode and the cathode, preventing direct contact and blocking internal electron transport between the two opposite electrodes. This cell component is referred to as the membrane separator, hosting and allowing the electrolyte to carry lithium ions back and forth between the two electrodes during normal charge and discharge cycles of the battery (Mikolajczak, et al., 2012). If this separator is broken, the electrons are free to move directly from anode to cathode within the battery cell. This phenomenon is referred to as internal shorting. Because both electrodes are electronically conductive, the internal shorting leads to a large current flow within the battery cell, rapidly releasing a large amount of heat. The Joule heating "plays a key role in initiating the temperature rise at the point of short" (Santhanagopalan, et al., 2009). As the cell temperature reaches ~ 175^{o}C, a series of

exothermic reactions among the cell components are initiated one after another, leading to excessive heat generation.

1.2.3. Factors that influence heat generation.

The severity of the thermal runaway a LIB cell depends upon many factors such as state of charge (SOC), ambient environmental temperature, battery chemistry, additives, and mechanical design of the cell (size, electrolyte volume, packaging, etc.). (Mikolajczak, et al., 2012)

Battery chemistry plays a critical role in heat generation in a short circuit (Brand, et al., 2013). Studies on different cell chemistrieshave revealed that the higher energy density of the active material, the higher heating rate is. The heat generation rate is also related to the cell size, which is attributed to lower amount of heat dissipated to the environment. For instance, at 2-3 Ah/cell, the normalized heating rate of a NCA type battery is about two times greater than that of a LFP-type battery; as the capacity increases to 30-40 Ah/cell, the difference is ten times greater (Orendorff, et al., 2016). Differential Scanning Calorimetry (DSC) and Thermal Gravimetric Analysis (TGA) have shown that oxygen release from charged cathode materials plays a significant role in the safety performance of lithium-ion batteries (Binotto, et al., 2011). Not only that the decomposition of the cathode active material is highly exothermic, the oxygen released from this process reacts with the electrolyte, generating more heat and gaseous products at accelerated rate (Kim, et al., 2007). This oxygen release that could lead to cell eruption is a major problem for all lithium metal oxide chemistries, especially for high-energy NMC

and NCA. High-energy-density NCA poses higher risk of thermal runaway compared to NMC, due to its higher oxygen release potential in charged state (Binotto, et al., 2011). For instance, regardless of the cell size, the normalized total heat release (kJ/Ah) in a LFP cell is approximately 15 % less than that in a NCA cell (Orendorff, et al., 2016).

On the one hand, regardless of the electrochemistry of battery cell, the normalized total released heat (kJ/Ah) is relatively constant for varied cell sizes, as the generated heat comes directly from the stored energy. On the other hand, normalized heating rate (W/Ah) increases approximately linearly with cell capacity within the 3-38 Ah range (Orendorff, et al., 2016). This is attributed to the lower heat dissipation rate in larger cells.

The nature of internal shorting is an important parameter, because the conductivity of short contributes directly to the Joule heating - the main source of heating that raises the cell temperature during the initial stage of thermal runaway (Santhanagopalan, et al., 2009). This factor is somewhat difficult to evaluate, because the damage level in a short circuit is usually of a far greater scale compared to the thickness of each electrode layer. The results may vary depending on different assumptions. In general, the most severe short heating may be observed when direct contact is established between the active anode material and the aluminum current collector of cathode, or between the copper and aluminum current collectors of the two opposite electrodes (Santhanagopalan, et al., 2009). This is attributed to the fact that electrons are readily available in a fully charged anode material, and the shortest internal conductive path for electron transport is through the aluminum current collector on the cathode side. In addition, as the size of puncture, or the shorted area,

increases, the heating rate would rise, due to the larger amount of participating materials (Keyser & Kim, 2011).

1.3. Problem Statement and Hypotheses

1.3.1 Mechanically triggered thermal-runaway-mitigation mechanism

1.3.1.1 Crack initiation and propagation in particulate composites

Barsoum and Wang (1992) proposed that "matrix cracking is precipitated by randomly distributed micro-flaws in the microstructure". In other words, visible macro-cracks are initiated via interactions between micro-flaws and local matrix(Barsoum, et al., 1992; Wang, et al., 1992). For a particulate-reinforced polymer composite, microcracks can be initiated only if a nucleation stress exceeds the critical value, approximately equal to Young's modulus of the polymeric binder. The particles act as stress concentration sites, and thus failure is expected to occur at the filler-matrix interface (Sahu & Broutman, 1972). Once initiated, the cracks can propagate through the polymer matrix and along the matrix–particle interface, and may be accelerated by external stresses (Matouš, 2003).

Broberg (1968) proposed the concept of Essential Work of Fracture, considering two different zones: the inner/process zone and the outer/plastic zone. The total amount of work involved (W_f) is assumed to be dissipated within the two regions. W_f is expressed as the summation of the essential work (W_e) and non-essential work (W_p) of fracture. (Broberg, 1968).

$$W_f = W_e + W_p \quad (1)$$

$$W_e = w_e l t \quad (2)$$

$$W_p = w_p \beta l^2 t \quad (3)$$

where W_e is related to the instability of the crack tip and the vicinity from which actual fracture process is initiated; its magnitude is proportional to the polymer ligament section, lt, with l denoting the length of the ligament and t the thickness of the specimen; $w_e$denotesthe specific essential work of fracture per unit surface area. W_p is associated with the work involved in deformation of the material in the surrounding plastic zone. Its value is proportional to the volume of the plastic zone, $\beta l^2 t$, where $w_p$denotes the specific essential work of fracture per unit volume and β is a system parameter Martinez, et al., 2009)(Arencón & Velasco, 2009; Martinez, et al., 2009)

Per theoretical bases, the ability of crack growth in the particulate composite electrode is limited by the polymer matrix and the interfacial adhesion with the main particulate component. For a commercial LIB electrode, the content of the active material takes up most the electrode's mass (over 90 wt.%), while the contents of binder and conductive additive are much smaller (MTI Corp., 2013, c; Singh, et al., 2015). The distribution of the polymer – conductive carbon black network among the active material particles plays a critical role in crack initiation and propagation, bringing to our attention that the introduction of a cracking/debonding initiation (CDI)additive into the electrode may alter the electrode microstructure. While this may be more beneficial to activate cracking-debonding safety mechanism, it may also bring about negative effects on the electrochemical performance of the battery cell, both of which must be carefully investigated.

1.3.1.2 Concept of Cracking/Debonding Initiator (CDI)

Even though lithium-ion technology is prone to thermal runaway due to its high-energy density, the probability is still relatively low. For small cell sizes as the ones in portable electronic devices, the damage is usually not severe. The major concern is focused on large-sized battery systems, such as energy storage in transportation, grid, and military systems. Especially when used in electric vehicle, the risk of thermal runaway becomes higher due to extensive vibrations, shocks, and in the worst-case scenario, vehicle collision (Hollmotz & Hackmann, 2011; SAE International, 2013). (Wilson, 2013)

A cracking/debonding initiator (CDI) works asa thermal-runaway mitigation(TRM) mechanism to solve the problem of mechanical abuse. The idea is to introduce additional micro-particles into the composite electrode, so that micro-cracks may be initiated and propagate through the electrode from the “micro-flaws” upon impact, breaking off the contact between the active material particles and the conductive binder-carbon black network. It is a mechanically triggered battery shutdown mechanism.

1.3.1.3 Key parameters for material selection

Even though the main objective of the CDI is to mechanically damage the electrode when impact occurs, it is critical to ensure that the introduction of such particles into the system does not bring any detrimental effect to the electrochemical performance of the battery. The material selection is narrowed down to carbon and silicon based materials, which have already been added to lithium-ion battery systems as additives (Etacheri, et al., 2011).

The key role of the CDI particles is to act as the stress concentrators to initiate cracking and debonding. The effect of stress concentration depends on the geometry of the particles, as well as the relative properties of these particles with respect to the electrode matrix (Arencón & Velasco, 2009). Therefore, particle size and shape, mechanical strength, adhesion with polymer binder, etc. must be considered. In regard of the CDI particle shape and size, both the macro-geometry of the composite electrode layer and the micro-geometry of the active material particles need to be accounted for. For instance, carbon based materials can be rod-like, round, or angular, of either low or high surface area (Table 1.1). Within the scope of this project, the electrodes of NMC532 are about 50-100 μm thick (Singh, et al., 2015), and the particle size of the active material is 10-20 μm. Hence, the size of the CDI particles should be around 30-80 μm, large enough to act as stress concentration sites and small enough to be well embedded within the electrode layer. With the geometry of CDI particles being taken as a factor, the CDI particle size will be narrowed down to 45-50 μm.

Once initiated, crack propagation is influenced by the interaction among the binder and the AM particles. To promote widespread crack growth, the microstructure of the electrode may be slightly altered, as the CDIs have different levels of interaction with the binder during electrode processing. Key parameters include surface areasand surface properties (Table 1.1).

Table 1.1.CDI Candidates

Criteria				Solid Filler	Supplier, Product no.	Additional Solid Wt.%
Matrix Materials	Form	Surface Area (m^2/g)*	Surface Condition			
Silica	Particles	80-120	Hydrophobic, hydrophilic (treated)	TNM-b	JLK Industries/ PP-35-HP-HS-18	3, 5
	Particles	600-800	Hydrophobic	Aerogel	Cabot Corp./ ENOVA ® IC3100	3
Carbon	Particles	600	Hydrophilic	FGD	Cabot Corp./DARCO ® FGD	3
	Particles	1500	Hydrophilic	BP2000	Cabot/Black Pearls ® 2000	3
	Nanotubes	-	Hydrophilic	MWCNT	Cheap Tubes/ SKU-030102	3, 5
	Nanotubes	-	Hydrophilic	SWCNT	Cheap Tubes/ SKU-010109	3
	Particles, round	1400	Hydrophilic, hydrophobic	CGR	Cabot Corp./ Norit ® C Gran	1, 3, 5
	Particles, sharp	1700	Hydrophilic	KBG	Cabot Corp./ DARCO ® KB-G	1, 3, 5

* *The data are from JLK Industries*, *Cabot Corp.*, (J Carpenter Environmental, LLC., 2013), (Wang, et al., 2010), (da Silva & Faria, 2003) *and* (Pacific Rim Oenology Services, 2007).

1.3.2 THERMALLY TRIGGERED THERMAL-RUNAWAY-MITIGATION MECHANISM

1.3.2.1 POSITIVE THERMAL COEFFICIENT (PTC) MATERIALS

For the past few decades, several safety mechanisms have been proposed for LIB, including safety vents, thermal fuses, and other circuit breakers (Balakrishnan, et al., 2006). Among these, positive thermal coefficient (PTC) materials/devices received wide attention, as they eliminate the inconvenience of installation and replacement, as well as the problem of premature failure. As the temperature rises, the electrical resistance of a PTC material/device increases drastically and interrupts the short current (Brice, et al., 1996). To optimize the response time, the PTC material can be coated either between the current collector and the active electrode layer or directly on the particles of the active material (Baginska, et al., 2012; Xia, et al., 2012; Zhong, et al., 2012). In these thermally responsive system, the triggering temperature may also be adjusted (Chen, et al., 2016). Due to the high heating rate in a short circuit, PTC system should have a relatively low triggering temperature, i.e. below the boiling point of electrolyte (~120 ^{o}C). However, the challenge for a low-temperature triggering point is that it may disrupt the charge flow during normal operation. While most current electric vehicles are equipped with thermal management system to maintain the internal temperature of battery below 55 ^{o}C(Pesaran, 2001), it is always desirable to have a higher range of operating temperature.

The PTC devices/materials still have major limitations. Two main types of PTC materials are ceramics and conductive polymers. While the ceramic-based PTC devices are limited by high electrical resistance and sluggish response, the conductive polymer PTC

devices are limited by their low tolerance with high current and high voltage (Balakrishnan, et al., 2006). The challenge is to develop a PTC system which can respond fast enough without any reduction in the electrochemical performance of the battery for high current and/or high voltage applications.

1.3.2.2 Concept of thermally sensitive binder (TSB)

Poly(vinylidene-fluoride) (PVDF) is the most commonly used binder material in LIB cathode. PVDF has excellent adhesion, strength, compatibility with high-voltage electrochemical reactions, and processability with solvents and active material (Yoshio, et al., 2009). In a few special cases, e.g. plastic lithium-ion batteries (PLiON^{TM}), poly(vinylidene fluoride-co-hexafluoropropylene) (PVDF-HFP) is favored as a hosting material for electrolyte, since it absorbs more electrolyte than PVDF and thus, increases the ionic conductivity (Stephan, 2006). Compared to PVDF, PVDF-HFP contains a larger amount of amorphous phase; its strength and thermal stability are lower, especially with the presence of electrolyte. Consequently, polymer binder in a regular LIB electrode tends to have a low HFP content, and may be treated to enhance the binding strength (Ameduri, 2009). In general, battery manufacturers and scientists do not use PVDF-HFP as the main component of binder, but rather often incorporate it into membrane separator, with a relatively low HFP content, i.e. less than 15 wt.% of the polymer (Wensley & Chambers, 2010). PVDF-HFP membranes have been investigated for thermal-runaway mitigation in LIB system. The intended working mechanism was based on the low melting point of PVDF-HFP, which can close the pores as the local temperature reaches a set point (Zhang, 2007). However, under severe mechanical abuses, rupture of the membrane separator is

inevitable. For the sake of conservation, we must assume that the positive and negative electrodes will eventually be in direct contact. More efficient approaches should be employed to increase the internal impedance around the damaged electrode areas, which motivated us to develop the technology of thermally sensitive binder (TSB).

One of the major issues of the current PTC technology for thermal-runaway mitigation is that, to introduce the PTC additives into the electrodes, the manufacturing procedure of LIB must be adjusted, which challenges the industrial engineering and the quality control, as well as increases the cost.In this study, we demonstrate that, instead of using PTC additives, the binder phase of LIB electrode can be thermally sensitive, by using a relatively small amount of PVDF-HFP. The slurry processing is similar to the conventional procedure, and the cell mass does not increase; i.e. the specific energy remains the same. Thermally sensitive binder (TSB) is designed to fail at elevated temperature (~110 ^{o}C) and disintegrate the electrode components. In another word, it is a thermally triggered thermal-runaway mitigation (TRM) mechanism. As the internal impedance rises, the short current is reduced and the heat generation is slowed down.

1.3.2.3 KEY PARAMETERS FOR MATERIAL SELECTION

Because the main objective of TSB is to mitigate the Joule heating effect in a short circuit, thermal sensitivity is a critical parameter. Upon impact, Joule heating will quickly raise the temperature of the cell to ~150 ^{o}C within 10-30 seconds, after which thermal runaway takes off(Doh, et al., 2008; Roth & Orendorff, 2012). During thermal runaway, self-heating rate may be as high as 150-200 ^{o}C/min, and the heat mainly generated from

vigorous chemical reactions among the internal components (Lawson, 2005; Roth & Orendorff, 2012). Once the battery has already reached the stage of thermal runaway, it becomes difficult for any safety mechanism to take effect. Therefore, TSB system must be triggered before the 150 ^{o}C -onset mark. In addition, it should still be well above the operating temperature window of battery, i.e. below 55 ^{o}C(Pesaran, 2001). As a result, a temperature window of 80-120 ^{o}C is desirable.

Because TSB is an integrated component of the electrode, it is critical to ensure that it does not affect the normal cycling operation of the battery. PVDF has been long developed for used as binder for cathode materials, thanks to its excellent electrochemical stability and bonding strength (Zhang, et al., 2014). The glass transition temperature (T_g) of PVDF, associated with the relaxation of the secondary bonds, is in the range of -40 to –30 ^{o}C; and the melting temperature (T_m) of its crystalline phase is between 155 and 192 °C, depending on the molecular weight (M_W), defects, and testing method (Ameduri, 2009). Therefore, if used, PVDF must be combined with another polymer component to enhance the overall thermal sensitivity of the binder.

For compatibility, simplicity in processing, and economical reasons, the material selection is limited to VDF-based polymers. In fact, many polymers of this group have been investigated for use in LIB cells, either as membrane separators or as binders. For instance, Samsung SDI (2015) filed a patent on a graft polymer based on poly(VDF-co-chlorotrifluoroethylene), or PVDF-co-CTFE, as binder in electrode (Park, et al., 2014). The polymer is derived from Kureha #7500 PVDF-co-CTFE as the backbone with added side groups. The invention aimed to improve the electrode performance at high voltage(Park,

et al., 2014). While the material appears to be compatible with the LIB environment, it is not a TSB, as its melting point is 160-170 ^{o}C.

Among a wide range of available VDF-based polymers, there are a number of polymers with thermal transition points within the target temperature window 80-120 ^{o}C.Dyneon offers several commercial fluoroplastic products with suitable transition temperatures. Dyneon ET 6235 and Dyneon 6500 series possess glass transition temperature (T_g) of 90^{o}C and 100 ^{o}C, respectively (3M, 2003). The flexural moduli of these polymers are over 550 MPa, more than twice compared with ~200 MPa of conventional PVDF binder (Quantum Advanced Engineering Plastics, 2009). This will be a major challenge to industrial cell assembly process, which requires folding of electrode films into multiple layers or rolls (Yeow, et al., 2012). Other options include Dyneon THV 220 (Teng, 2012), Kynar 2500 (Quantum Advanced Engineering Plastics, 2009), PiezoTech's Poly(vinylidene-co-Fluoride Tri-Fluoroethylene), and P(VDF-TrFE)(PiezoTech, 1993; Alves, et al., 1998).

Dyneon THV is a commercial fluorinated thermoplastic terpolymer oftetrafluoroethylene ($F_2C = CF_2$), hexafluoropropylene ($F_2C = CF–CF_3$), and vinylidene ($H_2C=CF_2$) or poly(TFE-co-HFP-co-VDF). Especially, Dyneon THV 220 satisfies the requirement for transition temperature (T_m = 120 ^{o}C) and processability, as it is soluble in polar organic solvents and can easily form thin films by solution casting (Teng, 2012). This product has been discontinued (3M, 2016).

Kynar 2500 is a PVDF-HFP supplied by Arkema. Since PVDF-HFP has been integrated into a number of LIB systems, the material is potentially compatible with the battery environment. Kynar 2500 is a block copolymer of VDF and HFP units (Ma, et al., 2014). The presence of atactic HFP units increases the irregularity, limiting the formation of ordered configuration and rendering the copolymer highly amorphous and the melting point lower than that of PVDF homopolymer(Ma, et al., 2014). The amorphous domain which is capable of storing a large amount of electrolyte was the main reason why this material was an attractive candidate for membrane separator (Sivakumar, et al., 2013). Kynar 2500 possesses a low melting point at 117 ^{o}C, thanks to its high HFP content (Quantum Advanced Engineering Plastics, 2009)

PiezoTech's P(VDF-TrFE) is a ferroelectric and piezoelectric copolymer, available in different compositions: 50/50, 70/30 and 77/23 mol.% (VDF/TrFE)(Alves, et al., 1998). Disregarding the different compositions and thermal treatments, primary melting always occurs at ~150 ^{o}C. A secondary endothermic phase transition occurs between 80-130 ^{o}C. The magnitude of heat absorption during this transition is small, and thus, it is difficult to compare among different compositions. Regardless, the transition appears to be more gradual with a lower initiation temperature at a higher TrFE content. With a 70/30 VDF/TrFE ratio, a solvent-cast sample shows a defined endothermic peak at ~100 ^{o}C(Alves, et al., 1998), which meets the requirement for TSB. However, the magnitude of the transition is only about 10% of that of the major melting event. When the content of the binder is less than 5wt% of the total mass of the AM composite layer(MTI Corp., 2013, c; Singh, et al., 2015), it may not be sufficient to shut down the electrode reactions.

In the scope of this study, PVDF and PVDF-HFP with different M_W and HFP contents were investigated (Table 1.2). Upon identifying a polymer candidate that shows most effective heat mitigation effect, the cycling performance of the battery cell was tested. Different modification methods were also implemented to improve the cycling performance, according to necessity.

Table 1.2. TSB Candidates

Supplier/ Product Number	Polymer type	Molecular Weight*, M_W (g/mol)	Melting Temperature *, T_m (°C)	HFP Content ** (wt.%)	Nick name
Sigma-Aldrich #182702	PVDF	~534,000 by G.P.C.	171	0	B01
Arkema/ Kynar 710 (Sigma-Aldrich # 427152)		~180,000 by G.P.C.	165 - 172		B02
Arkema/ Kynar 2501-20	PVDF-HFP	~500,000 by G.P.C.	117 - 125	32	B03
Arkema/ Kynar 2801-00		-	140 - 145	24	B04
Arkema/ Kynar 3120-50		-	161 - 168	10	B05

* *The data are from Sigma-Aldrich and Quantum Advanced Engineering Plastics.*
** *The data are from* (Neese, 2009) *and* (Terasawa, et al., 2011).

1.4. SUMMARY OF STUDY

Chapter II describes the general experimental procedure, including an experimental flowchart. A detailed description is provided for each step of the experimental process, i.e.

sample preparation, testing and material characterization. This procedure applied to both the Cracking/Debonding Initiator (CDI) and Thermally Sensitive Binder (TSB) systems.

Chapter III discusses theCracking/Debonding Initiator (CDI) mechanism, starting from material selection and treatment. We investigated the effects of the CDI matrix material, particle's geometry, surface area and surface property on heat mitigation effect via blunt impact and nail penetration tests. We also studied the effect of the CDI content on electrochemical performance of the battery, which in turns limited the effectiveness of the CDI mechanism in blunt impact and nail penetration tests.

Chapter IV discusses the Thermally Sensitive Binders (TSB). First, we performed preliminary study to select the baseline TSB material. Then, we investigated different modification techniques for the baseline material to improve the battery cell's cycling performance. Finally, we optimized the electrode composition based on the modified TSB material.

Chapter V discusses the compatibility of the optimized TSB system with high-energy materials and the performance of the TSB-modified high energy cell in nail penetration test.

Chapter VI gives a summary of the current study, discusses the limitations of each system and plans for future work.

ACKNOWLEDGEMENT

This research is supported by the Advanced Research Projects Agency – Energy (ARPA-E) under Grant No. DE-AR0000396, for which we are grateful to Dr. Ping Liu, Dr. John Lemmon, Dr. GrigoriiSoloveichik, Dr. Chris Atkinson, and Dr. Dawson Cagle. Special thanks are also due to Dr. Jiang Fan and Dr. Dengguo Wu for the help with lithium-ion battery design and processing.

Chapters 1, in part, is reproduced from Journal of Applied Physics 118, 2015. Le, Anh; Wang, Meng; Shi, Yang; Noelle, Daniel; Qiao, Yu; Lu, Weiyi. "Effects of additional multiwall carbon nanotubes on impact behaviors of LiNi0. 5Mn0. 3Co0. 2O2 battery electrodes." AIP Publishing LLC, 2015; with the permission of AIP Publishing. The dissertation author was the primary investigator and author of this paper.

Chapters 1, in part, is reproduced from Journal of Physics D: Applied Physics 48, 2015. Le, Anh V.; Wang, Meng; Shi, Yang; Noelle, Daniel; Qiao, Yu. "Heat generation of mechanically abused lithium-ion batteries modified by carbon black micro-particulates." © IOP Publishing. Reproduced with permission. All rights reserved. The dissertation author was the primary investigator and author of this paper.

Chapter 1, in part, is reproduced from the under-review manuscript. Le, Anh V.; Wang, Meng; Shi, Yang; Noelle, Daniel J.; Yoon, Hyojung; Meng, Ying S.; Wu, Dengguo; Fan, Jiang; Qiao, Yu. "Heat Generation of Mechanically Abused Lithium-Ion Battery Cell Based on Thermally Sensitive Cathode Binder."The dissertation author was the primary investigator and author of this manuscript.

CHAPTER 2–EXPERIMENTAL PROCEDURES

2.1. SAMPLE PREPARATION

2.1.1. ELECTRODE PROCESSING

For the positive electrode, active material (AM) was chosen as $LiNi_{0.5}Mn_{0.3}Co_{0.2}O_2$ (NMC532) (NCM-04ST from TODA America), with an average particle size of 10-20 μm. The reference binder (B) was polyvinylidene fluoride (PVDF), with the molecular weight, M_w, of 534,000 by G.P.C.The reference binder is referred to as B01 in this study (Table 1.2). A variety of Cracking/Debonding Initiator (CDI) candidates (Table 1.1) and vinylidene fluoride (VDF) -based thermally sensitive binder (TSB) candidates (Table 1.2) were investigated. The conductive additive was carbon black (CB) nanoparticles (CNERGY-C65 from TIMCΛL). The weight ratio among AM, binder, and CB was 93:4:3, or AM:B:CB = 94:4:3, typical for lithium-ion battery (LIB) coin cells. For the CDI-modified LIB cell, the additional amount of CDI is by wt.% with respect to the total mass of the AM:B:CB mixture, as listed in Table 1.1. For the TSB-based LIB cell, the same composition, i.e. AM:B:CB = 93:4:3, was first used for preliminary study to identify the baseline material performance and to evaluate different modification methods; and then varied compositions were examined to optimize the thermal-runaway mitigation (TRM) effectiveness.

To process reference cathodes, 5 g of solid components, i.e. AM, B, CB (with an appropriate amount of CDI if applicable), were manually ground and mixed in a set of agate mortar for 45 min. The mixture was transferred to a 10-mL beaker, and 2 mL of N-

Methyl-2-pyrrolidone (NMP) (Product No. 328634 from Sigma-Aldrich) was added. In the preliminary electrode testing stage (Figure 2.1), slurry mixing was performed with a mechanical stirrer obtained from IKA, Inc.(Le, et al., 2015, a). Later, in coin cell testing stage (Figure 2.1), slurry mixing was performed with a Qsonica Q55 ultrasonic processor for about 10 min. To avoid overheating, the mixing was interrupted after every 1 minute and the solution was cooled down in air for 2 minutes(Le, et al., 2015, b).

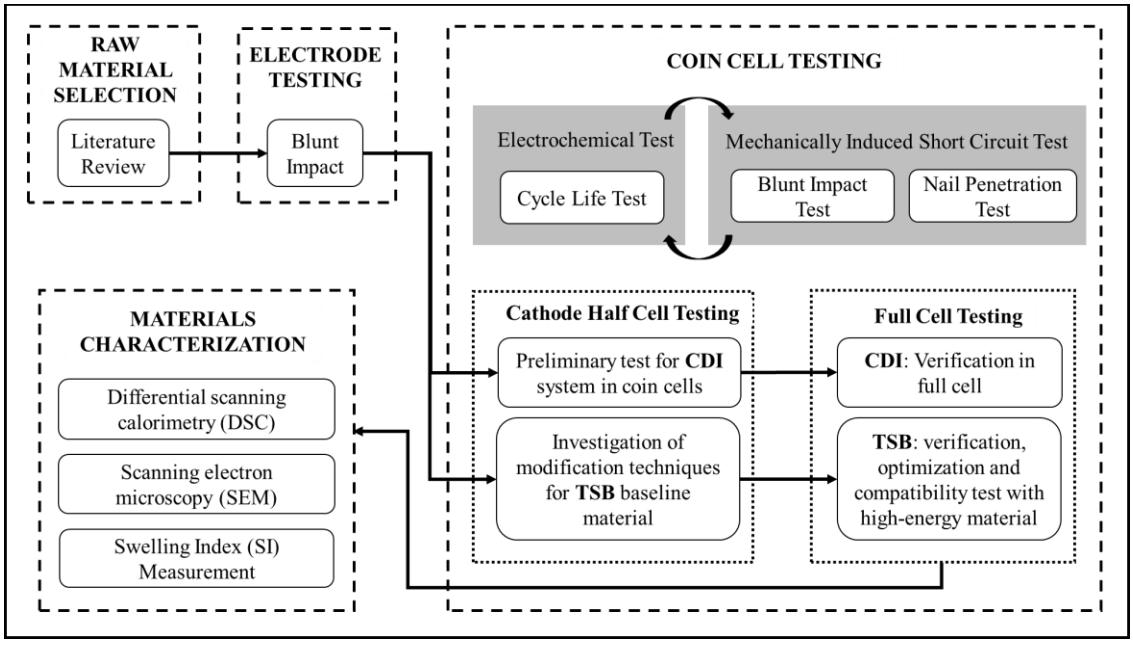

Figure 2.1. Flowchart of our work.

For the negative electrode, or anode, the active material (AM) was artificial graphite (AG) powders (EQ-Lib-CMSG from MTI). The anode binder was a blend of carboxymethyl cellulose (CMC) and styrene butadiene rubber (SBR), with the CMC to SBR mass ratio of 2:2. The SBR was obtained from MTI (Product Code EQ-Lib-SBR). The carboxymethyl cellulose sodium salt (CMC-Na) was obtained from Sigma-Aldrich (Product Code 1001817659). The CMC-SBR binder is commonly used in commercial LIB

cells. The mass ratio among the solid components was AM:B:CB = 95:4:1. For anodes with the CMC/SBR binder, the slurry processing followed the one established by MTI (MTI Corp., 2013, d), using deionized water as solvent.

PVDF, which is more commonly used in laboratory testing, was also tested as the binder in anode in this study for comparison purpose. The PVDF binder for anode was Kynar HSV 900, obtained from Arkema. This polymer was chosen for its high molecular weight, which was expected to "provide improved adhesion with reduced loading when utilized as a binder in electrode formulation" (Arkema, 2016). The mass ratio among the solid components was AM:B:CB = 93:6:1. The anode slurry with PVDF binder was prepared through a similar procedure as for the cathode slurry.

Casting of wet slurries was performed by using a doctor blade, and the slurry was dried at 80 ^{o}C in vacuum for 24 h. For both anode and cathode, the initial slurry thickness was either 50 μm (for cycle life testing) or 200 μm (for nail penetration testing). After drying, the film thicknesses were reduced to 20-25 μm and 100-110 μm for thin and thick electrodes, respectively.

For testing of mechanical properties of electrodes, the dried films were sandwiched by two flat stainless steel plates with smooth surfaces, compressed, and held at desired pressure for 30 sec by an Instron-5582 machine. The compressive pressures were 15 MPa and 30 MPa for anode and cathode films, respectively. The compressed films were cut into 1 cm -by- 1 cm squares(Le, et al., 2015, a). It served as a fast and convenient method for baseline material selection for the large number of possible CDI and TSB candidates.

For coin cell testing, the dried slurry was compressed by a hardened steel double roller to enhance the contact among the AM particles and the binder-CB conductive matrix, as well as to strengthen the bonding between active material layer and the current collector, following a standard industrial procedure (MTI Corp., 2013, a). The condensed electrode film was cut into circular disks with the diameter of 14.3 mm. A full battery cell contained a cathode and an anode. The active material mass was 8-10 mg for a thin cathode, or 30-35 mg for a thick cathode.The theoretical capacities of the anode and cathode AMs were 338.6 and 153.0mAh/g at first cycle, respectively (MTI Corp., 2013, b, c). The slurry processing was adjusted to achieve the AG mass in anode about 50% of the NMC532 in the matching cathode, so that the theoretical capacities of the two electrodes were compatible with each other.

2.1.2. CELL FABRICATION

Cell fabrication was performed in an Argon-filled glove box (MBraunLABstar MB10/ 14-150). The moisture level of the glovebox was maintained under 0.5 ppm. All equipment and coin cell components, including electrodes and membrane separator were vacuum dried at 80 ^{o}C for 12 hours prior to transferring into the glovebox.

For a full cell, a pair of positive electrode and negative electrode were placed in a standard set of CR2016 coin cell case (Xiamen Tob, product no. T-2016), separated by a 25-µm-thick porous PP/PE/PP tri-layer membrane separator (Celgard, product no. 2325). For impact test, the active cell components were secured by set of stainless steel spacer and spring, obtained from MTI Corp. (product codes EQ-CR20-Spacer304-02 and EQ-

CR20WS-Spring304AL, respectively). For nail penetration test, the active cell components were secured by a nickel foam, 14.3 mm in diameter and 1.6 mm in thickness (MTI Corp.,product code EQ-bcnf-16m). Finally, sufficient BASF SelectiLyte-LP50 EC/EMC electrolyte was added (Le, et al., 2015, b).

Cathode half-cells were produced through a similar procedure as the full cells, except that in the final cell assembly, the AG anode was replaced by a lithium disk with the diameter of 15.4 mm and the thickness of 1.1 mm, without any spacer or spring(Le, et al., 2015, b).

2.1.3. PRE-CONDITIONING

After the cell had been assembled, it was at rest for 24 h under ambient condition. All cells were first charged and discharged for one cycle between 4.3-3.0 V at 0.1C using an MTI BST8-3 Battery Analyzer. Low charging-discharging rate during the initial cycle helped establish more uniform and stable solid-electrolyte interface (SEI) (An, et al., 2016).

After the initial cycle, LIB cells with thicker electrodes (~ 30-35 mg of NMC532) for mechanical abuse testing, i.e. blunt impact or nail penetrations, were cycled between 4.2-3.0 V at 0.5 C for 5 times, and finally charged to 4.6 V at 0.1 C (Figure 2.2). The final capacity was approximately 5 mAh/cell. Immediately after charging, there would be a slight voltage drop from 4.6 V to 4.50-4.52 V, which was observed for both reference and TSB-based cells. At rest, stable cell voltage was maintained at 4.50-4.52 V for at least 3 hours. The cells were then pre-heated on a hot plate for 1 minute to reach 110 ^{o}C (Figure 2.2). After pre-heating, they were air-cooled to room temperature, after which the voltage

would maintain constant at 4.42-4.46 V for at least 10 minutes. Typical cycling-charging and pre-heating profiles of reference coin cell and TSB-modified coin cell are shown in Figure 2.2(Le, et al., To be published, a).

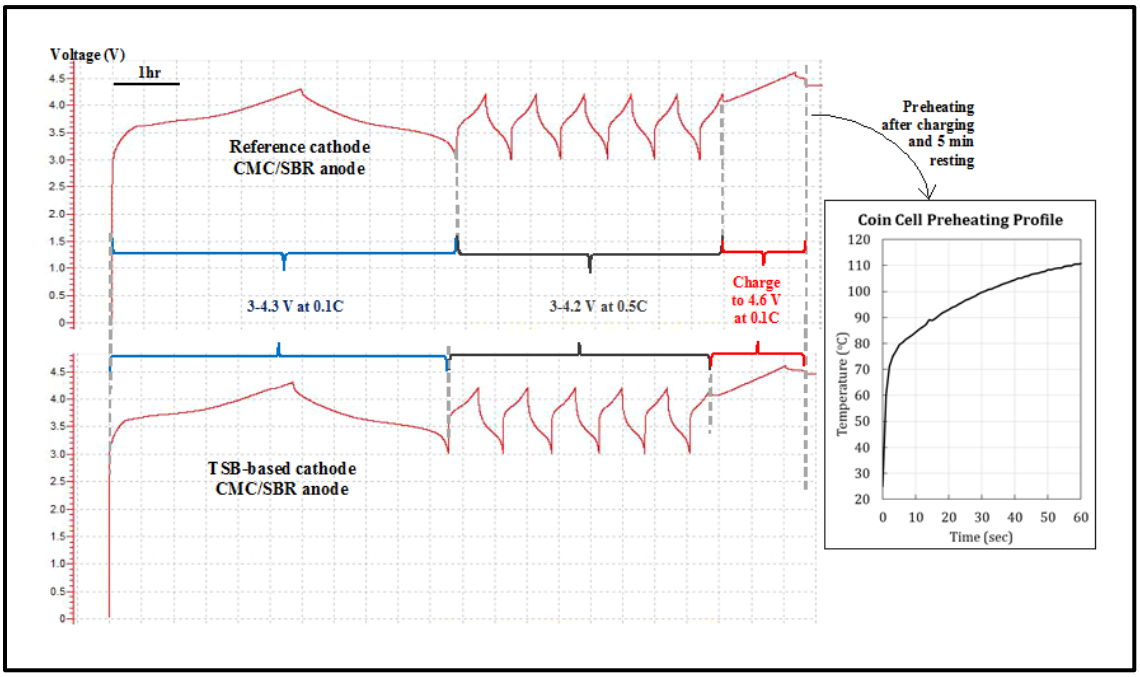

Figure 2.2. Typical pre-cycling – charging – pre-cycling profiles of coin cells.

2.2. Coin Cell Testing

2.2.1. Cycling performance measurement

After the initial pre-conditioning cycle, cells of thinner electrodes were tested for electrochemical performance in an MIT BST8-3 Battery Analyzer. For preliminary study, as for the TSB baseline material selection, 20 cycles were sufficient to show the binder performance. Cycle life test was also performed at elevated temperature, i.e. 60 ^{o}C, to speed up aging of the cells while still ensuring safe operation (Waldmann, et al., 2014). For in-

depth study, at least 100 cycles were needed for selected cells. Additional 200 cycles were carried out to confirm the long-term cycling performance of the best CDI and TSB candidates.

2.2.2. NAIL PENETRATION TESTS

Nail penetration is a reliable method to trigger internal shorting in small LIB CR2016 coin cell (Kim, et al., 2009); it maximizes the temperature signals. Nail penetration tests were carried out on pre-cycled, fully charged and preheated LIB cells on a solid polyurethane (PU) platform as shown in Figure 2.3(Le, et al., To be published, b). The cell was firmly attached on the platform by 5 layers of insulating tapes and indented upon by a stainless-steel nail with the diameter of 1.58 mm. The nail was placed inside the PU foam, and driven through the cell by a Palmgren bench vise. An Omega TT-K-40-25 type-K gage-40 thermocouple was adhered 3 mm away from the center of the cell, connected to an Omega OM-EL-USB-TC temperature logger.

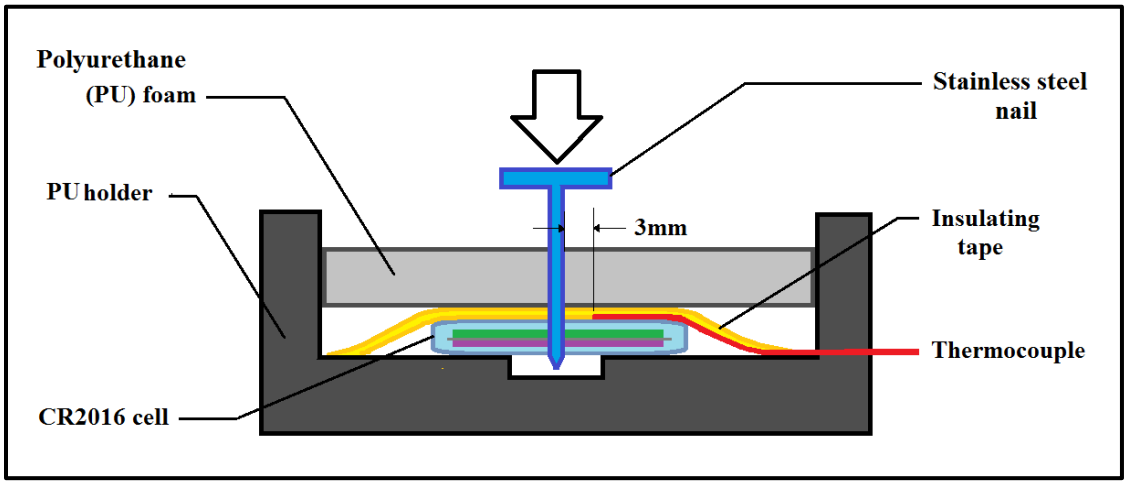

Figure 2.3. Schematic of the nail penetration test.

2.2.3. IMPACT TESTS

For preliminary study, blunt impact tests were performed on electrode stacks, each comprising 10 layers of electrode films, employed as an analogue to the layered electrode structure in LIB (Yeow, et al., 2012). The testing specimens were saturated by 200 µlof ethyl methyl carbonate (EMC), which was the solvent of the LIB's electrolyte. We measured the deceleration of the drop weight, from which the impact loading and compressive stress on the electrode sample were calculated. We also measured the resistance of the electrode at different stages of the impact test, and examined the cracking/debonding behaviors of tested samples. Both reference and CDI/TSB modified cathode and anode films were tested.

A table-top drop tower was developed (Le, et al., 2015, a). The drop tower consisted of a solid stainless steel base, a solid metal holder, and a transparent polycarbonate (PC) guiding tube. The force applied on the sample was measured by an accelerometer (ACC103, Omega, Inc.) attached to the drop weight and recorded by a high-speed digitizer (PCI-5105, National Instruments, Corp.). Due to the difference in mechanical properties between cathode and anode films, two separate impact systems with similar setup but different parameters were developed. The specifications are listed in Table 2.1 and the schematics of the experimental setups are shown in Figure 2.4(Le, et al., 2015, a). Each layer of the tested sample was observed under microscope (Section 2.3.2) and its resistance was measured (Section 2.3.4).

Table 2.1. Specification of the tabletop drop tower system.

Sample	Drop Weight Parameters				Drop Height (mm)
	Material	Mass (Kg)	Diameter (mm)	Length (mm)	
Cathode	Titanium	0.405	22.27	266	0-160 (~80)
Anode stack	Stainless Steel	7.7	620	3050	4–22 (~12)
Coin cells					160

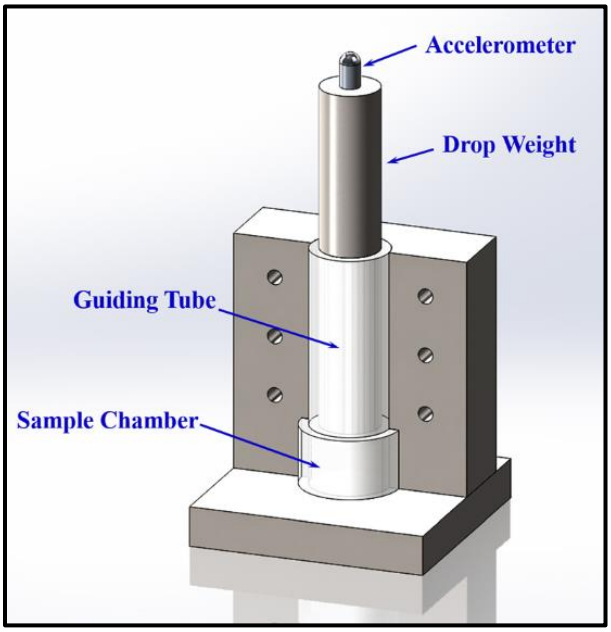

Figure 2.4. Schematic of the blunt impact test

Blunt impact tests were also performed on fully charged coin cells on the same solid PU platform as in nail penetration test (Le, et al., 2015, b). The same impact system as shown Figure 2.4 was used. A LIB coin cell was affixed on the platform by insulating tapes and indented upon by a copper spherical indenter with the diameter of 12.7 mm.

Initially, the indenter was rested on top of the battery cell, separated by 5 layers of insulating tapes. The system was insulated by a solid PU cover, which also acted as the guide for a stainless-steel rod with the diameter of 12.7 mm and the length of 50.8 mm, same as one used in the impact test of anode stack (Table 2.1). The rod was placed on top of the indenter, hosted by a rubber O-ring. The assembly was inside a stainless-steel frame with a transparent polycarbonate (PC) tube at the top, which guided a 7.7 kg stainless steel cylindrical hammer. The drop distance was 16 cm. An Omega TT-K-40-25 type-K gage 40 thermal couple was attached to the cell case, about 5.0 mm away from the center. The cell temperature was recorded by an Omega OM-EL-USB-TC temperature logger.

2.3. Materials Characterization

2.3.1. Differential Scanning Calorimetry (DSC)

Differential scanning calorimetry (DSC) analysis was conducted to characterize the polymer binders (Le, et al., To be published, c). Polymer films were prepared by the solvent casting method, using NMP as the solvent. About 2 g of polymer powder was mixed with 5 mL of NMP, forming a gel. The polymer gel was flattened to about 1 mm thick, dried in a VWR 1410 vacuum oven at 80 ^{o}C for 24 hours, air-cooled to room temperature, and cut into 6.35-mm-diameter discs. Each disc weighed approximately 10 mg, with the final thickness of about 200 μm.

Assembling of DSC sample was performed in the Argon-filled glovebox. Two groups of polymer films were investigated: dry polymer discs (Group 1) and polymer discs soaked up with electrolyte for 3 hours (Group 2). Soaking of samples was also performed

in the glovebox. After soaking, the sample mass increased by approximately 2 mg. The sample was placed in a 50 µL sealed aluminum pan.

The DSC analyses were performed with a DSC 8000 (PerkinElmer). The temperature range was 40-200 ^{o}C. The heating rate was 10^{o}C/min. An empty sealed pan, i.e with no polymer sample but only Argon gas, was used as reference.

2.3.2. Environmental Scanning Electron Microscopy (ESEM)

Environmental scanning electron microscopy helped study the microstructure of the electrodes at different stages: dried, calendared, cycled, charged, heated, and after nail/impact test. It is a useful tool to evaluate the both thermal-runaway mitigation (TRM) mechanisms, CDI and TSB.

We used a FEI/Philips XL30 ESEM, available at the CALIT2: California Institute for Telecommunication and Information Technology - Nano3 facility. All electrode samples were cut into small pieces that fit onto a 12.7-mm-diameter specimen mount (Emsdiasum, product no. 75220), and then dried in a vacuum oven at 80 ^{o}C for at least 12 hours before being observed.

2.3.3. Swelling Index Measurement

To determine the degree of dissolution and the degree of swelling of each cathode binder material in electrolyte, we performed swelling index measurement. The experimental procedure followed ASTM D3616-95 (2014), simplified to accommodate the small sample size (Figure 2.5). The polymer sample was processed using the solvent

casting method with NMP as the solvent, similar to the procedure in Section 2.3.1, except that the gel was cast at 400 μm. After drying, the final film thickness was approximately 100 μm. The film was cut into "rings" of 12.700 mm (1/2 inch) outer diameter and 3.175 mm (1/8 inch) inner diameter, weighing approximately 20 mg each. Each sample consisted of 5 "rings," with initial mass of polymer material (m_i) approximately 100 mg. The sample was sandwiched between two 12.700-mm diameter stainless steel meshes. A reference test was carried out without polymer, i.e. $m_i = 0$. The sample rack was submerged in 10 mL of electrolyte, with the initial mass of M_{EL}. The experimental apparatus, or "unit," was assembled in the Argon-filled glovebox and sealed with parafilm (Pechiney PM 996) before being transferred out for testing. The swelling index tests were performed at three different temperatures: 25, 60 and 80 ^{o}C. The testing duration was 24 hours.

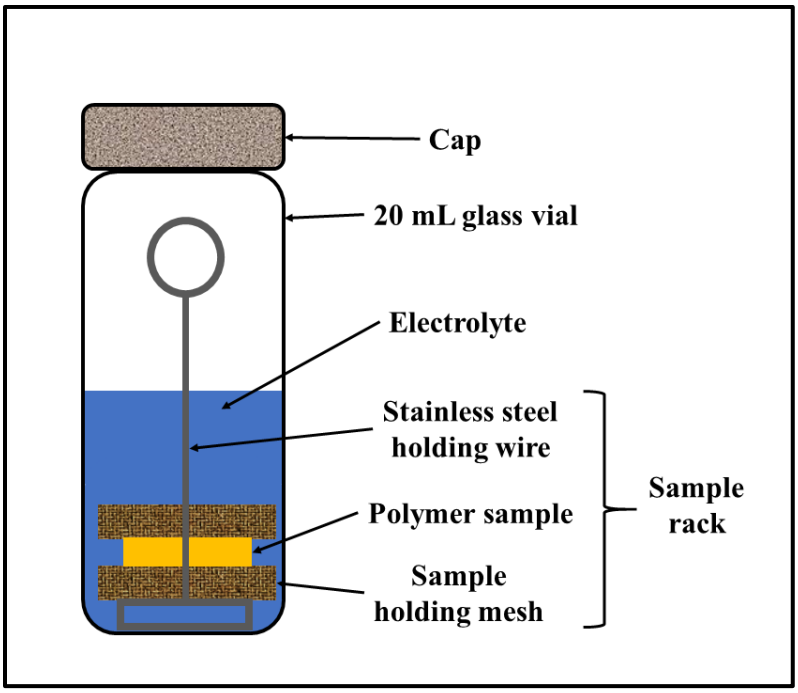

Figure 2.5. A 'sample unit' for swelling index (SI) measurement

After 24 hours, the unit was opened, and 2.5 mL of the liquid, containing electrolyte solvent and polymer solute, was pipetted out onto an Aluminum weighing dish and was vacuum dried for 24 hours. The mass of the dried gel was measured and recorded as m_g.

The mass of dissolved polymer could be calculated as:

$$m_d^{'} = 4 \times m_g , \qquad (1)$$

In which the factor 4 accounted for that only 1/4 of electrolyte was sampled for the measurement of m_g. It also came to our attention that the dried gel might have contained a non-evaporating portion of the electrolyte (i.e. ethylene carbonate, EC, and some other components). Therefore, we performed a calibration test in which the electrolyte was simply vacuum-dried at 80 ^{o}C for 24 hours, and measured a constant amount of r = 7.62 wt% solid left.

Let m_d be the actual mass of dissolved polymer and m_s be the mass of solid component of the electrolyte in the electrolyte/polymer solution. Then,

$$m_d^{'} = m_d + m_s , \qquad (2)$$

and the actual mass of the electrolyte solvent in the electrolyte/polymer solution was:

$$m_{EL}^{'} = \frac{m_s}{r} \qquad (3)$$

The mass of the undissolved polymer was:

$$m_p = m_i - m_d = m_i - m_d^{'} + m_s \qquad (4)$$

To calculate the swelling index, the solvent must be completely removed. This was done by gently washing the sample unit with fresh solvent, which was the electrolyte in our case. Then, the washing solvent was removed, and the masses of the sample containing rack and the reference empty rack were quickly measured and recorded as m_r and $m_{r,ref}$, respectively. Then, the mass of the swollen polymer sample, containing both the undissolved polymer and the solvent that entered the polymer system, was given by:

$$m_{sw} = m_r - m_{r,ref} \tag{5}$$

The mass of the electrolyte in the swollen polymer was:

$$m_{EL} = m_{sw} - m_p = m_{sw} - m_i + m_d^{'} - m_s \tag{6}$$

Because $M_{EL} = m_{EL} + m_{EL}^{'}$, we could solve for m_s from equations (3) and (6). From then, the actual mass of polymer in the dried gel, m_d, could be calculated. Then, the actual weight percentage of dissolved polymer was given by:

$$D,\% = \frac{m_d}{m_i} \times 100 \tag{7}$$

Finally, the swelling index (SI) was calculated as the ratio between the mass of swollen (electrolyte containing) polymer, m_{sw}, and the actual mass of the undissolved polymer component, m_p:

$$SI = \frac{m_{sw}}{m_p} \tag{8}$$

2.3.4. RESISTANCE MEASUREMENT

Two different methods were used to measure the resistance of the samples. The first method was developed for the electrode layer stack in blunt impact test. The second method was developed to measure the internal resistance (R_I) of the coin cell before and after impact (without copper indenter).

In the first method, a two-point setup was employed to measure the resistivity across 2 mm at the center of the electrode layer (Le, et al., 2015, a). The resistance measurement was conducted for each layer of the electrode stack under different conditions: oven-dried (R_d), dried and compressed before impact (R_c), soaked in EMC before impact (R_s), and wet condition after impact (R_i). The average values were calculated and reported.

The purpose of the second method was to investigate the effect of impact loading on the electrodes within the cell case. It was expected that, upon impact, the contact among components of the electrode would remain intact in reference cell and be damaged in CDI-modified or TSB-based cell, leading to a difference in internal resistance. That is, an impacted modified cell may exhibit a higher R_I value. Note that, if internal shorting occurs, a direct conductive path would be formed between anode and cathode, rendering it impossible to measure the internal resistance of the cell. Therefore, for the R_I measurement, the impact setup was similar to the one in Section 2.2.3, except no indenter was used. We employed the Verband der Automobilindustrie (VDA) technique,

established by the German Association of Automotive Industry (Schweiger, et al., 2010). The same battery analyzer as in Section 2.2.1 was used. Because the purpose of the VDA measurement was to investigate the condition of the cell close to internal shorting, only discharge resistance was relevant. Due to the limitation on the battery size and the analyzer, the maximum current value of 5 mA was used for the constant current discharge pulse for 1 second. The measurement was taken for each cell type at different stages: cycled-charged, preheated, and impacted(Le, et al., To be published, d).

ACKNOWLEDGEMENT

This research is supported by the Advanced Research Projects Agency – Energy (ARPA-E) under Grant No. DE-AR0000396, for which we are grateful to Dr. Ping Liu, Dr. John Lemmon, Dr. GrigoriiSoloveichik, Dr. Chris Atkinson, and Dr. Dawson Cagle. Special thanks are also due to Dr. Jiang Fan and Dr. Dengguo Wu for the help with lithium-ion battery design and processing.

Chapters 2, in part, is reproduced from Journal of Applied Physics 118, 2015. Le, Anh; Wang, Meng; Shi, Yang; Noelle, Daniel; Qiao, Yu; Lu, Weiyi. "Effects of additional multiwall carbon nanotubes on impact behaviors of LiNi0. 5Mn0. 3Co0. 2O2 battery electrodes." AIP Publishing LLC, 2015; with the permission of AIP Publishing. The dissertation author was the primary investigator and author of this paper.

Chapters 2, in part, is reproduced from Journal of Physics D: Applied Physics 48, 2015. Le, Anh V.; Wang, Meng; Shi, Yang; Noelle, Daniel; Qiao, Yu. "Heat generation of mechanically abused lithium-ion batteries modified by carbon black micro-particulates." © IOP Publishing. Reproduced with permission. All rights reserved. The dissertation author was the primary investigator and author of this paper.

Chapter 2, in part, is reproduced from the under-review manuscripts: (1) Le, Anh V.; Wang, Meng; Shi, Yang; Noelle, Daniel J.; Yoon, Hyojung; Meng, Ying S.; Wu, Dengguo; Fan, Jiang; Qiao, Yu. "Heat Generation of Mechanically Abused Lithium-Ion Battery Cell Based on Thermally Sensitive Cathode Binder;" (2) Le, Anh V.; Wang, Meng; Noelle, Daniel J.; Shi, Yang; Yoon, Hyojung; Zhang, Minghao; Meng, Ying S.; Qiao, Yu.

“Effects of Macromolecular Configuration of Thermally Sensitive Binder in Lithium Ion Battery.” The dissertation author was the primary author of these manuscripts.

CHAPTER 3–ELECTRODES BASED ON CRACKING/DEBONDING INITIATORS

3.1. MATERIALS SELECTION AND TREATMENT

Two classes of matrix material, carbon and silica, were selected as the candidates asCracking/Debonding Initiator (CDI), as listed in Table 1.1. Their particle shapes, sizes, and surface area and surface properties are available in broad ranges and can be tailored according to necessity.

Surface treatment techniques have been well developed to adjust the degree of hydrophobicity or hydrophilicity. For instance, TNM-b silica particles were available from JLK Industries with a relatively mild degree of hydrophobicity. To render it more hydrophobic, surface grafting treatment was performed with silyl material, following the procedure described by Kim et al. (2011). With a high number density of hydroxyl sites, the surface of the material is polar and thus, hydrophilic. Silyl groups react with the hydroxyl sites, forming relatively strong bonds (Park, 2010; Kim, et al., 2011). After the treatment, non-polar silyl groups dominate the surface properties, making the material hydrophobic. The materials could be heated in furnace at 600 ^{o}C to remove nonpolar surface groups. After the treatment, the CDI material was dried in a vacuum oven at 80 ^{o}C for 12 hours, and mixed into the electrode slurry, following the procedure described in Section 2.1.1.

3.2. SILICA-BASED CRACKING/DEBONDING INITIATORS

Blunt impact test on electrode stacks was performed for down selection of CDI candidates. The Aerogel-based electrode showed excessive swelling leading to immediate

debonding upon adding electrolyte, therefore was deemed non-compatible with the battery environment.Per the electrode impact testing results, the other silica-based CDI materials were ineffective for cracking/debonding initiation. After impact, no prominent cracking/debonding pattern was detected on both reference and CDI-modified anode films. For instance, Figure 3.1b, adapted from (Le, et al., 2015, a), shows the microscopic images of anode film stacks. No cracks could be detected on the reference sample (0 wt.% CDI) and the 3 wt.% TNM-b modified sample. It could be attributed to the limited surface area of silica particles, as will be discussed in Section 3.3 below.

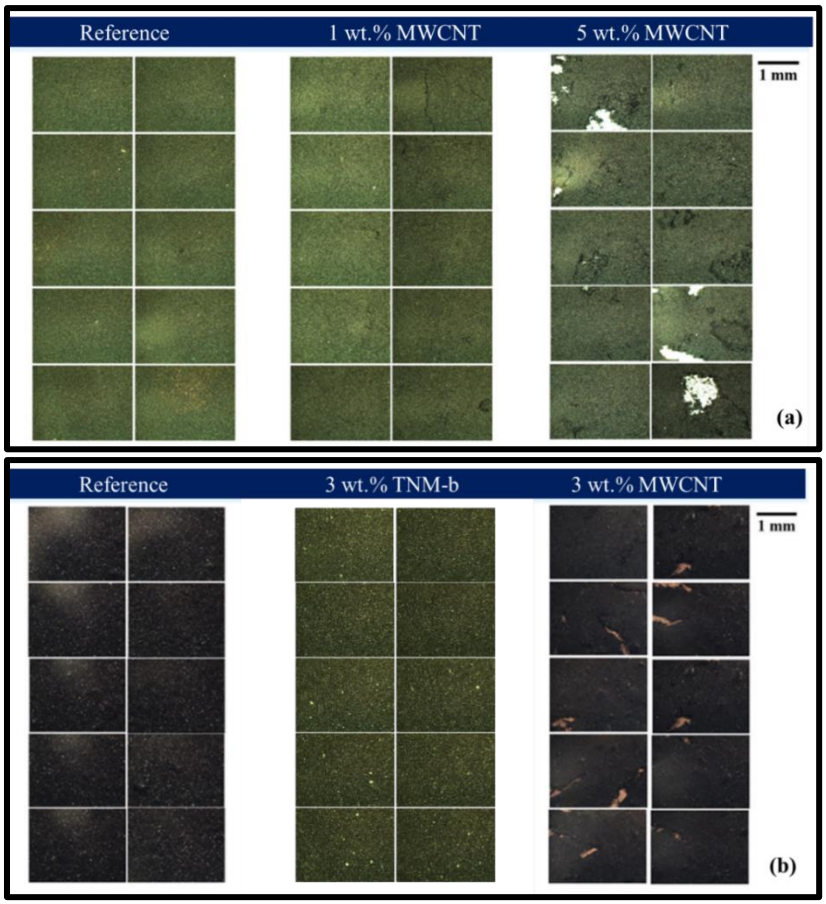

Figure 3.1. Optical microscopy of electrode film stacks after drop tower tests: (a) Cathode samples with 0 wt. %, 1 wt. %, and 5 wt. % MWCNT (left to right);(b) Anode samples with 0 wt. % CDI and 3 wt. % TNM-b and 3 wt. % MWCNT.

Resistance measurement on electrode film was carried out to investigate the structural failure in the interior electrode, such as the delamination between the active material layer and the current collector. If there were a widespread cracking network within the active material layer or delamination between active material layer and current collector, the resistance should have increased. However, such increase was not observed for the TNM-b modified electrode films after impact test, as shown in Table 3.1(Le, et al., 2015, a). The measured resistance value of a single layer of electrode was reduced after being compressed during processing, then increased due to the addition of electrolyte into the system. After the blunt impact test, the resistance of a single TNM-b modified electrode layer dropped again to 6-7 Ω, about the same as that of a dried electrode film. This result agreed with the fact that no widespread damage was observed on the impacted electrode film, and was an indication that TNM-b, along with other silica-based materials tested in this study, was not suitable for the proposed CDI mechanism.

Table 3.1. Resistance of a single layer of anode film under different conditions.

Resistance of a single layer of electrode (Ω)	**Oven-dried, R_d**	**Compressed, R_c**	**Soaked in EMC, R_s**	**Impacted, R_i**
Reference	4.5-9	10-40	7-15.5	1-20
3wt.% MWCNT-modified	4-6.5	7.5-21	7-14	7-11
3 wt.% TNM-b-modified	6-7	3-5.5	7-15	6.5-7

3.3. Carbon-based Cracking/Debonding Initiators

3.3.1. Electrode Impact Test

For the carbon-based CDIs, a number of candidates exhibited the ability to trigger cracking and debonding in electrode upon impact. The following discussion will focus on multiwall carbon nanotube (MWCNT).

The resistance measurement of MWCNT-modified electrodes before and after impact test indicated that damage occurred within the active material layer, as the average resistance of electrode film increased from 4-6.5 Ω to 7-11 Ω (Table 3.1). However, it was brought to our attention that the measurements were inconsistent. First, the reference electrode showed even a larger increase in resistance after impact test, even though no damage could be detected under microscope (Figure 3.1). Second, the resistance of electrode film increased after compression, even though the electrical contact among electrode components should be have been improved. Lastly, data scatter seemed to be quite large. For the afore-mentioned issues, these resistance measurements were deemed invalid. This could be due to various reasons, such as the roughness of electrode surface or and the exposure of electrolyte to air.

From the recorded deceleration profile of the drop weight, the stress history applied on the electrode stack in impact test was calculated. Figure 3.2 shows a representative deceleration curve, with three distinct regions being identified. The region of interest is the contact period, from which the stress history was computed as:

$$\sigma = \frac{F}{A} = \frac{ma}{A}, \qquad (3.1)$$

in which a is the recorded acceleration at a given time; m is the mass of the drop weight, i.e. 0.405 kg and 7.7 kg for cathode and anode, respectively; and A is the contact area of the sample, i.e. 1 cm^2.

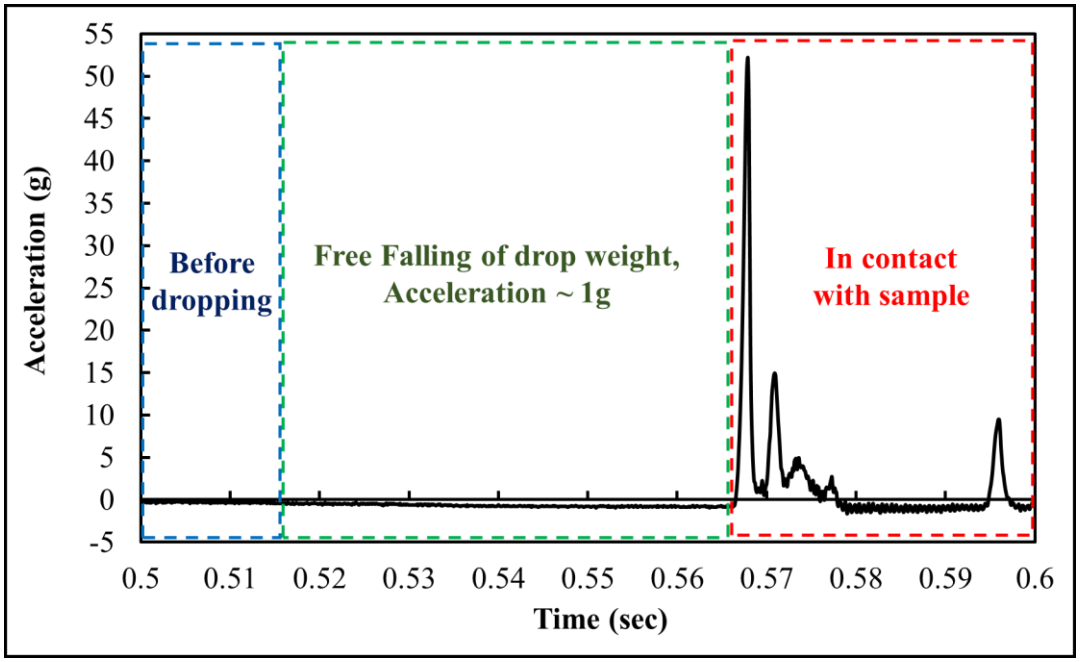

Figure 3.2. Typical acceleration history of drop weight in impact test on electrode stack.

From Figure 3.3(Le, et al., 2015, a), the stress rising rate of reference samples, i.e., the slopes of sections "AB" and "CD" in Figures 3.3a and 3.3b, respectively, were much higher than those of MWCNT-modified electrodes. Since 1 wt. % of MWCNTs was below the critical value, the stack had similar dynamic response as the reference material. The Young's modulus (E) can be expressed as

$$E = \frac{\Delta\sigma}{\Delta x / \mathrm{d}_0}, \tag{3.2}$$

in which σ is the stress applied on the specimen, x is the displacement, and d_0 is the original thickness of electrode stack. The displacement is calculated as

$$x = \int_{t_1}^{t_2} v dt = \int_{t_1}^{t_2} (v_0 + at) dt = x_0 + v_0 t + \frac{at^2}{2}, \tag{3.3}$$

where v is the velocity of the drop weight at a given time. This equation considered the motion of the drop weight from the time it came into contact with the specimen, t_1, so the initial displacement, x_0, is set to zero, and the initial velocity, v_0, is given by the equation

$$v_0 = \sqrt{2gh}, \tag{3.4}$$

in which g is the gravitational acceleration, 9.8 m/s^2, and h is the drop height, i.e. 80 mm and 12 mm for cathode and anode, respectively.

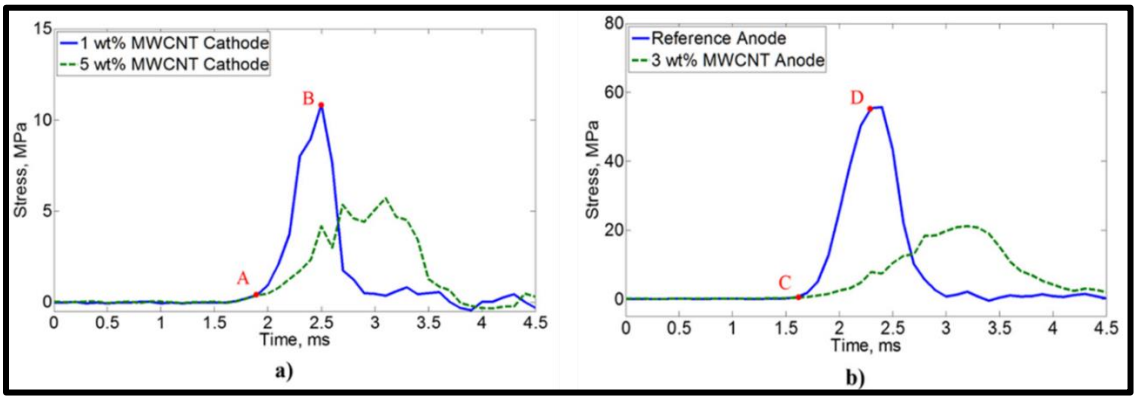

Figure 3.3. Stress history of electrode film stacks: (a) cathode and (b) anode.

Using the above equations, the Young's modulus of reference anode film was calculated to be 507 MPa, much stiffer than 53.6 MPa of the reference cathode. This was one of the reasons for the different drop weights and drop heights employed in the test. In general, the CNT-reinforced composites show increased strength and stiffness, thanks to the optimum content and the surface condition of the CNT additive (Thostenson, et al., 2001). However, in our case, when used as received and at relatively high material loading, the MWCNT additive effectively reduced overall strength and stiffness (Figure 3.3). This was mainly because widespread cracks after impact were desired. The cracking/debonding effect could be attributed to random orientation of the MWCNT. The stiffness of MWCNT along the axial direction is high while is low along transverse directions. In addition, MWCNT were not straight; thus, the effective stiffness of tended to be even lower.

Table 3.2 (Le, et al., 2015, a) shows the energy dissipated by the reference or modified sample in each test was calculated as:

$$U = \int \sigma A dx \qquad (3.5)$$

Table 3.2. Kinetic energy of drop weight and energy associated with electrode samples.

Sample	**Kinetic Energy of Drop Weight**	**Elastic Energy stored in Reference Sample**	**Plastic Energy dissipated in MWCNT-modified Samples**
	J	**J**	**J**
Cathode stack	0.32	0.40	0.32
Anode stack	0.90	0.90	0.82

For the case of either cathode or anode, the calculated values were close to the drop weight's input kinetic energy. For a reference specimen, the stress increased linearly until reaching the peak stress, indicating that the impact energy was temporarily stored in the sample as elastic energy. In this case, the sample experienced no permanent damages. For a modified sample, a sharp turning point could be observed in the stress profile of either cathode or anode, indicating that the modified specimens underwent plastic deformation (Figure 3.3). About 90% of the kinetic energy was dissipated by modified electrode film (Table 3.2). The amount of absorbed energy could be related to the content of MWCNT. The effective surface energy, E_S, between MWCNT and active material matrix was related to the elastic energy release rate, G_C, a material constant, and the density of cracks:

$$E_S = 2G_C A_C, \qquad (3.6)$$

where $2A_C$ is the total new surface area associated with the cracks. The fracture strength of the electrode samples was influenced by the content of MWCNT additive. For reference samples, these values should be higher than the applied stresses (11 MPa for cathode reference and 60 MPa for anode reference), since the reference samples remained in theirrespective elastic ranges. For the modified samples, the fracture strength was defined as the stress at the first sharp transition point of the stress profile. The values were 4.2 MPa and 7.8 MPa for MWCNT-modified cathode and anode film stacks, respectively (Figure 3.3a and 3.3b). When the stress applied by the drop weight was lower than the fracture strength of the sample, the stress intensity at any local stress concentration site on the sample was lower than the fracture toughness of the matrix. Once the stress level exceeded

the safety threshold, the elastic energy stored in stiffer MWCNT was released, which broke their bonds with the matrix. Consequently, a large number of cracks were introduced into the electrodes and might shut down the electrochemical reactions.

Many CDI candidates worked for both cathode and anode, even though the optimum concentrations were different. Figure 3.1a shows that few cracks were generated in a 1 wt.% MWCNT modified cathode. Prominent cracks were observed only when 5 wt.% MWCNT was added to the cathode film. For anode, 3 wt.% load of MWCNT appeared to be sufficient for widespread cracking/debonding. Some other promising candidates were CGR (Le, et al., 2015, b)and KBG(Wang, et al., 2016).

However, we discovered that the effectiveness of MWCNT depended heavily on the dispersion of MWCNTs in the electrode matrix. In a liquid solution, such as cathode or anode slurry, MWCNT tends to aggregated and entangled clusters. To break off the clusters and to promote uniform dispersion of MWCNT in the slurry is challenging (Hilding, et al., 2003). Mechanical stirring was not efficient to achieve uniform dispersion of MWCNT in the slurry system. As shown in Figure 3.4, an electrode film processed with mechanically stirring at 1000 rpm still showed prominent clusters across the surface, resulting in major cracks after the drop tower test. Electrode film processed with sonication appeared to have much smoother surface, indicating a better dispersion of MWCNT; yet, only a few visible cracks on few layers of the electrode stack could be detected.

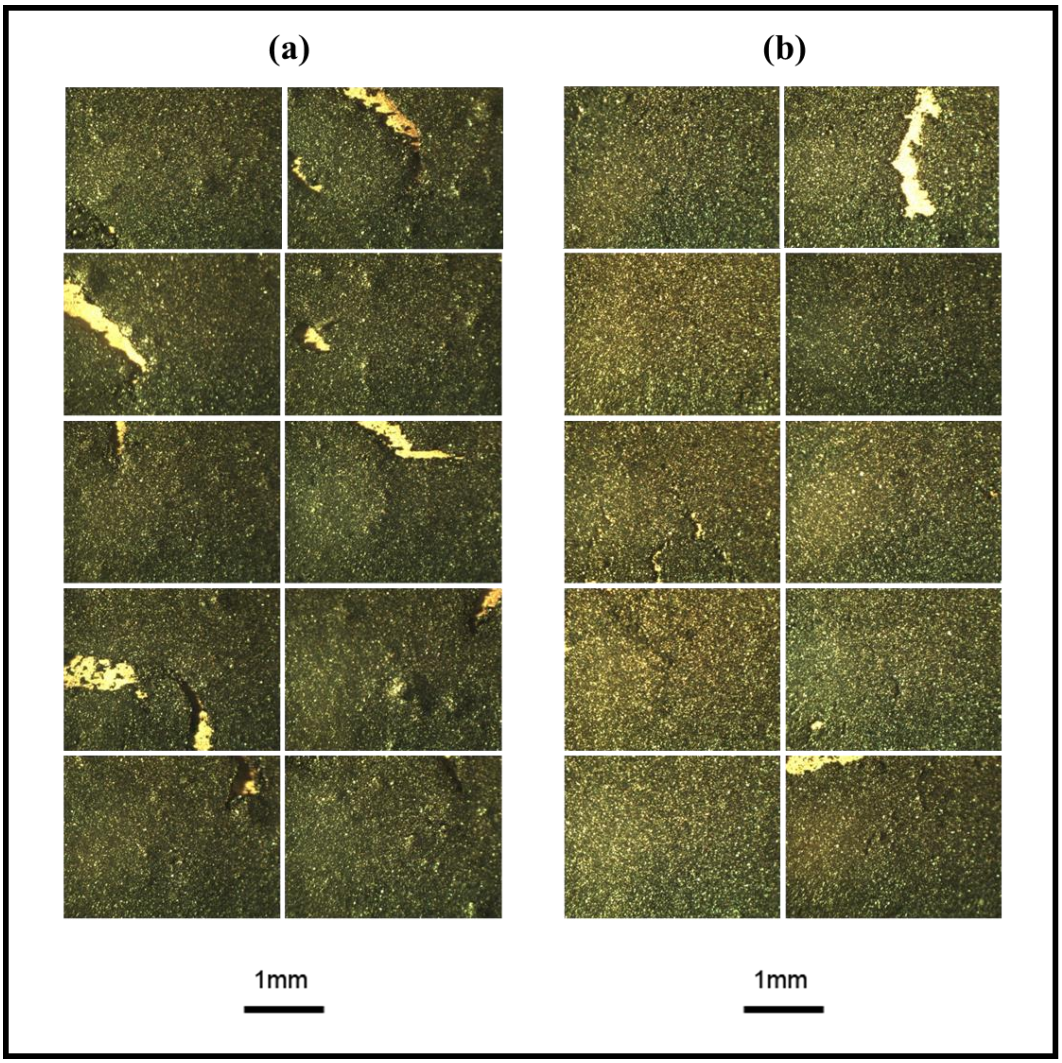

Figure 3.4. Optical microscopy of anode film stacks after drop tower tests:(a) with 3 wt.% MWCNT, processed through mechanical stirring at 1000 rpm; (b) with 3 wt.% MWCNT, processed through sonication.

3.3.2. Limitation of CDI Contents by Cycling Performance

The introduction of CDI particles into the electrode system would alter the microstructure of the active material layer. Therefore, it was critical to investigate the effects of CDI on the cycling performance of the modified battery cell. The CDI candidates

under investigation were CGR and KBG, with the added amounts ranging from 1-5 wt.% of the total mass of active material (AM), binder (B), and carbon black (CB). After appropriate treatment, the CDI material was measured to the exact amount and added into the dry AM/B/CB powder mixture, followed the normal slurry processing described in Section 2.1.1.

Cycle life measurement was conducted on cathode half-cells(Le, et al., 2015, b; Wang, et al., 2016). Compared to the AG anode in a full cell, the lithium anode in a half-cell was prone to dendrite growth and limited coulombic efficiency during cycling, as it was more thermodynamically unstable in organic solvents(Aurbach, et al., 2002). Therefore, the cycling performance measurement was conservative. Figure 3.5(Le, et al., 2015, b) shows typical cycling performance of reference cathode half-cells and CGR-modified cathode half-cells. The discharge capacity was normalized by the capacity of the second discharge cycle. With everything else being the same, addition of 1 wt% CGR did not cause any increase in degradation rate, since the chemical composition of CGR was identical to CB. The major differences between CGR and CB were the particle size, surface area and hydrophilicity. The electrode was processed with the wet slurry casting method and NMP was used as the solvent for the PVDF binder. The high surface area and hydrophilicity of the CGR additive resulted into high level of interaction between the CGR and the PVDF/CB matrix during slurry processing, hence ensuring a relatively strong van der Waals bonding between the CGR particles and the matrix during cycle life testing. However, at the same time, the uniformity of PVDF distribution around the active NMC532 particles was also affected, so the overall strength and conductivity of the

electrode were reduced. At a higher CDI loading, this effect could be detrimental to the electrochemical performance of the battery.

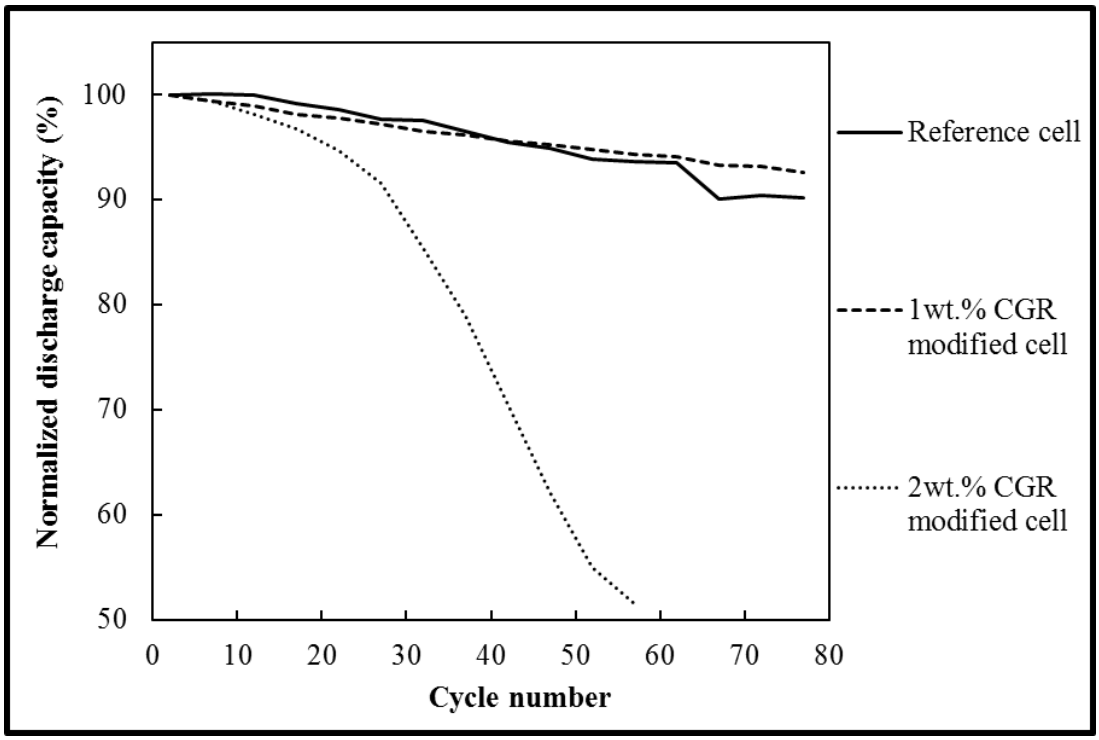

Figure 3.5. Cycling performance of reference and CGR-modified cathode half cells.

Figure 3.6 shows the typical ESEM images of GCR samples (Le, et al., 2015, b). The average size of CGR was 45-50 μm (Figure 3.6a), only slightly smaller than the electrode thickness (60-70 μm) and much larger than the particle size of the active material (10-20 μm). With a relatively high volume fraction, CGR might have blocked volumetric changes of the NMC532 active material(Zheng, et al., 2012), causing defects to be nucleated. In addition, the large particle size of the highly conductive CGR or KBG particles might have created an electrical conductivity gradient in the surrounding region, which disturbed the electron and ion flows during lithiation and de-lithiation processes

(Frackowiak & Beguin, 2001). As a result, distribution of charges became non-uniform, forming stress concentration sites even during normal operation of the battery.

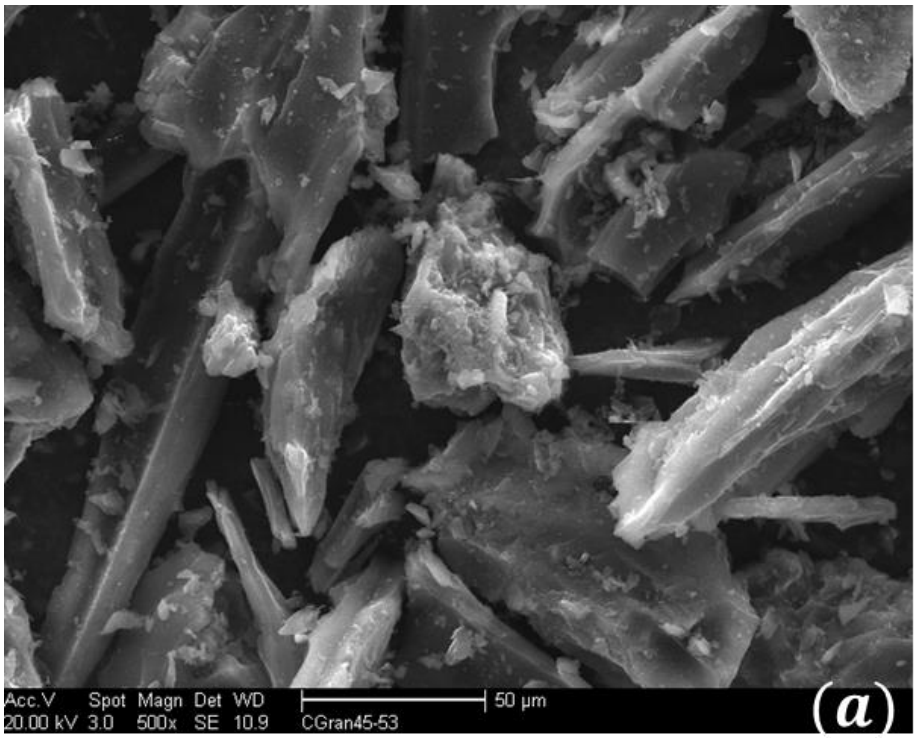

Figure 3.6. Typical SEM images of CGR samples: (a) CGR grains, (b) CGR-modified cathode, and (c) CGR-modified anode. The CGR content was 1 wt%.

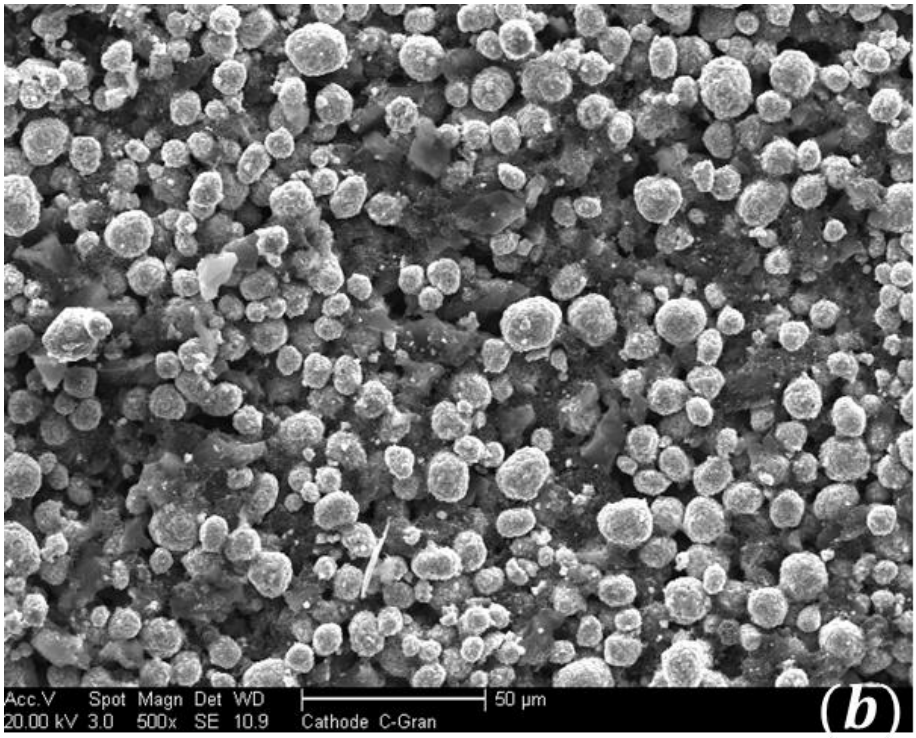

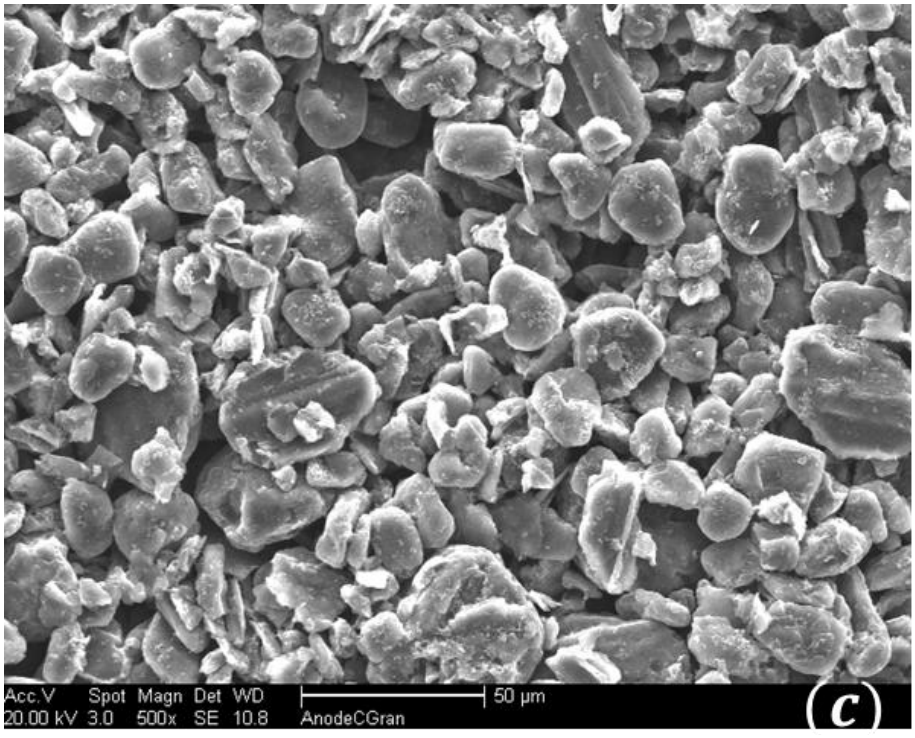

Figure 3.6. Typical SEM images of CGR samples, *continued*.

Another aspect to consider is the high degree of hydrophilicity of CGR, which tends to promote the heterogeneous dispersion of PVDF. Figure 3.6a shows the raw CGR material, and Figures 3.6b and 3.6c show the CGR-modified cathode and anode electrodes, respectively. All images are of the same scale, with the CGR content of 1 wt%. Even though the raw CGR particles appear large in Fig. 3.6a, they are not immediately detectable on the surfaces of the CGR modified cathode and anode, suggesting that the large CGR particles have been well embedded within the electrode matrix. During the wet stage of slurry processing, the highly porous and hydrophilic CGR particles attracted the NMP-PVDF solution, disrupting the otherwise uniform arrangement of PVDF-CB around the active materials, leading to a segregation of the PVDF-CB conductive matrix in the vicinity of CGR. Consequently, the strength of the CGR modified electrodes was weaker, and the conductive matrix in the CGR modified electrodes was relatively non-uniform. The optimum CGR content should be determined by the balance between the weakening effect of electrode and the increase in internal impedance. Based on our testing result, this optimum content was around 1 wt% for both CGR (Le, et al., 2015, b)and KBG additives (Wang, et al., 2016).

3.3.3. Heat Generation in Nail Penetration Test

Figure 3.7(Le, et al., 2015, b)shows typical temperature profiles in nail penetration tests. The temperature was measured 2.5mm away from the center of the cell, where the nail was driven through (Section 2.2.2). Nail test reflects a simplified condition of internal short circuit formation. When a conductive nail penetrates through a LIB cell, a direct internal flow of electrons from anode to cathode is established. The battery cell is heated

up due to the large internal current. This phenomenon is referred to as Joule heating (Santhanagopalan, et al., 2009). In a large pouch cell, the temperature increase (ΔT) often rapidly reaches more than 100 ^{o}C, which triggers thermal runaway (Yoshio, et al., 2009). For the coin cells in the current study, due to the large specific surface area, heat transfer would much reduce the temperature rise, and the peak temperature increase (ΔT_{max}) was only a few ^{o}C. To best simulate the thermal effects of a large ΔT, some cells were preheated (Section 2.1.3). Even though the CDI is a mechanically triggered safety mechanism, the pre-heating helps conditioned the cell to better resemble the behavior of a high-capacity pouch cell.

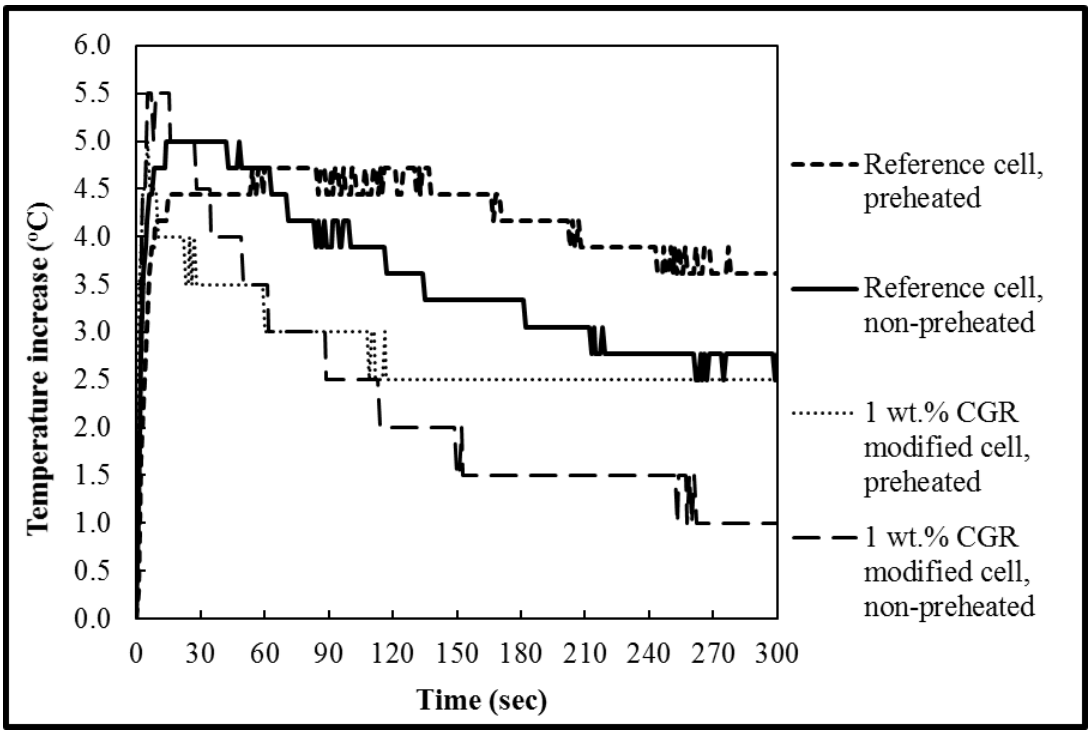

Figure 3.7. Typical temperature profiles in nail penetration tests.

Upon the nail penetration, in a non-preheated reference cell, the temperature increased by ~5 ^{o}C in 10-15 sec. The rapid heat generation was a result of short circuit,

where a sequence of rapid chemical reactions took place as the electrons quickly traveled across anode tothe aluminum charge collectorsthrough the conductive nail (Terada, et al., 2001; Pistoia, 2014). As heat generation continued, it competed with heat transfer (Terada, et al., 2001; Sun, et al., 2009; Pistoia, 2014). Eventually, ΔT entered a plateau region for ~30 sec, followed by a gradual temperature decrease. The temperature decrease rate was around 0.2 ^{o}C/min, until the cell was near its fully-discharged state, i.e. almost all electrical energy initially stored in the battery was dissipated.

For the reference cell, the temperature profile of a preheated cell was quite similar with that of non-preheated cell. However, after reaching the peak temperature increase (ΔT_{max}), the temperature dropped at the rate of 0.1 ^{o}C/min, approximately 50% slower than previously observed for the non-preheated cell. The slower temperature decrease suggested a more aggressive heat generation, possibly because the electrode structure was altered and the internal impedance was lowered. That is, the components of the electrodes re-arranged to a more confined configuration, establishing better contact between active materials and either or both of the conductive carbon black and CGR, which facilitated a lasting reaction. Preheating better fitted with the situation of a large pouch battery cell being internally shorted, where local temperature rosewell over 110^{o}Cdue to Joule heating. The lower ΔT_{max} of preheated cells was associated with stress-induced damage on the electrical contact among the cell components due to the combination of high temperature and voltage. The damage was signaled by a slight voltage drop after preheating, around 60-80 mV for both reference and modified cells.

As the electrode was modified by CGR, the temperature profile changed substantially. The slightly higher peak temperature could be attributed to the fact that the CDI additive was electronically conductive, thus facilitated the charge transfer from anode to cathode and generated more heat during the first few second of short discharge. After the peak temperature was reached, the temperature decrease rate of a non-preheated cell largely rose to about 0.4 ^{o}C/min, implying that the heat generation rate was reduced by nearly 50% compared to that in a non-preheated reference cell. In a preheated cell, the average temperature decrease rate was around 0.2 ^{o}C/min, also reduced by nearly 50% compared to that in a preheated reference cell. The reductions in heat generation rates might have been caused by the impedance increase of the CGR modified electrodes. As the large CGR particles were added in the electrode, the internal bonding among electrode components was hampered and the charge diffusion resistance was increased. The high surface area of CGR might have been another important factor, as CGR could serve as electrolyte reservoirs.

Figure 3.8 (Le, et al., 2015, b)shows the cathode and anode after nail penetration test. For cathodes, the electrode's regions with the whitish color change were structurally altered regions, as the light was reflected from the rough electrode's surface. In both CGR-modified cathode, the structurally altered areas were larger than in reference cathode. For anode, the CGR-modified electrode showed pronounced bumps, indicating debonding of the active material from the copper current collector. The reference anode also showed large whitish region surrounding the penetrated point. However, for anode, this region was associated with the SEI.

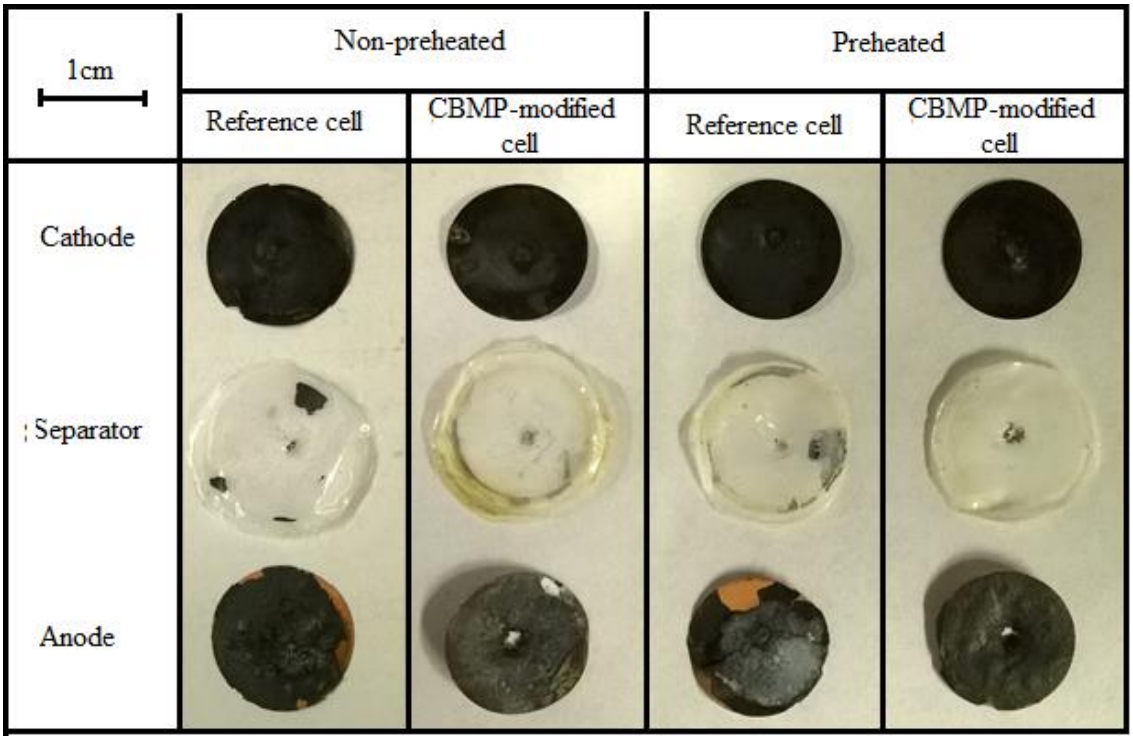

Figure 3.8. Photos of cell components after nail penetration test.

In the damaged regions, the charge transfer was blocked and thus, the return path of internal shorting was less conductive, which lowered the heat generation rate. The effects of CGR were more evident on anodes than on cathodes, probably due to larger particle size of the graphite active material. That is, the nonuniformity of the conductive binder-carbon black network caused by highly porous CGR particles might have been more severe in anode than in cathode, so the bonding among the electrode's components were weakened at a larger scale. As a result, debonding between the modified anode layer and the copper charge collector was pronounced, which also contributed to the internal impedance increase. The total generated heat, which could be assessed through the area under the temperature profile curve, was nearly the same for all the tested cells. The cell

capacity, i.e. the amount of stored electric energy, was clearly unaffected by preheating or addition of CGR.

The behavior of the 1 wt.% KBG modified cell in nail penetration test was similar to that of the 1 wt.% CGR modified cell (Wang, et al., 2016). While KBG particles were more angular, they were also carbon-based with similar surface area (Table 1.1).

3.3.4. Heat Generation in Blunt Impact Test

Blunt impact tests were performed to evaluate the cell performance upon dynamic loadings. Figure 3.9 (Le, et al., 2015, b)shows representative temperature profiles of reference and CGR-modified battery cells. As described in Section 2.2.3, the temperature measurement was taken 5.0 mm away from the center of the cell, where the spherical copper indenter was placed, and was also the center of impact. Under impact loading, even a battery cell at 0% SOC would exhibit a certain temperature increase around 1-2 ^{o}C, due to the rupture and friction of cell components as well as the sudden movement of thermocouple. This base temperature increase had been subtracted from the raw temperature data, giving the corrected curves (Figure 3.9). As the indenter compressed the cathode, the membrane separator, and the anode, the membrane separator failed, so that the positive and negative electrodes directly contacted each other, leading to rapid exothermic short circuit reactions. Similar with the nail penetration test, a significant temperature increase, ΔT, was detected. The temperature rose to the peak value in about half a minute. The peak temperature change, ΔT_{max}, was nearly 3.5 ^{o}C. Both the peak temperature and the temperature increase rate were lower than that of nail experiments. On the other hand, the

post-peak temperature decrease rate of the reference cell was nearly 0.2 ^{o}C/min, twice as much as that of nail test. The lower peak temperature increase and higher temperature decrease rate could be attributed the fact that the anode was not in direct contact with the cathode's aluminum current collector, which was identified as the most aggressive internal shorting mode (Santhanagopalan, et al., 2009).At the same time, therate at which the heat was dissipated into the surrounding environment could also be higher in blunt impact test, as it imposed more damage on the insulation system.

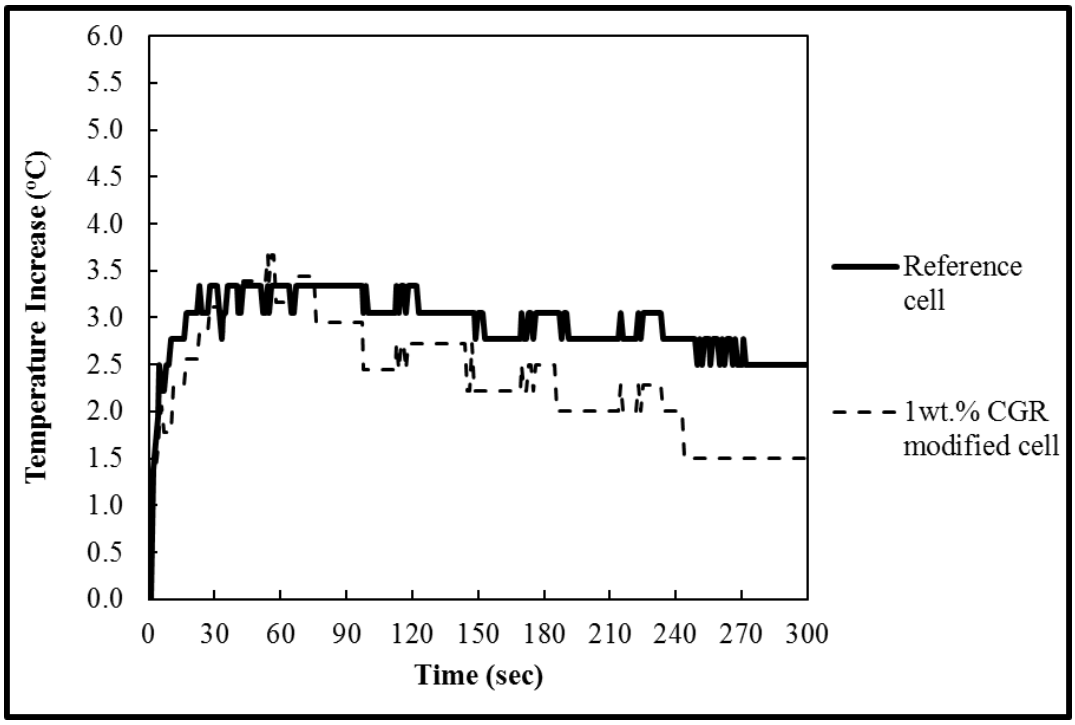

Figure 3.9. Typical temperature profiles in blunt impact tests.

With the addition of 1 wt% CGR, the temperature decrease rate increased to about 0.4 ^{o}C/min, around 2 times higher than that of the reference cell, compatible with the results of the nail penetration experiments. Clearly, the CGR particles weakened the electrode. As the impact happens, widespread damaging took place, as shown in Figure 3.10 (Le, et al.,

2015, b), and therefore, the internal impedance increased. Compared with the reference cell, the CGR-modified cathode did not exhibit much difference, while the CGR-modified anode was significantly weakened. In fact, cathode is usually the "bottleneck" of the LIB's performance, (Choi, et al., 2012). To avoid unfavorable side effect on the electrochemical performance of the battery, the weakening effect was more desirable in anode than in cathode.

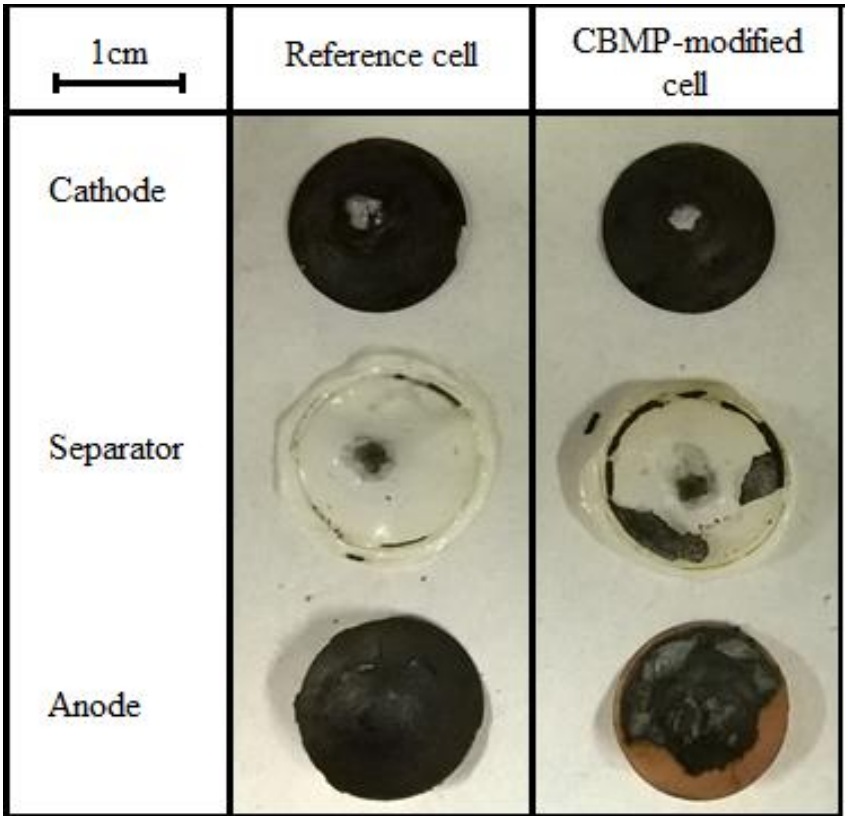

Figure 3.10. Photos of cell components after blunt impact test.

Again, the behavior of the 1 wt.% KBG modified cell in blunt impact test was similar to that of the 1 wt.% CGR modified cell described above (Wang, et al., 2016).

ACKNOWLEDGEMENT

This research is supported by the Advanced Research Projects Agency – Energy (ARPA-E) under Grant No. DE-AR0000396, for which we are grateful to Dr. Ping Liu, Dr. John Lemmon, Dr. GrigoriiSoloveichik, Dr. Chris Atkinson, and Dr. Dawson Cagle. Special thanks are also due to Dr. Jiang Fan and Dr. Dengguo Wu for the help with lithium-ion battery design and processing.

Chapters 3, in part, is reproduced from Journal of Applied Physics 118, 2015. Le, Anh; Wang, Meng; Shi, Yang; Noelle, Daniel; Qiao, Yu; Lu, Weiyi. “Effects of additional multiwall carbon nanotubes on impact behaviors of LiNi0. 5Mn0. 3Co0. 2O2 battery electrodes.” AIP Publishing LLC, 2015; with the permission of AIP Publishing. The dissertation author was the primary investigator and author of this paper.

Chapters 3, in part, is reproduced from Journal of Physics D: Applied Physics 48, 2015. Le, Anh V.; Wang, Meng; Shi, Yang; Noelle, Daniel; Qiao, Yu. “Heat generation of mechanically abused lithium-ion batteries modified by carbon black micro-particulates.” © IOP Publishing. Reproduced with permission. All rights reserved. The dissertation author was the primary investigator and author of this paper.

CHAPTER 4–ELECTRODES BASED ON THERMALLY SENSITIVE BINDERS

4.1. THERMALLY SENSITIVE BINDER

4.1.1. MATERIALS SELECTION

To select thermally sensitive binder (TSB), PVDF-HFP with different HFP contents (Table 1.2) were tested. We tested cathode half cells with different TSB candidates. The processes for sample fabrication and testing has been described in Chapter 2.

Figure 4.1shows typical temperature increase profiles of coin cells in nail penetration tests. The temperature was measured 3 mm away from the center of the cell, simultaneously as the nail was driven through. Nail test reflected a simplified, intense condition of internal short circuit formation. In a large pouch cell, the local temperature increase (ΔT) near the nail penetration site often rapidly reaches 100-200 ^{o}C, which triggers thermal runaway (Yoshio, et al., 2009). For the coin cells in the current study, due to the limited cell capacity and the large specific surface area, heat transfer much reduced the peak temperature increase (ΔT_{max}) to only few ^{o}C. To best simulate the thermal effects of a large ΔT, the cells were preheated at 110 ^{o}C, so as to trigger the softening and swelling of TSB (Section 2.1.3).

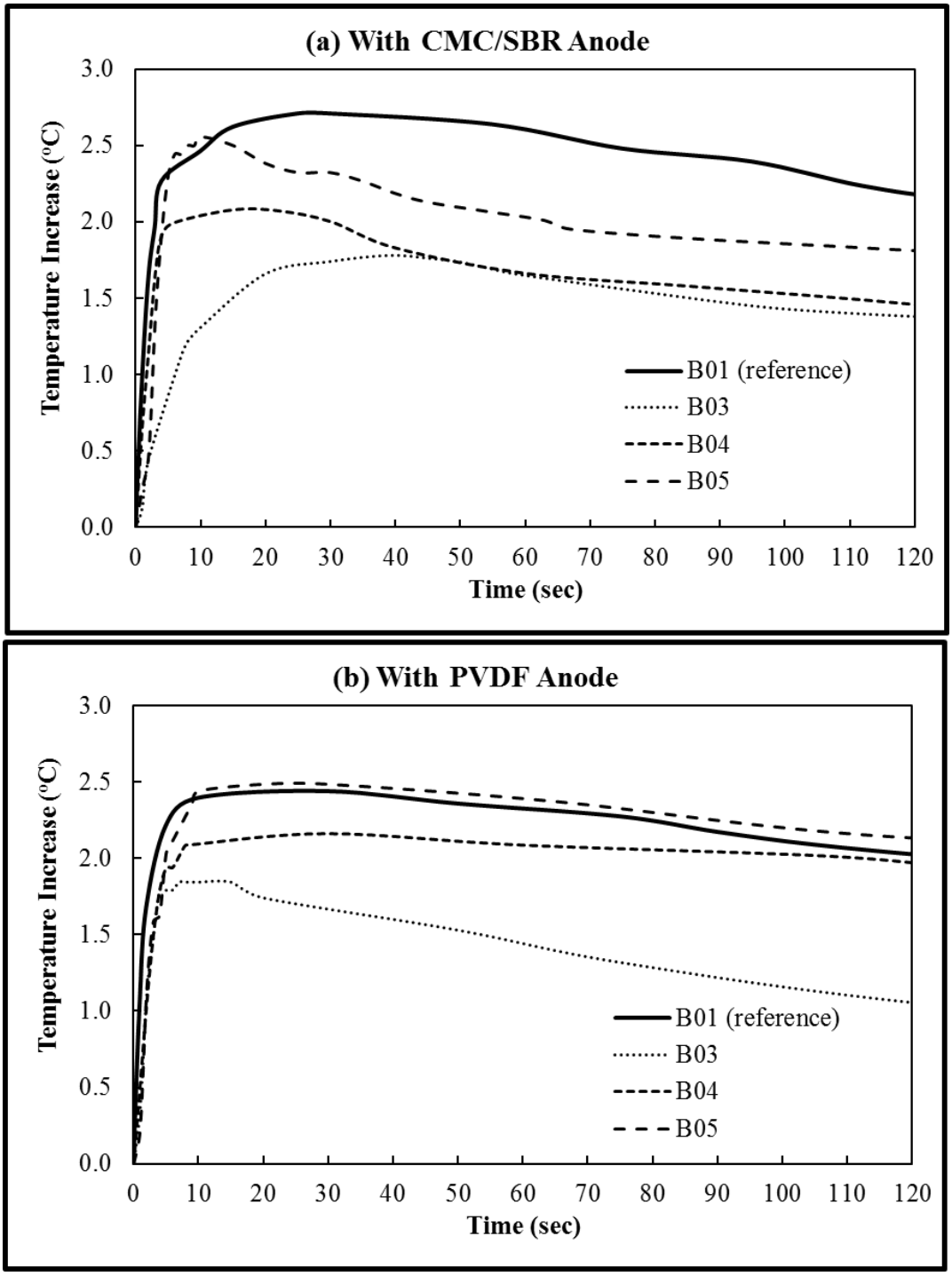

Figure 4.1. Typical temperature profiles in nail penetration tests of full cells. The cathode contained 4 wt.% pristine PVDF or HVDF-HFP binder; the anode contained (a) 4wt% CMC/SBR (2:2) or (b) 6wt% PVDF. The cathode binder type is indicated by the legend.

Upon nail penetration, in a reference cell, the temperature increased by ~2.75 ^{o}C and ~2.45^{o}C, for anodes based on CMC/SBR and PVDF, respectively. The rapid heat generation, reflected by the steep initial slope, was a result of high rate discharge. As the heat generation continued, it competed with the heat dissipation, and eventually ΔT entered a plateau, followed by a gradual temperature decrease until the cell was fully discharged and the stored electrical energy was dissipated. The temperature decrease section might be of interest for the investigation on the overall cell capacity and the discharge rate effects, yet the major goal of the TSB development was to slow down the heat generation rate in the initial stage and to reduce the peak temperature.

In a TSB-based cell, the temperature increased by ~1.75 ^{o}C and ~1.85^{o}C within 30 seconds, for anode binders of CMC/SBR and PVDF, respectively. The reduction in heat generation rate should be related to the impedance increase of TSB cathodes during preheating. At 110 ^{o}C, the smallest semi-crystalline areas in TSB were softened or melted and became amorphous. In these newly formed amorphous regions, the polymer chains attracted more electrolyte from adjacent fields, causing a sudden polymer-electrolyte phase change and distorting the cathode morphology. The conductive binder/CB network became disconnected in these swollen regions. The contact between carbon black (CB) and active material (AM) was also loosened and the binding strength was much weakened. The internal impedance rose within the composite electrode layer and at the surface of current collector. As a result, the electron and ion transports were suppressed.

For a cell with CMC/SBR-based anode, the peak temperature could be reached within 30 seconds after the nail penetrated through the cell. The initial slope of temperature

profile was the lowest if the B03 based cathode was used, suggesting that the TSB had effectively disintegrated the active components of the positive electrode. The peak temperature was reduced from 2.71 ^{o}C in reference cell to 1.74 ^{o}C in B03-based cell by ~36%. The CMC/SBR binder did not coat uniformly around the AG particles in anode, only creating bridges among these particles, which was more tolerant to electrode morphology changes.

For cells with PVDF anodes, the peak temperature was reached within 10 seconds after the nail penetrated through. The initial slopes of temperature profiles were almost the same for the reference cells and the B03 based cells. The peak temperature was reduced from 2.38 ^{o}C in a reference cell to 1.84 ^{o}C in a B03 cell by ~23%. In contrast with the CMC/SBR binder, the PVDF binder uniformly coated the AG particles in anode. Such an anode was relatively stiff and thus, the density of the compacted electrode layer was lower than that of CMC/SBR-based anode, resulting in a higher heat generation rate in the initial stage of nail penetration.

For large pouch cells, thermal runaway can happen within 1 min after internal shorting takes place (Doh, et al., 2008). In the current experiment, the peak temperature was reached within 10-30 sec. The temperature increase was relatively small, mainly due to the limited Joule heating of the small-sized coin cells (Lin, et al., 2013). Although no aggressive exothermic reactions were triggered, the testing data reflected the system behavior at the early stage of heat accumulation, critical to the materials selection and battery cell design.

Figures 4.2a and 4.2b show the cycling performance of cathode half cells with different anode binders, CMC/SBR and PVDF, respectively. In these tests, the cells were charged and discharged between 3.0-4.3 V at room temperature. The first cycle was performed at 0.1 C to condition the cell. The following cycles were performed at 1 C. The discharge capacity was normalized by the capacity of the second discharge cycle, which was ~1.2 mAh for each cell. With everything else being the same, replacement of 4 wt% reference PVDF binder by 4 wt% TSB led to a faster decay. When the PVDF was used as binder for anode, large fading of the TSB-based cell could be observed from the starting cycles. When CMC/SBR was used as the anode binder, the TSB-based cell was quite stable for the first 50 cycles, after which the decay accelerated. Note that, the thinner electrodes used for this cycle life test were still quite thicker than that of regular coin cells (Marks, et al., 2011). The thickness of dried and calendered electrode was around 20-25 μm, which should accommodate at least two layers of the 10 μm active material (AM) particles. Therefore, any binder failure would have more considerable detrimental effects on the electrochemical properties of the cells.

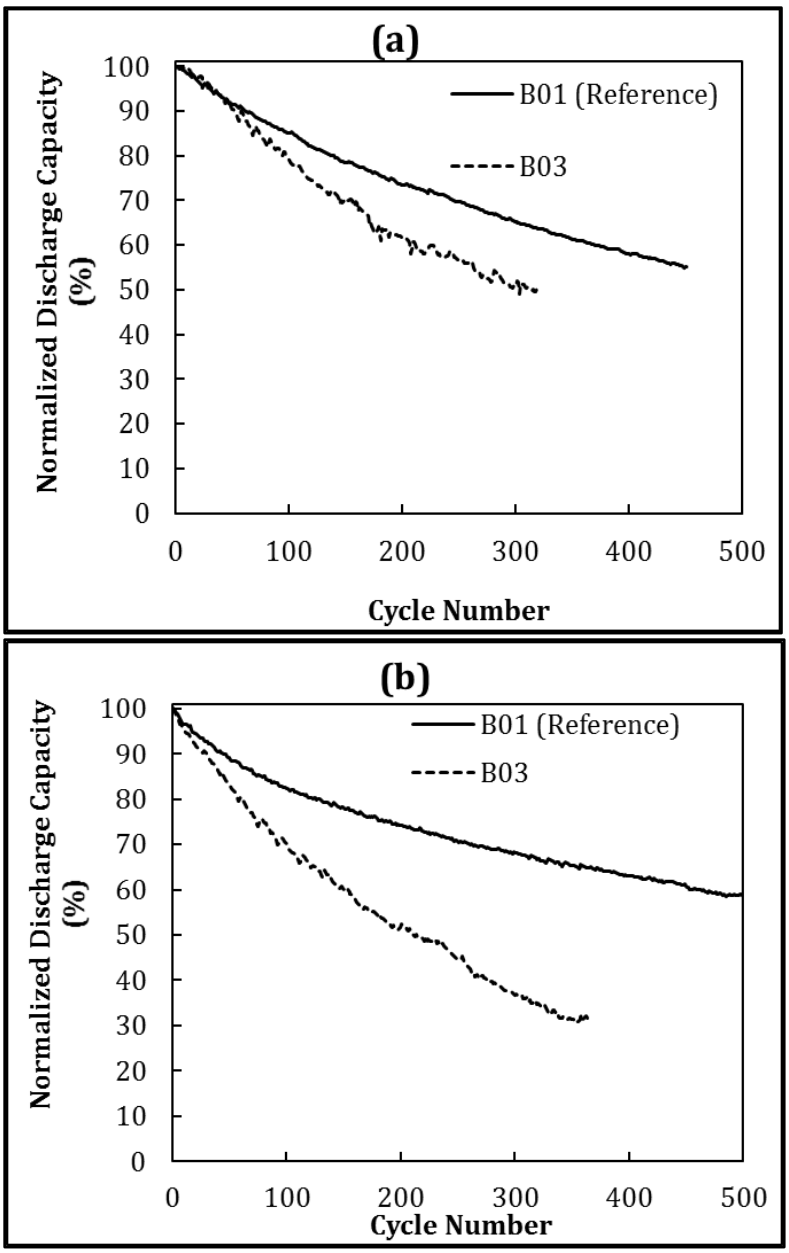

Figure 4.2. Cycling performance at 25 ^{o}C of full coin cells, with the anodes based on CMC/SBR binder or and (b) PVDF binder.

A closer analogue to commercial battery cells was produced by using the same cathode, anode, and electrolyte materials, but with a much larger cell size, for cycle life testing (Figure 4.3). Large pouch cell fabrication and testing were performed by the American Lithium Energy Corp. (ALEC, Vista, CA). The large pouch cells contained 10

layers of electrodes welded together, with the layer size of 76.2×76.2 mm. The cathode's active material (AM) was NMC532, the same material as used in electrode and coin cell testing. The AM loading was the same for the reference and TSB-based cells. The reference cathode binder was B01, and the modified cathode binder was B03. The anode binder was CMC/SBR. The large cells were charged at 0.7A to 4.2V, and discharged to 2.8V at 0.7A, which was approximately C/3. The first-cycle capacities were 2,152 mAh and 1,878 mAh for the reference and TSB-based cells, respectively. The lower gravimetric energy density of TSB-based cell was due to the higher irreversible capacity loss. Due to its highly amorphous nature, B03 might have interacted and electrolyte more aggressively, forming thicker and denser solid-electrolyte interphase (SEI) on the cathode's side and reducing its electrical conductivity. It could be seen that the cycling performance of the B03-based cell was much more stable than in a coin cell, suggesting that, even with the much-higher electrode thickness, B03 imposed less challenges as the cell size approaches the industrial level. This could be attributed to the uniform cell closing pressure and lower free volume, which might have helped keeping the TSB-based electrodes compacted against excessive swelling, as well as keeping the contact between the active electrode and the current collector. However, the decay rate of the B03-based cell had the tendency to increase after 110 cycles, probably due to the weak bonding strength between the electrode layers and the current collectors.

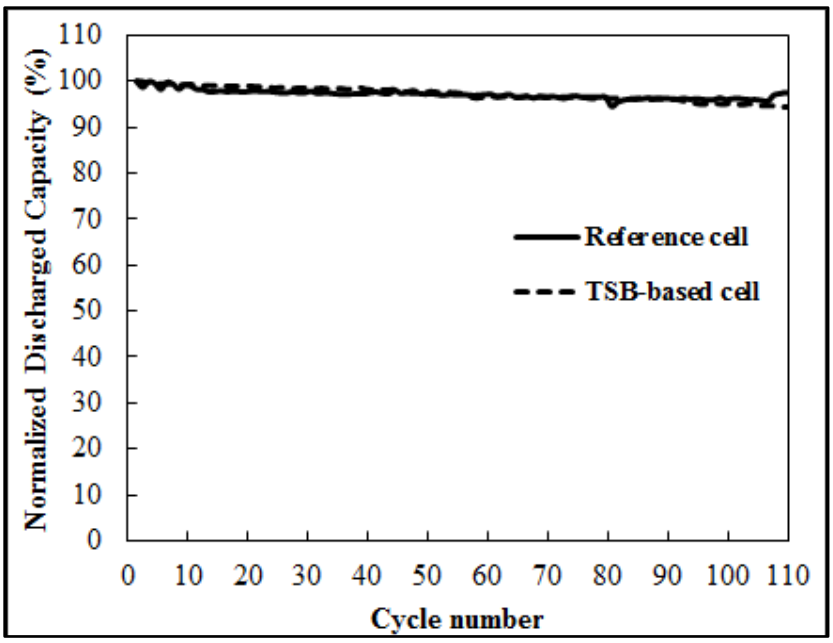

Figure 4.3. Cycling performance of large pouch cells at room temperature (25 ^{o}C).

Clearly, the above study did not facilitate a fully developed battery electrode binder. Issues related to the gradual swelling and loosening of TSB, the relatively uniform distribution of TSB around AM particles, the thickness and density of solid-electrolyte interface (SEI), the HFP content, as well as their influence on ion transport and reversibility must be further analyzed. Nevertheless, it was validated that B03 could significantly lower the heat generation rate of the battery cell. This result shed much light on developing safe and robust large-scale energy storage systems.

To conclude, heat generation of mechanically abused lithium-ion battery (LIB) coin cells based on thermally sensitive binders (TSB) had been investigated (Figure 4.1). The TSB baseline candidates was PVDF-HFP. Upon nail penetration, with a high HFP content of 32 wt%, TSB could efficiently reduce the peak temperature of preheated cell by up to 36%; if the HFP content was relatively low (~24 wt%), this beneficial effect became secondary. The reduction in heat generation rate was related to the softening of TSB that

begins at about 80 ^{o}C. The binder softening not only weakened the bonding strength among active material particles, but also led to more aggressive electrolyte absorption, both of which increased the internal impedance. This TSB baseline material, however, had a negative influence on the cycling performance of LIB cells.

4.1.2. Modification of Baseline Material

In the previous section, we demonstrated that, instead of using PTC or CDI, if the polymer binder of LIB electrode was thermally sensitive, the internal impedance of LIB cell could be largely increased upon preheating. The thermally sensitive binder (TSB) was designed to fail at elevated temperature (~110 ^{o}C) and to disintegrate the electrode components. As the return path of short-circuit was shut down, the internal shorting current was reduced and the heat generation was slowed down. Our testing results showed a 40% reduction in peak temperature increase in nail penetration test on coin cells. However, the cycle life of the TSB-modified LIB cells was unsatisfactory, attributed to the swelling of the TSB binder. The TSB under investigation was B03, a poly(vinylidenefluoride-co-hexafluoropropylene) (PVDF-HFP) with high HFP content at 32 wt.%. The HFP component rendered the binder phase thermally sensitive yet also more amorphous and more susceptive to electrolyte attack. Even though the ability to absorb electrolyte enhance the ionic conductivity, it is only favorable when used as the membrane separator and only with a low HFP content less than 24 wt% (Song, et al., 2003; Raghavan, et al., 2014). When the HFP content is above 30 wt%, PVDF-HFP absorbs much electrolyte, swells, and loosens the contact among the particles of active materials and current collector(Le, et al., To be published, a). In addition, the more access the electrolyte has to the active materials,

the more side reactions would occur, which may result in thicker solid-electrolyte-interphase (SEI) layers. Because SEI does not conduct electrons and is almost impenetrable to electrolyte, the electrode becomes less conductive both ionically and electronically.

In this section, we investigated a number of polymer treatment methods in order to enhance the cycle life of TSB-based LIB cells, as shown in Table 4.1. The investigated methods included: adjusting molecular weight (M_W), crosslinking, polymer blending, and controlled crystallinity(Le, et al., To be published, b, c). The treated TSB must remain its high processability, and must have little detrimental effects to the performance of other LIB components, i.e. active materials, carbon black (CB), and electrolyte. The treated TSB should be strong at room temperature and disintegrate the electrode at 100-130 ^{o}C(Doughty & Roth, 2012; Roth & Orendorff, 2012).

Table 4.1. Modified cathode binders under investigation

Modification Method	Sample Code	Binder Components	
		Component 1	**Component 2**
	B01	PVDF (534,000 g/mol)	
	B02	PVDF (180,000 g/mol)	
	B03	PVDF-HFP with 32 wt% HFP (~500,000 g/mol)	
Controlled Molecular Weight (M_W)	R1	Low-M_W portion harvested from B01 (6 wt% of B01)	
	R2	Low-M_W portion harvested from B02 (2 wt% of B02)	
	R3	High-M_W portion harvested from B03 (0.5 wt% of B03)	
Crosslinking	X-2	B03	BPO (2 wt% of Component 1)
	X-10		BPO (10 wt% of Component 1)
	X-20		BPO (20 wt% of Component 1)
Thermal treatment	T1-50	B01 (50 wt%)	B03 (50 wt%)
	T1-20	B01 (20 wt%)	B03 (80 wt%)
	T1-10	B01 (10 wt%)	B03 (90 wt%)
	T2-50	B02 (50 wt%)	B03 (50 wt%)
	T2-20	B02 (20 wt%)	B03 (80 wt%)
	T2-10	B02 (10 wt%)	B03 (90 wt%)

In this section (4.1.2), the cycling tests were performed at 60 ^{o}C. Figure 4.4 (Le, et al., To be published, b, c) summarizes the cycling performance of different types of cells subjected to different modification methods. The best performing modified binders were tested for heat mitigation effect in nail penetration test (Figure 4.5).

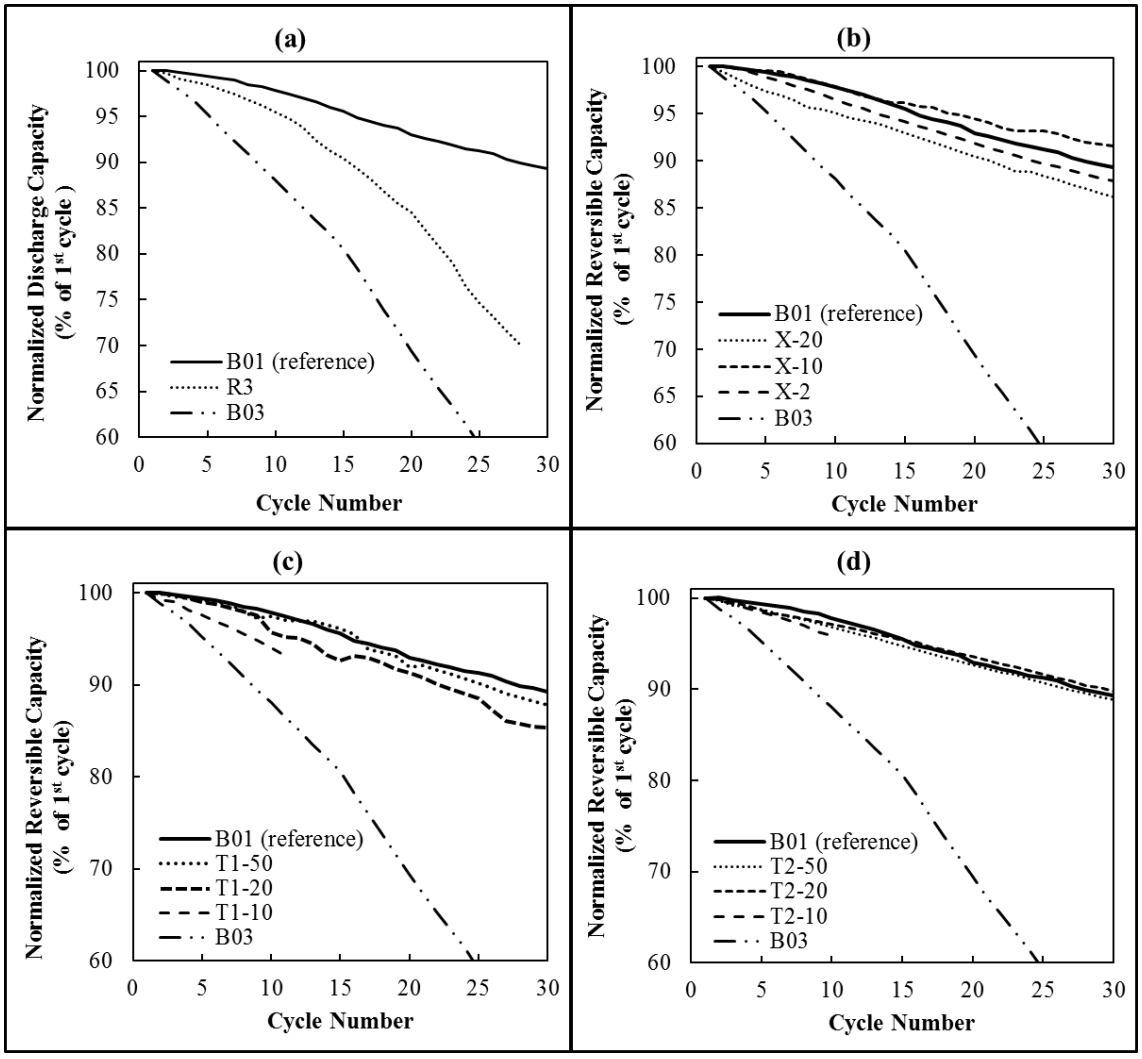

Figure 4.4. Typical cycling performance at 60 ^{o}C of cathode half-cells with modified B03: (a) refined (R3) and as-received (B03) PVDF-HFP; (b) cross-linked PVDF-HFP (B03); (c) thermally treated B01/B03 blends; (d) thermally treated B02/B03 blends.

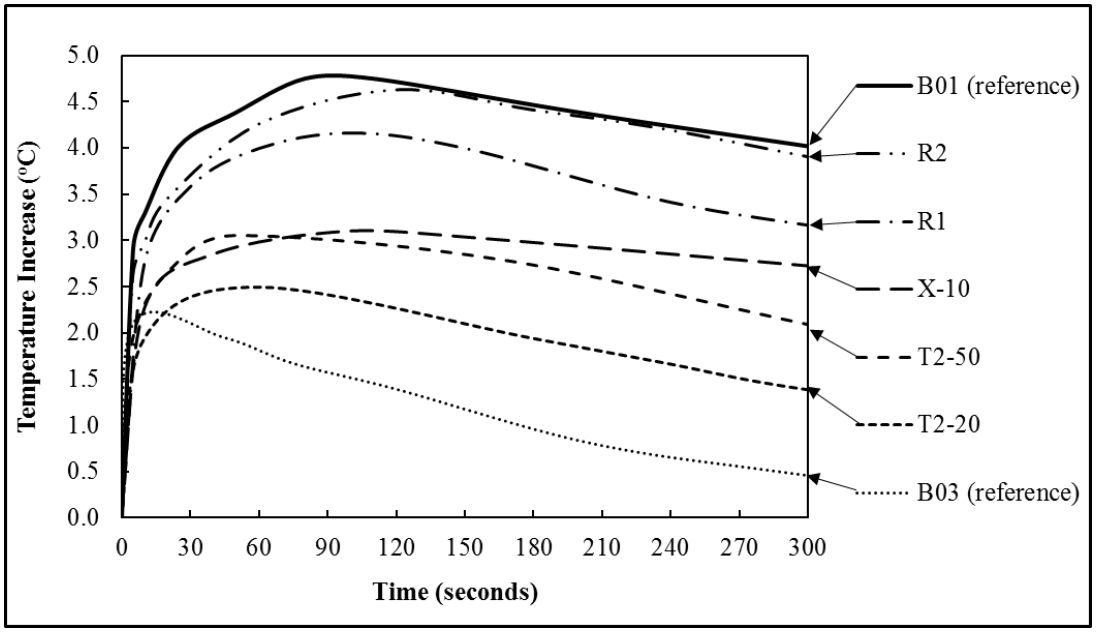

Figure 4.5. Typical temperature profiles of nail penetration tests of cathode half-cells.The arrows indicate cathode binder types.

4.1.2.1. Binder with Controlled Molecular Weight

Molecular weight, M_W, of polymer is a vital factor that dominates thermal, mechanical, and swelling properties (Nunes, et al., 1982). Previous testing data indicated that the solvent resistance of B03 was too low while the softening temperatures of B01 and B02 were too high. Therefore, if M_W of B03 could be increased or M_W of B01 or B02 can be reduced, the balance between thermal sensitivity and swelling might be enhanced.

To vary M_W of polymer binder while keep everything else similar, we harvested binder samples from the reference polymers, i.e. B01, B02, and B03, through controlled precipitation. About 10 g of B01, B02, or B03 was first dissolved in 100 ml of acetone. In a capped beaker, the solution was stirred continuously at 1000 rpm with a mechanical

stirrer (IKA EUROSTAR 20) for 1 hour; the beaker was placed on a hot plate (Corning PC 4000), with the temperature set to 100 ^{o}C. The solution was then transferred to an open container and placed back onto the heater, so that acetone evaporated. Polymer precipitate was visible after about 5 min, and was collected every 5 minutes by using a stainless-steel tweezer, until the remnant material became gel like. The harvested precipitate tended to have a higher M_W than the remnant material (Ueberreiter, 1968). As similar controlled-precipitation processes were repeated for harvested or remnant materials, the highest-M_W and the lowest-M_W portions of polymer were separated. The harvested materials were about 6 wt%, 2 wt%, or 0.5 wt% of the initial polymers, for B01, B02, and B03, respectively, as shown in Table 4.1. The slurry processing, coin cell fabrication, and cell testing followed the same procedure as described in Chapter 2.

Typical cycling performance of R3-based cathode half cells at 60 ^{o}C is shown in Figure 4.4a. It can be seen that even though the high-M_W B03 (R3) showed a significantly improved cycling performance compared to the B03-based cells, the degradation rate was still must faster than that of reference (B01-based) cells, suggesting that while the high M_W improved the strength and swelling resistance of binder, the binder phase still could not survive the harsh charge-discharge process. One of the possible reasons of the poor performance of R3 was that PVDF-HFP tends to be highly amorphous (Gozdz, et al., 1994).

As show in Figure 4.5, when the LIB cell is mechanically abused, the low-M_W PVDF binders, i.e. R1 and R2, did not efficiently trigger widespread de-functionalization of electrodes before heat generation accelerated. The reductions in peak temperature increase were only ~ 0.5-1.0 ^{o}C, roughly 10 % of the peak temperature increase of reference

B01-based cathode half-cell. Surprisingly, the refined B01 material, i.e. R1, resulted in a lower temperature increase than that of refined B02, i.e. R2. This could be attributed to the longer chain and higher degree of branching of B01, which might have limited the binder-CB network from being uniformly distributed throughout the composite electrode.

4.1.2.2. CROSSLINKED BINDER

When properly formed, crosslinks could strengthen the polymer and improve the resistance to swelling (Nielsen , 1969). PVDF-HFP can be crosslinked by bisnucleophiles, such as diamines or bisphenols, or by irradiation. Common crosslinkers include hexamethylene diamine (HMDA) and their carbamates (HMDA-C) or derivatives, benzoyl peroxide (BPO), etc(Taguet, et al., 2005). In the current study, benzoyl peroxide (BPO) was employed as the thermal initiator, following the procedure established in (CN102924732B, 2013). BPO was dissolved in NMP and mixed with other components of electrode; the amount of BPO was shown in Table 4.1. After drying, the electrode film was compressed at 5 MPa using a type-5582 Instron machine for 5 min to stabilize the microstructure, and then sandwiched between two stainless steel pistons, secured by a C-clamp, and cured in a Carbolite CFT 12 furnace at 200 ^{o}C for 2 hours. Finally, the electrode film was cut into discs, and used to assemble cathode half-cells, as discussed in Section 2.1.2.

While crosslinked PVDF-HFP has been used to produce membranes in LIB to host electrolyte (Katsurao, et al., 2002; Song, et al., 2003), crosslinking PVDF-HFP is relatively difficult under mild conditions (Taguet, et al., 2005). With the presence of lithium metal

oxides, carbon black nanoparticles, and adsorbed electrolyte, the control on surface area, swelling resistance, and SEI of electrode became challenging. In this study, we used BPO as the crosslinking agent. According to Figure 4.4b, it was clear that compared with pristine B03, crosslinked binders led to much better cycle lives of LIB cells. The crosslink density was adjusted by the amount of BPO. In binders X-2, X-10, and X-20, the BPO contents were 2 wt%, 10 wt%, and 20 wt% of B03, respectively. The cycling performance of X-2 based LIB cells were somewhat lower, but comparable with that of B01 based reference cell. When the BPO content increased to 10 wt%, X-10 based LIB cells showed even better cycle lives than reference cells. As the BPO content was further increased to 20 wt%, however, the degradation rate of X-20 based cell was increased to higher than that of X-2 based cell, but still much lower than that of cells based on pristine B03. Clearly, crosslinking helped stabilize the binder phase and reduce swelling, so that the LIB cells were much more stable than B03-based ones. However, when the BPO content was too high, the crosslinking initiator might have attacked the polymer chains and result in chain scission (Taguet, et al., 2005).

In a nail penetration test, the temperature increase, ΔT, of X-10 based cell was considerably lower than that of B01-based reference cell by ~37% (Fig. 4.5). This result indicated that X-10 was a functional binder that not long slightly enhanced the electrochemical performance of LIB cell during normal operation, but also suppressed heat generation when the cell was mechanically abused. Note that the temperature increase of X-10 based cell was higher than that of B03-based cell, since the stronger X-10 binder

rendered the electrode layer more structurally integral and the damaging was less extensive at elevated temperature.

4.1.2.3 Thermally Treated Polymer-Blend Binders

Amorphous PVDF-HFP binder was prone to aggressive swelling in electrolyte at elevated temperature (e.g. ~110 ^{o}C), which disintegrated electrode and suppressed thermal runaway. Such a polymer also swelled in electrolyte under normal working condition of LIB cell, which led to the poor cycling performance. It was, therefore, desirable that the crystallinity could be increased to enhance the binder properties. Moreover, replacing a portion of PVDF-HPF, i.e. B03, by a proven stable polymer, e.g. PVDF (B01 or B02), should help stabilize the binder phase.

We first blended B03 with either B01 or B02 in NMP, with proportions as shown in Table 4.1. The rest of the slurry processing, cell assembly, and cell testing followed the procedure as described in Chapter 2, except that after drying, the electrode film was heated in air to 200 ^{o}C in a Carbolite CTF 12 furnace, above the melting point of binder, and slowly cooled down to room temperature to promote crystallization (Nakagawa & Ishida, 1973). The cooling rate was ~0.3 ^{o}C/min. When the temperature, *T*, was ~20 ^{o}C below the melting point of a binder component (140 ^{o}C for B01, 140^{o}C for B02, and 80 ^{o}C for B03), the temperature was maintained constant for 1 hour to allow melt crystallization, followed by continued cooling.

Blending B03 with B01 or B02 reduced the amount of unstable material in the binder phase. The thermal treatment was expected to promote the formation of crystalline

phases of PVDF and PVDF-HFP, so that the structural properties were further enhanced (Nakagawa & Ishida, 1973). It has been reported that annealing of the PVDF helped maximize the crystalinity (Nakagawa & Ishida, 1973).

Both B01 and B02 were PVDF, proven stable and durable in the electrochemical environment of LIB cell. They had different molecular weights and structures. As the polymer blend was cooled down, either B01 or B02 would solidify first, since their melting points were much higher than that of B03. As temperature further decreased, B03 molecules would attach onto the PVDF nuclei and the NMC532 microparticles. The PVDF nuclei was expected to increase the crystallinity of the PVDF-HFP, as it was more energetically favorable for the B03 chains to align with the crystalline B01 or B02 phase. As shown in Figure 4.4c and 4.4d, the electrochemical performance of polymer-blend-based LIB cells were comparable with or could be even better than that of B01-based reference cell, by far exceeding the performance of B03-based cell. In general, as the PVDF content in polymer blend increased, the cycling performance was improved. When the PVDF component was B01, as the binder changed from T1-10 to T1-20, the degradation rate was reduced by nearly 40%; as the binder was T1-50, the degradation rate further decreased by another ~20%, lower than yet close to that of B01-based reference cell. When the PVDF component was B02, while the curves of T2-10 based and T1-20 based cells were somewhat similar, as the PVDF content in binder rose to 20%, T2-20 based cell demonstrated the best performance, superior to the reference cell. As the B02 content in polymer blend increased to 50%, the degradation rate of T2-50 based cell slightly increased

to above that of B01-based reference cell, suggesting that the beneficial effects of blending B03 with PVDF had saturated.

DSC analysis results showed that B02 had a higher crystallinity than B01 (Section 4.2.2.1, Table 4.3), probably because that the shorter chains of B02 were less entangled in the melt and could more easily disentangle to form crystalline structure (Whisnant, 2000). Note that crystallinity is not the only indicator for the strength of polymer. In fact, entanglement of longer chains is also an important factor that helps enhance the polymer strength. However, when the PVDF binder is subjected to a solvent, i.e. electrolyte, the amorphous regions swell, and thus the crystalline regions play the major role in supporting the polymer matrix. Therefore, high-crystallinity B02 showed a better performance compared to highly entangled B01.

However, if the crystallinity of polymer binder is too high, it might not store enough electrolyte to maintain a high ionic conductivity across the electrode. With B02 and B03 being immiscible in the blend (see IV.2.2), the nonuniformly distributed B02 crystalline regions might have caused non-uniform lithiation and de-lithiation, leading to stress-concentrations which might have hampered the long-term performance of the electrode. In other words, while a high concentration of B02 in the binder blend should increase the structural integrity and solvent resistance of a regular structural composite, it might have a negative effect on the ionic conductivity and introduce more internal stresses during cycling of the composite electrode. Therefore, the composition of polymer blend must be optimized. According to our testing result, the optimum PVDF content was around 20%, i.e. T2-20.

Figure 4.5 confirms the thermally sensitivity of T2-20 binder, as it showed the lowest heat generation among all the modified-B03 cells in nail penetration test. Compared with a pristine B03-based cell, the peak temperature of T2-20 based cell was higher by only ~10%; the post-peak temperature decrease rate was substantially higher, but it was not the critical element for thermal runaway mitigation. That is, T2-20 based cell generated more heat than B03-based cell within the first 5 min, yet the heat generation was distributed over a relatively long time and thus, did not have a significant effect on the maximum temperature increase. As discussed in Chapter 1, peak temperature increase was the critical parameter to evaluate Joule heating in a shorted coin cell, and in a long run, the normalized total released heat (kJ/Ah) should be the same. The working mechanism of T2-20 should be similar to that of B03, except that the swelling of PVDF-HFP was mitigated by PVDF, so that during normal charge-discharge operation the cathode remained structurally integral.

4.1.3. Optimization of Electrode Composition

To further improve the performance of battery under both normal operation and in mechanical/thermal abuse conditions, we investigated the effect of the contents of binder and carbon black additive(Le, et al., To be published, d). T2-20 exhibited the best performance in both nail penetration and cycling test, hence was selected as the baseline material to be further optimized in this section. In the following discussion, the weight percentage of each component, i.e. active material (AM), binder (B), or carbon black (CB), was measured with respect to the “reference” total mass of solid components, 5 g. The content of active material was fixed at 93 wt.%, or 4.65 g, while the contents of binder and carbon black additives varied. For instance, in a 2wt% B - 2wt% CB electrode, the mass

ratio among its solid components would be AM:B:CB = 93:2:2. The binder and carbon black were measured to desired quantities and added to the powder mixture. The slurry processing, coin cell fabrication and testing were the same as described in Chapter 2.

The first step of optimization was to examine the peak temperature increase recorded in nail penetration test. Next, the samples of the lowest temperature increase would be selected and tested for cycling performance. As shown in Figure 4.6b, the peak temperature increase in reference cell (B01 as cathode binder) was 2.71 ^{o}C, and that in TSB baseline cell (B03 as cathode binder) was 1.73 ^{o}C. Figure 4.6a shows the temperature increase of TSB-modified cells, with various CB and T2-20 contents. The reference point was at 4 wt.% T2-20 and 3 wt.% CB. From the reference point, the contents of TSB and CB were modified.

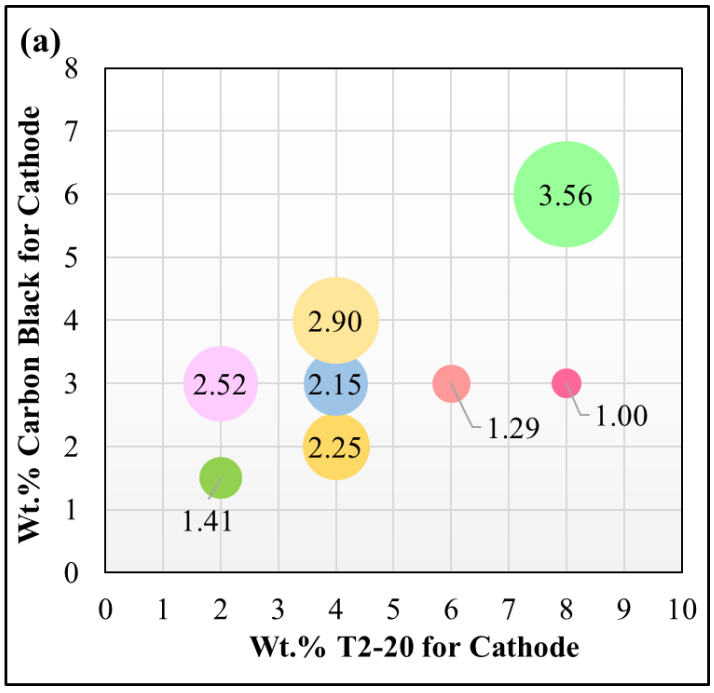

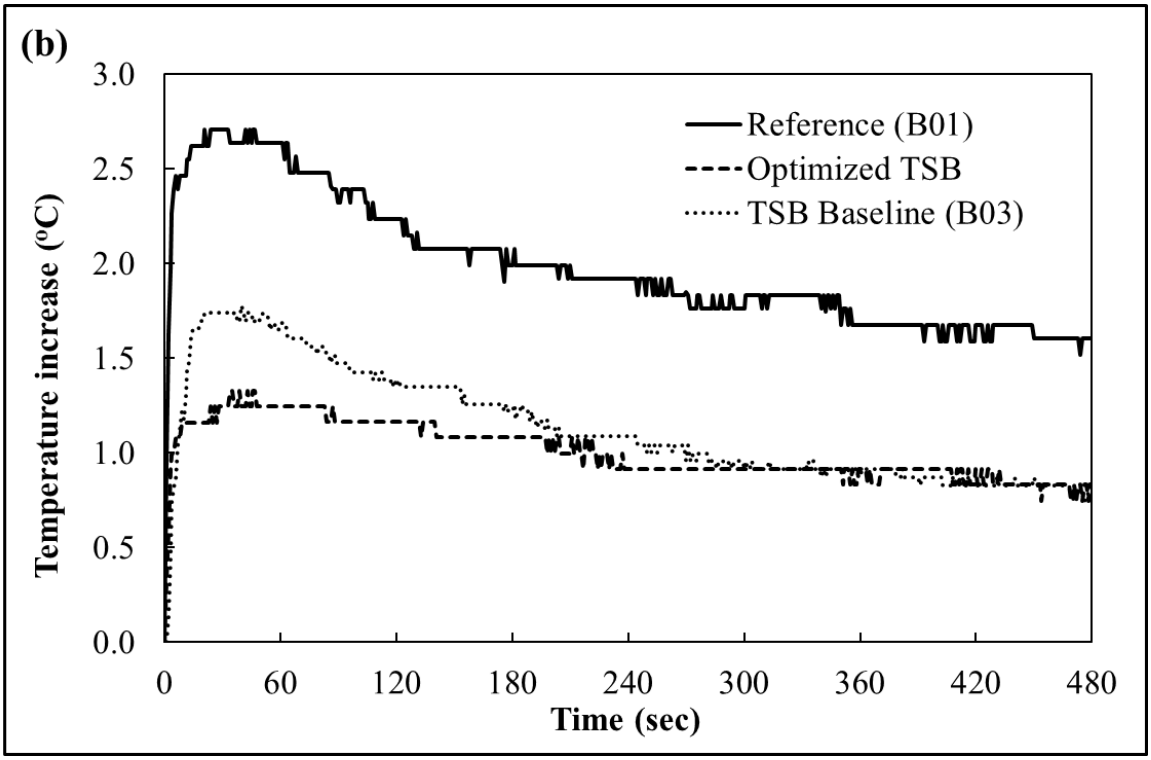

Figure 4.6. Typical temperature increase in nail penetration tests of full cells with 4wt% CMC/SBR (2:2) as the anode binder: (a) Temperature increase chart (°C) for various TSB and CB contents; (b) Comparison among different cathode binders (optimized TSB, baseline PVDF, and PVDF-HFP).

As the testing results showed, the heat reduction effect was improved with increasing TSB content: with a constant 3 wt.% CB and the TSB content ranging from 2 wt% to 8wt.%, the peak temperature increase gradually dropped from 2.52 °C to 1.00 °C. As the TSB:CB mass ratio increased, the electrical conductivity of the TSB/CB network decreased, which in turns reduced the overall conductivity of the composite electrode. In addition, the higher content of TSB, the greater the thermal sensitivity came into effect: As the binder melted and swelled, the conductive CB embedded within the polymer matrix were disconnected (Balakrishnan, et al., 2006). This mechanism raised the concern for electrochemical reactions during normal operation of LIB.

The conductive additive, i.e. carbon black (CB), is critical to the performance of LIB, especially for the cathode, as its active material has a lower electrical conductivity compared to the graphite-based anode (Park, et al., 2010). For an application that requires high energy density such as the energy storage for electric vehicle, a cathode about 70 μm thick normally requires ~3 wt.% carbon black in the composite electrode layer (Singh, et al., 2015). In this study, the range of CB content was from 2 wt.% to 4 wt.%, with a constant 4wt.% TSB (T2-20). Due to restriction in the lower limit of CB content, the trend was somewhat random (Figure 4.6.a). However, an approximately 22% reduction in peak temperature increase (from 2.90 ^{o}C to 2.25 ^{o}C) could be observed as the CB content decreased from 4 wt.% to 2 wt.%. Increasing the CB content would result in a more aggressive heat generation in nail penetration test, due to the increase in electrode conductivity.

Another approach was to maintain a constant TSB:CB ratio at 4:3 w/w, while modifying the content of both components together. As shown in Figure 4.6a, doubling the reference 4wt.% TSB – 3wt.% CB resulted in a much higher heat generation rate in nail induced short circuit, with the temperature increase peaked at 3.56 ^{o}C. The higher binder content might have enhanced the structural integrity of the electrode, making it more stable and more tolerance to the dynamic events in short circuit. As the TSB/CB network remained well connected, short circuit discharge could not be slowed down. In addition, the fact that the temperature increase was even higher than that of the reference B01 based cell indicated that the higher content of TSB/CB (4:3 w/w) conductive network, the more conductive the electrode became. On a side note, this finding might suggest that it is

possible to slightly increase the TSB:CB ratio without having much negative effect on the electrochemical performance of LIB, which would be investigated later.

Reducing the TSB/CB 4:3 by 50% helped limit the peak temperature increase in nail test to 1.41 ^{o}C. The effect was not as significant as increasing the binder content, but still prominent. This was a promising recipe as the conductivity of the TSB:CB network remained unchanged, which would be less likely to have any negative effect on the electrode during normal cycling of the battery.

From the nail penetration testing results, two candidates were selected for cycle life testing: (1) 6wt.% TSB – 3 wt.% CB and (2) 2 wt.% TSB – 1.5 wt.% CB (Figure 4.7a). The cycling performance of the two candidates were compared against the reference cathode (B01 based), the baseline TSB cathode (B03 based), and the T2-20 reference cathode (AM:TSB:CB = 93:4:3). To accelerate the optimization process, the cycling test was first performed at 60 ^{o}C. As mentioned previously, the purpose of the high temperature setting is to speed up the aging process, while still keep it safe within the operational temperature range (Waldmann, et al., 2014).

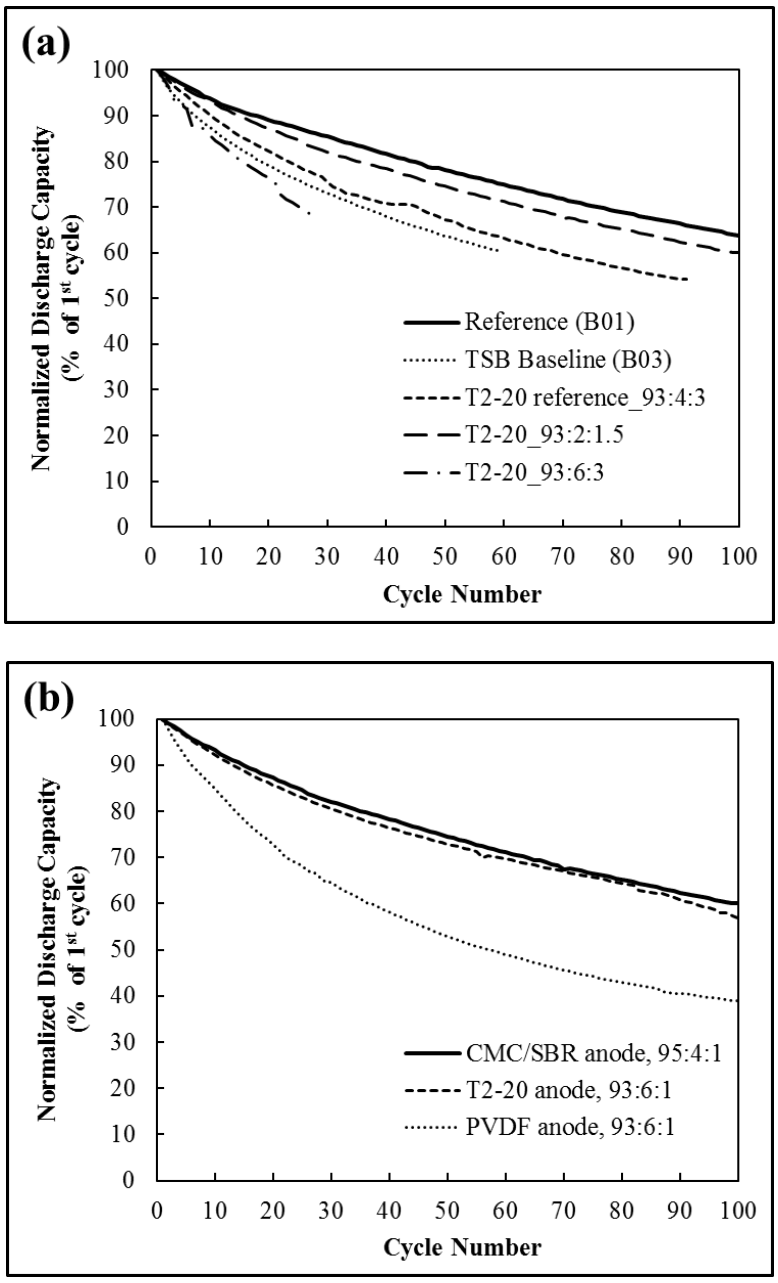

Figure 4.7. Typical cycling performance of full cells at 60 ºC: (a) Comparison between various PVDF/PVDF-HFP blend and CB contents for cathode, with 4 wt.% CMC/SBR (2:2 w/w) as the anode binder; (b) comparison between PVDF, T2-20, and reference CMC/SBR as anode binder, with optimized TSB-based cathode (T2-20; mass ratio = 93:2:1.5)

The T2-20 modified cell with 6 wt.% binder and 3 wt.% CB showed the lowest performance, with the fading rate even higher than that of the TSB baseline (B03) cell.

Low reversible capacity could be observed from the starting cycles, which signaled the low electrical conductivity resulting from the high TSB:CB ratio (2:1). The subsequent rapid capacity loss indicated further damage of the electrical contact due to the relaxation of binder. In contrast with our hypothesis, this result showed that increasing the TSB:CB ratio, even only slightly, i.e. to 2:1, could be detrimental to the electrochemical performance of electrode. As T2-20 is flexible and thermally sensitive, a high content of this binder was unfavorable to the structural integrity of the electrode.

The T2-20 modified cell with 2 wt.% binder and 1.5 wt.% CB showed very stable performance, almost matching with the reference cell (B01). Because the TSB:CB ratio was the same as that of the reference cell (4:3 w/w), the conductivity of the TSB:CB network remained the same. The binder and CB contents were still in the reasonable range, so the overall conductivity of electrode was not largely affected. As the content of TSB was reduced, the swelling effect during cycling was reduced. Further reducing the content of TSB/CB would lower both ionic conductivity and structural integrity of the electrode. An electrode made with 1wt.% TSB and 0.75 wt.% was produced, but showing very poor adhesion to the current collector, rendering it unsuitable for actual production.

It was also of our interest to study the effect that the T2-20 binder may have on anode. We prepared the anodes with different types of binder, including T2-20, and performed cycle life test at 60 ^{o}C (Fig. 4.7b). The reference binder for anode was CMC/SBR at 2:2 w/w ratio, and the ratio among the anode components was AM:B:CB = 95:4:1. The PVDF binder for anode was Kynar HSV 900, a high molecular weight PVDF homo-polymer obtained from Arkema America. As the particle size of the anode active

material was large (~20 μm), the purpose of using a high-M_W polymer was to enhance the bonding among AM particles.

The sample cell with PVDF-based anode showed a much higher fading rate from the starting cycles, and continued to progress through 100 cycles (Fig. 4.7b). Surprisingly, the sample cell with T2-20 modified anode showed good cycling performance, almost reaching that of the CMC/SBR reference anode. This was attributed to the increased crystallinity of T2-20. While T2-20 was designed to be thermally sensitive in cathode, its crystallinity might have been enhanced in the graphite anode. Anode graphite particles were approximately twice as large as the NMC532 particles, and thus, might have provided better nucleation sites for crystalline phase formation of linear PVDF, B02 (Le, et al., To be published, d). However, the performance of T2-20 anode was not superior to that of the CMC/SBR anode. Taking into account other factors such as cost and toxicity of the NMP solvent during processing of PVDF-based binder, CMC/SBR was still more favorable as the binder material for graphite anode.

To test the long term performance of cells with the optimized cathode composition, i.e. AM:B:CB = 93:2:1.5, with T2-20 binder, full cells with CMC/SBR anode were tested at 1-C current rate at room temperature for 300 cycles (Figure 4.8). The result confirmed that the T2-20 binder, at optimized electrode composition, indeed enhanced capacity retention of the electrode. The initial reversible capacities of reference cell and optimized TSB-modified cell at the first measured cycle were 155 and 148 mAh/g of active material, respectively. After 100 cycles, the reversible capacities reduced to 132 and 130 mAh/g of active material. Even though the starting reversible capacity of the optimized TSB cell was

lower than that of reference cell, the number was within reasonable range as reported for the NMC532 active material cycled at 1-C rate (Hou, et al., 2014). The higher initial capacity of the reference cell was attributed to the side reactions as the stiff B01 binder matrix started to loosen up after several repeated charge-discharge cycles. These side reactions caused a more rapid capacity fade compared to the optimized TSB cell within the first 100 cycles. The capacity retentions were 85% and 88% for the reference and modified cells, respectively.

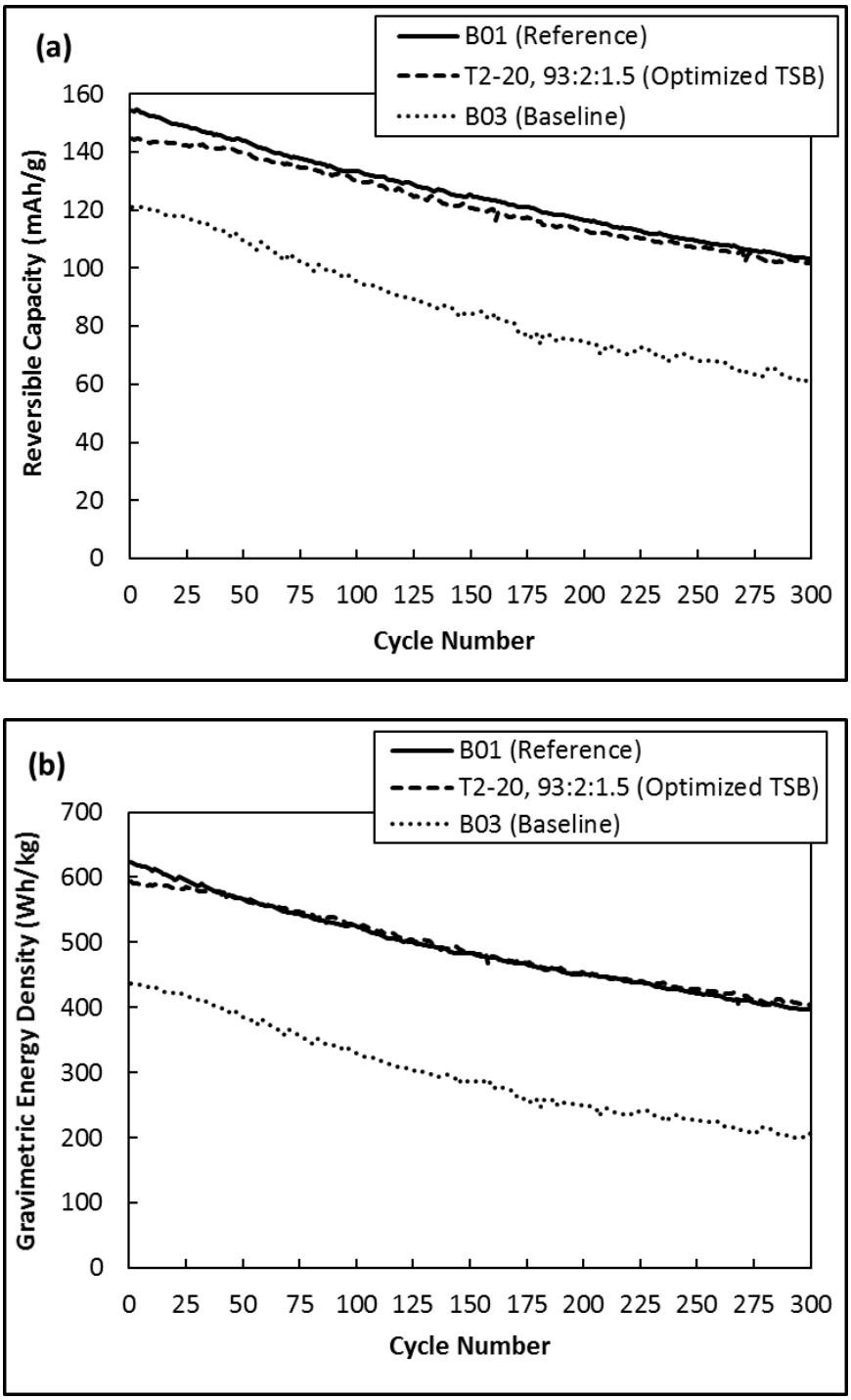

Figure 4.8. Typical cycling performance of full cells with CMC/SBR anode at ambient temperature (25 ^{o}C): Reversible capacities of reference and TSB-based cells; (b) gravimetric energy densities of reference and TSB-based cells

While the binder content must be sufficiently high to hold the composite electrode together, the reduction of the flexible B03 phase also reduced the structural instability of the system. In addition, while fixing TSB:CB mass ratio at 4:3 ensured electronic conductivity of the binder-CB matrix for satisfactory cycling performance, the varied content of binder might has also influenced its crystallization process. During slurry processing of the electrode, while the amount of the major components, i.e. active material and solvent, remained unchanged, and the mass and particle size of carbon black could be negligible, the amount of binder varies, resulting in a distinct polymer-to-solvent ratio. With the 'reference' ratio, the polymer binder takes up about 10 wt.% of the NMP solvent/polymer solution (see II.1.1). With the optimized TSB ratio, the polymer binder takes up about 5 wt.% of the NMP/polymer solution. A previous study on the effect of PVDF concentration in DMF solvent showed that when the PVDF concentration was 10wt% and above, the viscosity of the solution was high, restricting chain alignment and thus, resulting in a smaller spherulite size and a lower crystallinity (Ma, et al., 2007). In short, as the content of the relatively unstable B03 was reduced and reinforcement was enhanced with higher-crystallinity B02 phase, the electrode became more structurally integral, leading to improved cycling performance of the battery cell.

4.2. Materials Characterization

4.2.1. ESEM Analysis

Environmental Scanning Electron Microscopy (ESEM) analysis was performed on the reference and B03 based cathodes at different stages of nail penetration. As shown in

Figures 4.9a and 4.9b, no evident defects could be detected in the two electrodes after charging. The active NMC532 particles were densely packed in a similar way. Note that B03 distributed more uniformly around the NMC532 particles, probably because B03 interacted with the NMP solvent more actively during slurry processing and it was also more deformable. The PVDF reference binder exhibited a higher resistance to solvent and calendaring. As a result, 1-2 μm large microscopic voids could be occasionally observed. The micro-voids did not affect the electrochemical performance of the reference cathode, due to their small size and low density, and also thanks to the sufficient binder strength.

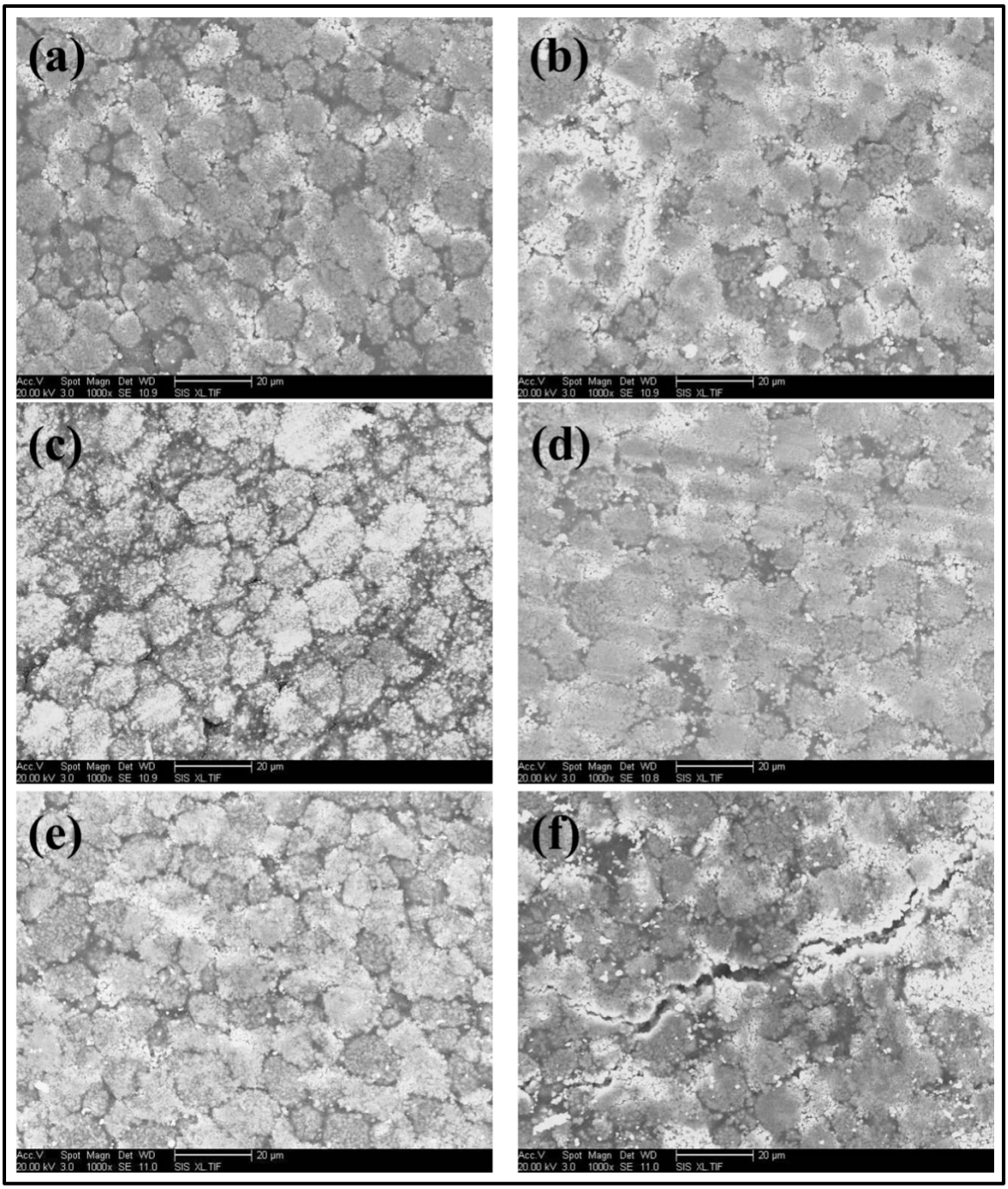

Figure 4.9.ESEM images of reference positive electrodes (a, c, e) and B03-based positive electrodes (b, d, f) at different stages: after cycling and charging (a,b), after preheating at 110^{o}C (c, d), and after nail penetration, more than 0.5 cm away from the nail (e, f). The magnification was 1000 times.

After preheating, considerable swelling of B03 was observed. The binder-filled gaps among NMC532 particles became prominent (3-5 μm) in the B03 based cathode (Fig. 4.9d), while the reference PVDF binder was thermally stable up to 155^{o}C and its microstructure remained unchanged (Fig. 4.9c). Recall that even though both reference and B03-based cells showed slight voltage drops after pre-heating, their voltages were stable for at least 10 min after air-cooling, indicating that even though the microstructure of the B03 electrode had been altered, its ability to host charges was not largely affected. However, the B03 swelling damaged the electrical contact between the AM particles and the binder-CB phase. In addition, preheated B03 became much weaker and was more prone to separation upon the nail loading. Figure 4.9f, which was taken far away from the nail, shows a ~2 μm gap between the separated AM particles in the B03 electrode. In contrast, the bonding among AM particles and CB remained intact in the reference electrode (Fig. 4.9e).

Figure 4.10 shows the B01 and T2-20 based cathodes, with standard composition, at different stages of nail penetration. As shown in Figures 4.10a and 4.10b, again no evident defects could be detected in the two electrodes after charging. Similar to the case of B03, the T2-20 binder also distributed more uniformly around the active NMC532 particles. After preheating, considerable swelling of T2-20 was also observed. The binder-filled gaps among NMC532 particles could be up to 10 μm in the T2-20 based cathode (Fig. 4.10d). Even though the gaps between NMC532 particles appeared to be larger in T2-20 based electrode (Fig. 4.10d) than in B03 electrode (Fig.4.9d), the number of swollen gaps per area was lower. This could be attributed to the immiscibility of the B02 phase and

B03 phase in the T2-20 blend (see section 4.2.2.1). The difference in size, number and distribution of binder filled gaps rendered T2-20 binder less effective in heat mitigation than B03 (Figure 4.5). In these swollen binder - carbon black filled regions, both binding strength and electrical conductivity were reduced. Due to the less uniform distribution of weakened swollen binder regions, the T2-20-based electrode was still relatively structurally stable under short discharge. In contrast to the case of B03-based electrode, the T2-20 based electrode showed almost no prominent cracks after nail penetration test (Fig. 4.10f). Therefore, the reduction in temperature increase profile of T2-20 based cell (Figure 4.5) could be largely attributed to the increase in electrical resistivity.

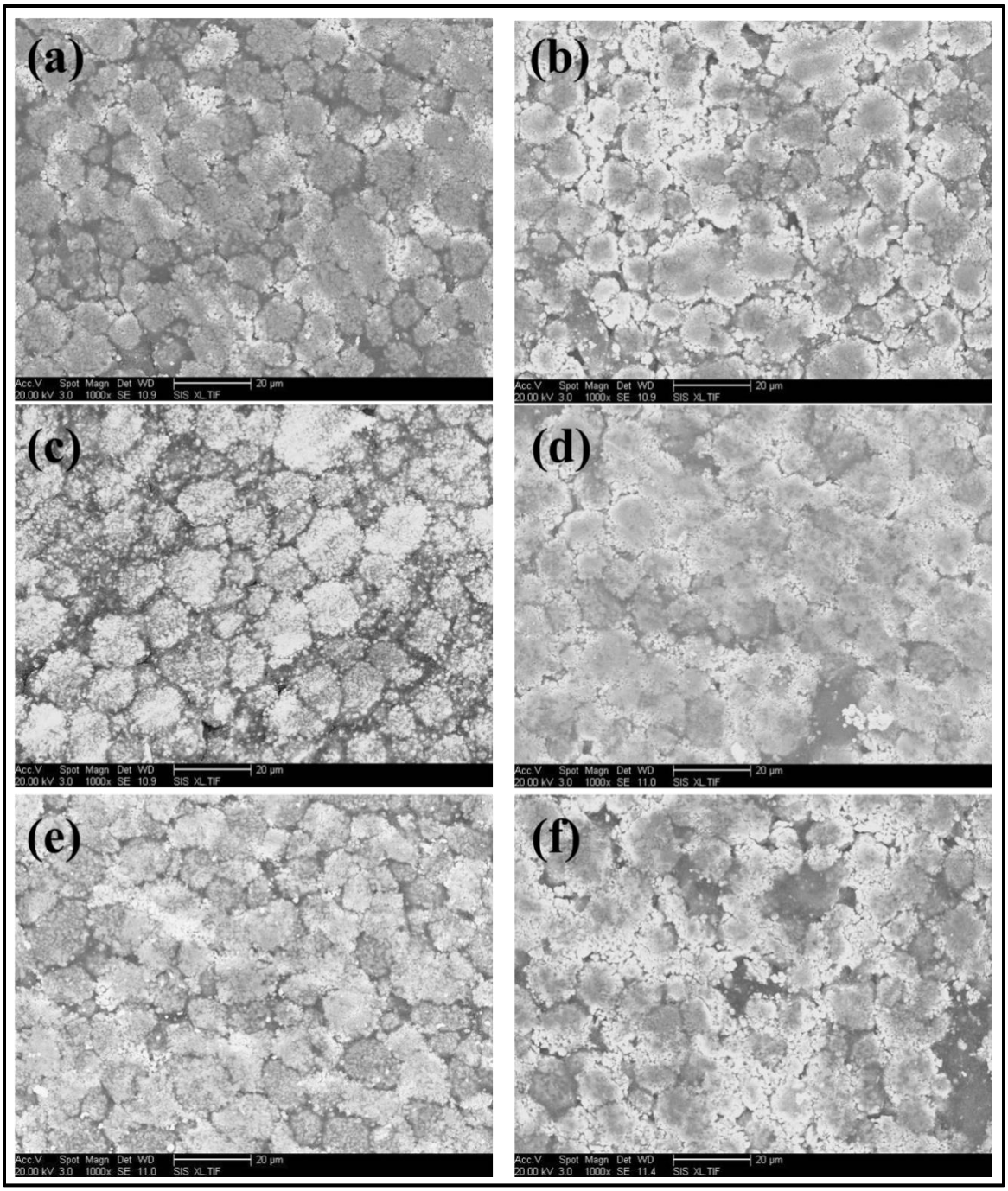

Figure 4.10.ESEM images of reference positive electrodes (a, c, e) and T2-20 based positive electrodes (b, d, f) at different stages: after cycling and charging (a,b), after preheating at 110^{o}C (c, d), and after nail penetration, more than 0.5 cm away from the nail (e, f). The magnification was 1000 times.

4.2.2. DSC PROFILES

4.2.2.1. EFFECT OF HFP-CONTENT

Figure 4.11 shows the Differential Scanning Calorimetry (DSC) results of the reference PVDF binder and the PVDF-HFP binders with varied HFP contents, from 40^{o}C to 200^{o}C, at 10 ^{o}C/min. Table 4.2 summarizes their thermal properties obtained from the DSC analyses. The DSC curve of the reference PVDF binder contained an endothermic peak at ~167 ^{o}C, associated with the melting initiated at around 150^{o}C and ended at 170^{o}C; the peak was quite sharp and narrow. For every TSB, the DSC curve demonstrated a broad shoulder with a few secondary endothermic peaks before the main peak was reached. The melting points of TSB were significantly lower than that of PVDF. The shapes of the melting peaks were related to the variation in crystallinity. The reference PVDF was of a narrower distribution of the sizes of semi-crystalline areas, due to the refined molecular weight and the simpler molecular structure. The PVDF-HFP copolymers tended to have broad distributions of crystalline phase sizes, due to the broader variations in molecular weight and the HFP groups that hinder the polymer chains from aligning with each other (Blaine & Waguespack, TA276). As a result, a larger population of smaller-sized semi-crystalline areas was formed in TSB, and melted at lower temperatures.

Table 4.2. Thermal properties of cathode binders, obtained from the DSC analyses.

Binder Type	Melting Point (°C)		Heat of Fusion, ΔH_f (J/g)	Crystallinity (%)
	Onset	Peak		
B01	156	166	44	42
B05	151	161	41	-
B04	113	148	34	-
B03	82	130	21	-

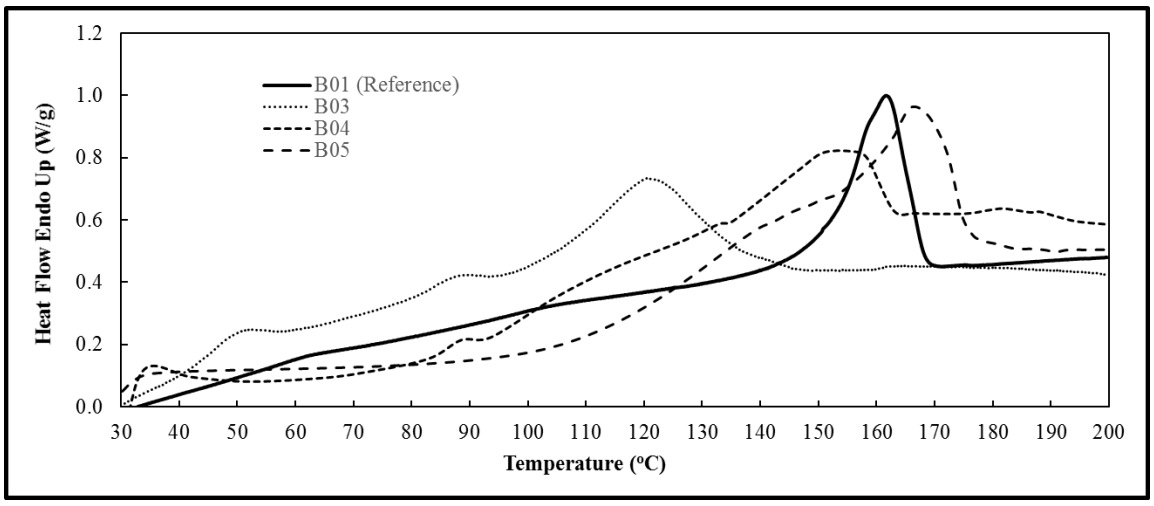

Figure 4.11. Typical DSC curves of pristine (as-received) cathode binders.

With the reference heat of fusion being set to 105 J/g for 100% crystalline PVDF(Teyssedre, et al., 1993), it was calculated that the PVDF reference binder under investigation has a crystallinity of 42% (Table 4.2). Theoretically, PVDF-HFP should not be able to achieve 100% crystallization, and thus, the exact reference heat of fusion was unavailable. Nevertheless, for the purpose of self-comparison, the crystallinities of PVDF-HEP were approximately assessed by using the same reference heat of fusion of 105 J/g. As shown in Table 4.2, it was evident that the higher the HFP content, the lower the heat

of fusion and melting temperature would be, indicating that the polymer tended to be more amorphous. It is important to note the increasing slopes in the DSC curves after the major melting events have occurred. The slope became steeper with a higher content of HFP, which could be attributed to the higher volume expansion associated with melting. The expansion of the polymer sample built up an inner pressure, causing the deformation of the aluminum pan in the DSC Analyzer.

The PVDF reference binder offered a high binding strength to the AM and CB components. However, the onset of melting of PVDF binder occurred at a temperature much higher than the threshold point of thermal runaway (~110^{o}C). For the TSB, even though the main melting peak, related to the melting of the van de Waals bonds among the most abundant groups of the longest chains, occurred at a relatively high temperature, the broad shoulder showed up at ~80 ^{o}C; i.e the binder worked normally in the working temperature range of LIB cells while began to soften before thermal runaway accelerated.

4.2.2.1. Effect of Modification Methods on Baseline TSB Material

Figure 4.12 shows the DSC curves of pristine and low-M_W PVDF materials. It appeared that the peak melting temperatures of R1 and R2 were shifted to the lower end, as they should be. Note that the melting point of the as-received B02 agreed with supplier's data, whilethe melting point of the as-received B01 was lower. This could be attributed to the higher polydispersity of B01. That is, B01 might have possessed a wider distribution of M_W. This could also be the reason that refinement was more effective for B01 than for B02, as shown by a more pronounced shift of its melting peaks (Figure 4.12) and a more

significant temperature reduction in nail test (Figure 4.5).However, the shifts were only a few ^{o}C, quite small compared with the difference between the original peak melting temperatures and the critical point of LIB thermal runaway (~150 ^{o}C). This result explained the low effectiveness of the refined, low-M_W PVDF materials in the nail penetration test.

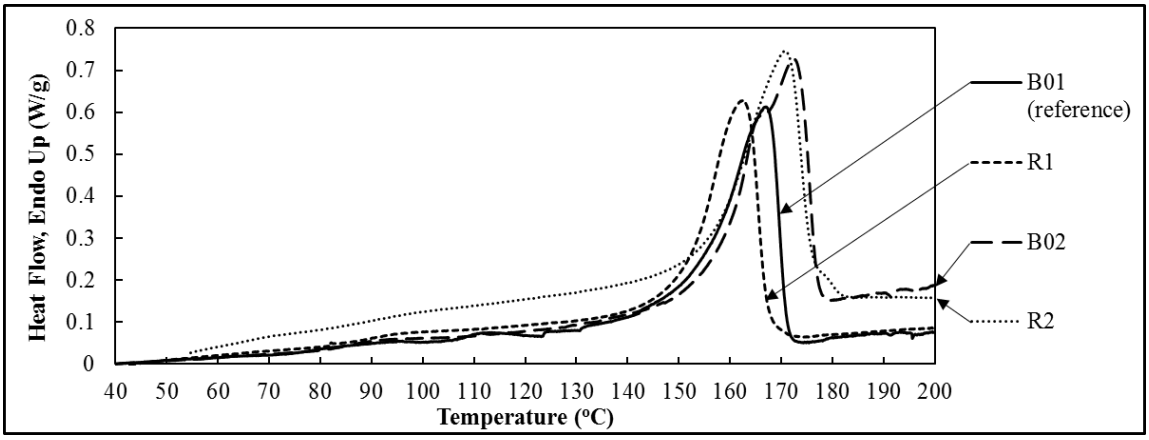

Figure 4.12. Typical DSC curves of PVDF binders: pristine (B01, B02) and refined (R1, R2).

Figure 4.13 shows the DSC measurement results of PVDF binders and PVDF/PVDF-HFP blends. The DSC curve of B03 contains broad shoulders for both dry (Group 1) and electrolyte-soaked (Group 2) films. This thermal response is usually attributed to the wide range of molecular weight: the shorter polymer chains form smaller crystalline areas that melt at lower temperatures; longer chains form larger crystalline areas that melt at higher temperatures (Gray, 1970).Melting of dry B03 began at about 80 ^{o}C. When soaked in electrolyte, the polymer became less stiff; the melting temperature range was 15-20 ^{o}C lower, and the heat absorption was much reduced. More importantly, the electrolyte-soaked B03 films was softened at ~50 ^{o}C, which explained the poor cycle lives of LIB cells based on pristine B03. Clearly, the pristine B03 offered relatively low strength,

low solvent resistance, and low thermal stability; it had a relatively broad M_W distribution, which was likely one of the reasons of the fast degradation rate of the B03-based LIB cells.

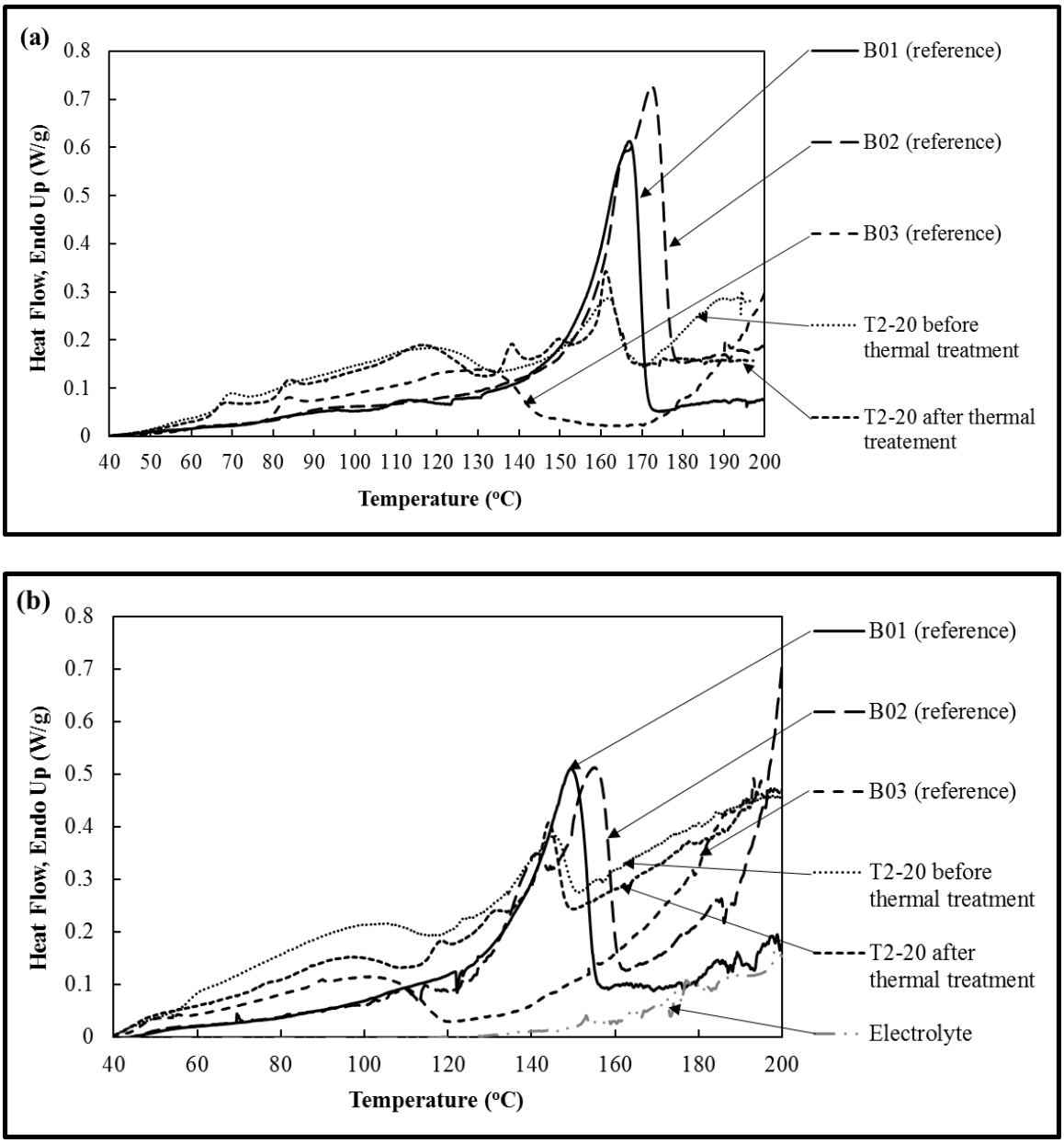

Figure 4.13. Typical DSC curves of cathode binders, comparison between thermally treated PVDF/PVDF-HFP blends and baseline PVDF, PVDF-HFP materials: (a) Group 1 consisted of dry polymer films and (b) Group 2 consisted of polymer films soaked in electrolyte.

The DSC measurement results confirmed that the thermal treatment indeed helped increase the crystallinity in binder phase. First, regardless of the thermal treatment and presence of electrolyte in the system, each of the B02/B03 blends exhibited two separately endothermic melting peaks, associated with separate melting behaviors of B03 and B02 (Figure 4.13). Such melting behaviors indicated that the two components in the blend, i.e. B03 and B02, were immiscible to each other (Sahagian & Bair, 2012). In fact, immiscibility was desirable to preserve the thermal instability of B03 for thermal runaway mitigation. The independent melting behaviors of B02 and B03 phases also renders it convenient to assess the crystallinity of each component separately. The crystallinity was calculated from the heat of fusion, ΔH_f. The higher the value of ΔH_f, the higher the crystallinity the polymer has (Gray, 1970). While this value might be directly computed for pure polymer samples by DSC scans, the true value of ΔH_f for each component in polymer blend should be re-calculated according to the content of the component in the blend. The content of electrolyte in the soaked samples had also been subtracted before the scan. For instance, a T-20 sample contains 20 wt.% of B02 phase, and the DSC scan for this sample gave a raw value of 9.72 J/g for the ΔH_f of B02 phase. Therefore, the actual ΔH_f value of B02 phase in this case was (9.72 J/g)/(20%) = 48.6 J/g.

With thermal treatment, the crystallinity of the B02 phase in the T2-20 polymer blend increased by 73% in dry polymer film, and by 59% in polymer film soaked with electrolyte, as shown in Table 4.3. The increase in crystallinity of B02 was mostly associated with the formation of relatively small-sized crystalline areas, reflected by the smaller melting peaks in the DSC curves within the 132-155 ^{o}C range for dry T2-20 (Fig.

4.12a) and within the 115-135 ^{o}C range for soaked T2-20 (Fig. 4.12b). The DSC curves also support our hypothesis that the PVDF offered nucleation sites for the crystallization of PVDF-HFP: smaller crystalline areas of B03 were indicated by the smaller melting peaks in the DSC curve of dry T2-20 within the 65-88 ^{o}C range. Interestingly, the crystallinity of B03 phase remained relatively constant (Table 4.3), and the smaller B03 crystalline areas vanished when the polymer blend was soaked in electrolyte, possibly due to the solvent attack. The solvent attack was also evident in PVDF, but much less severe: the heights of smaller melting peaks of B02 were reduced, yet the shapes of these peaks were prominent. Regardless, an increase of 59% in crystallinity of B02 phase in the electrolyte-soaked T2-20 blend clearly offered sufficient structural support to the composite electrode over repeated charge-discharge cycles (Figures 4.6d, 4.7 and 4.8).

Table 4.3. Average heat of fusion of cathode binders, ΔH_f(J/g)

Sample Code		**Group 1 – Dry Polymer Films**	**Group 2 – Polymer Films Soaked in Electrolyte**
B01		44.1	29.4
B02		40.3	38.6
B03		20.7	13.8
T2-20, before thermal treatment	B02 phase	35.7	30.6
	B03 phase	18.6	10.8
T2-20, after thermal treatment	B02 phase	61.8	48.6
	B03 phase	19.9	10.0

After thermal treatment, the major melting peaks of the B03 phase in the T2-2 blend, both in dry and electrolyte-soaked samples, slightly shifted to the left, suggesting that

melting of semi-crystalline B03 occurred at a slightly lower temperature. For polymer in dry state, melting still completed well over 110 ^{o}C; the benefit became provident for the polymer films soaked in electrolyte, as the melting peaks were reduced by ~20 ^{o}C.As a result, the entire melting curve of the B03 phase in the thermally treated T2-20 shifted to below 110 ^{o}C, enhancing the thermal sensitivity of the binder (Figures 4.2 and 4.3b).

4.2.3. Swelling Index Measurement

Swelling index (SI) measurement provided additional information about the working mechanism of TSB (Table 4.4). Overall, the dissolution and swelling of all the polymers in the current investigation were quite high. The final dried polymer gel exhibited a mass loss compared to the initial mass of the polymer sample, suggesting dissolution of the polymer into the electrolyte solvent had occurred. The polymer samples of SI measurement were processed without any active material or carbon black. That is, there were fewer number of available nucleation sites and reinforcement against dissolution and swelling in excess solvent(Miyazaki, et al., 2008; He, et al., 2010). Therefore, the measurement results were only valid for comparison among the bulk polymers, and might not be directly related to actual dissolution and swelling behaviors of the polymers in composite electrodes in actual LIB environment.

Table 4.4. Swelling indices of cathode binders.

Polymer	At Room Temperature		At 60°C		At 80°C		$T_{m,\ onset}$ (°C)
	% dissolved	SI	% dissolved	SI	% dissolved	SI	
B01	28.31	6.55	23.90	5.37	27.41	5.83	~140
B02	21.77	4.82	23.20	4.89	20.73	5.99	~147
B03	34.22	7.95	61.80	11.90	100.00	-	~85
					-	21.42	
T2-20	26.60	5.94	49.06	6.63	58.00	9.65	

At room temperature, the PVDF materials, B01 and B02, showed mild dissolution and swelling, while the high HFP-content copolymer, B03, showed more prominent dissolution and swelling behaviors, which was associated with the high concentration of amorphous phase. Such prominent swelling even at ambient temperature explained the low capacity and energy density of the B03-based cell (Fig. 4.8). When blended with B02 at the optimized ratio and subjected to the thermal treatment to form T2-20, however, the dissolution and swelling behavior at room temperature could be much retrained to the same level as that of the PVDF materials, i.e. B01 and B02, and thus helped stabilize the cycling performance of T2-20 based cells (Figure 4.8).

As the temperature increased, the dissolution and swelling of B03 became more and more severe, while B01 and B02 remained mostly unaffected. This explains the large capacity fading of the B03-based cells. At 60 °C, the swelling index of B03 increased by about 50 % and was over twice of the swelling indices of B01 and B02. Meanwhile, the

swelling index of T2-20 increased by only 12 %, and only about 23 % higher than that of the reference B01 binder. The improved swelling resistance could be attributed to the presence of B02 in the system, aided by the thermal treatment that increased the crystallinity. It is also worth noting that the swelling indices of B02 at room temperature and at 60 ^{o}C were both lower than those of B01 at the same temperatures, respectively, which agreed with the DSC results that the crystallinity of B02 was higher (Table 4.3). Interestingly, the dissolution level of T2-20 at 60 ^{o}C, while was improved from the pristine B03, was still about twice of those of PVDF materials. This result provided a quantitative explanation as to why reducing the content of T2-20 by 50 % would optimize the TSB composition, limiting binder dissolution and swelling for long term cycling performance (Figures 4.7a and 4.8).

4.2.4. Internal Resistance Measurements

The motivation of the internal resistance (R_I) measurements for the battery cells was to detect any difference in the structures of the reference and the modified electrodes at different states. If there was swelling and/or cracking within the composite electrode, or if there was any debonding between the electrode layer and the current collector, the internal resistance should rise. For the reference cathode half-cell, the cathode binder was B01. For the optimized TSB cathode half-cell, the cathode binder was T2-20, and the mass ratio among the solid components was AM:B:CB = 93:2:1.5. In general, the values of internal resistance were large for coin cells due to the limitations on cell geometry and

components. Thicker electrodes also imposed greater resistance on the mass transports of lithium ions and electrons (Singh, et al., 2015).

As shown in Table 4.5, the initial condition of the reference and the TSB cells were similar, as their R_I values were about the same and lower than 10 Ω. Upon preheating, the internal resistances increased to 143.3 Ω and 100.6 Ω for the reference cell and TSB cell, respectively. Both cell types exhibited a large increase in internal resistance due to the expansion of the cell components and boiling of electrolyte. Surprisingly, the average internal resistivity of the reference cell after preheating was higher than that of the TSB cell. After being impacted, however, the internal resistance of the TSB cell increased by more than three times from its value after preheating. Meanwhile, the internal resistance of the reference cell also increased due to damaged contact between the cell components, but at a much lower degree.

Table 4.5. Internal Ohmic resistance (R_I) of cathode half-cells

Cell condition	Reference cell	Optimized TSB cell
Cycled and charged to 4.6 V	7.3 Ω	8.2 Ω
Preheated to 110 ^{o}C	143.3 Ω	100.6 Ω
Impacted (without indenter)	232.2 Ω	341.5 Ω

In combination with DSC and SI measurements, the R_I values suggested that while preheating might not have imposed significant damage on the positive electrode, it could have melted and weakened the TSB binder, which in turns altered the microstructure of the composite electrode. As the R_I values of impacted cells suggested, the major structural

damages might have taken place only when an external load, i.e. impact or high current discharge via nail penetration, was applied on the weakened composite electrode.

ACKNOWLEDGEMENT

This research is supported by the Advanced Research Projects Agency – Energy (ARPA-E) under Grant No. DE-AR0000396, for which we are grateful to Dr. Ping Liu, Dr. John Lemmon, Dr. GrigoriiSoloveichik, Dr. Chris Atkinson, and Dr. Dawson Cagle. Special thanks are also due to Dr. Jiang Fan and Dr. Dengguo Wu for the help with lithium-ion battery design and processing.

Chapter 4, in part, is reproduced from the under-review manuscripts: (1) Le, Anh V.; Wang, Meng; Shi, Yang; Noelle, Daniel J.; Yoon, Hyojung; Meng, Ying S.; Wu, Dengguo; Fan, Jiang; Qiao, Yu. "Heat Generation of Mechanically Abused Lithium-Ion Battery Cell Based on Thermally Sensitive Cathode Binder;" (2) Le, Anh V.; Wang, Meng; Noelle, Daniel J.; Shi, Yang; Yoon, Hyojung; Zhang, Minghao; Meng, Ying S.; Qiao, Yu. "Effects of Macromolecular Configuration of Thermally Sensitive Binder in Lithium Ion Battery." The dissertation author was the primary author of these manuscripts.

Chapter 4, in part, is currently being prepared for submission for publication of the material: (1) Le, Anh V.; Wang, Meng; Noelle, Daniel J.; Shi, Yang; Meng, Ying S.; Qiao, Yu. "Mitigating Thermal Runaway of Lithium-ion Battery by Using Thermally Sensitive Binder;" (2) Le, Anh V.; Chung, Hyeseung; Wang, Meng; Noelle, Daniel J.; Shi, Yang; Yoon, Hyojung; Meng, Ying S.; Qiao, Yu. "Effects of Electrode Composition on Lithium-ion Battery Based on Thermally Sensitive Binder." The dissertation author was the primary investigator and author of these manuscripts.

CHAPTER 5– HIGH-ENERGY BATTERY CELLS

5.1. MATERIALS

Near-future electric vehicle (EV) demands higher specific energy and energy density, longer cycle life, and improved safety of lithium-ion battery (LIB). In order to investigate the compatibility of thermally sensitive binder (TSB) with high-energy battery chemistry, we tested LIB cells based on novel high-voltage cathode materials provided by the Laboratory for Energy Storage and Conversion (LESC) at the University of California - San Diego. The material synthesis performed at LESC was led by Professor Y. Shirley Meng, aiming to increase the energy density of the active material by enhancing its performance during high-voltage operation. The high-energy cathode active materials (AM) under investigation included lithium-rich layered oxide (LRLO), polyol-synthesized lithium nickel manganese oxide (*P*-LNMO), and polyol-synthesized lithium nickel manganese cobalt oxide (*P*-NMC333). The raw NMC333 material was obtained from MTI (EQ-Lib-LNCM111). The operating voltage windows, theoretical capacities, and particle sizes of the high-energy materials are listed in Table 5.1.

The TSB used in the high-energy cells was T2-20. Among all the thermal-runaway mitigation (TRM) techniques discussed in previous chapters, T2-20 demonstrated the best performance in terms of both the TRM effectiveness and the cycling performance. The reference binder material was conventional PVDF. The tests were performed on cathode half cells. For the reference cathode, the mass ratio among the solid components was AM:Binder:carbon black (CB) = 80:10:10. For the T2-20 based cathodes, two different

ratios, 80:10:10 and 93:4:3, were investigated. Thermal treatment was performed on the T2-20 based electrodes, following the procedure described in Chapter 2. After vacuum drying, the electrode film was calendered, cut into small electrode discs and assembled into half cells, following the previously described procedure (Chapter 2).

In attempt to investigate the compatibility of TSB with other TRM techniques, the *P*-LNMO slurry was cast on debossed current collector, another innovation which had been shown to effectively shut down thermal runway (Qiao, et al., 2016; Wang, et al., 2016). The debossed current collector was prepared by Mr. Meng Wang at the Multifunctional Materials Research Laboratory (MMRL), University of California – San Diego. All other slurries were cast on regular aluminum current collectors. Slurry processing was performed by Dr. Hyojung Yoon and Ms. Hyeseung Chung at LESC, using the binders and current collectors provided by MMRL. We performed thermal treatment on the dried TSB-based electrode films and calendered the treated films following the procedures described in Chapter 2. Coin cell fabrication and cycle life characterization were performed by LESC.

Table 5.1. High-energy cathode materials (LESC).

Material	**Operating Voltage *(V)***	**1st Cycle Reversible Capacity *(mAh/g)***	**C-rate**	**Particle Size *(μm)***	
				Primary	**Secondary**
LRLO	2-4.85	250	C/3	n/a	10-20
P-LNMO	3.5-4.85	120	C/3	0.15	n/a
P-NMC333	2.5-4.7	175	1C	0.15	n/a

5.2. Cycle Life Testing

Figure 5.1 compares typical cycling performance of LRLO cells with 10 wt% reference PVDF and 4 wt.% TSB binders. The LRLO cathode half-cell were charged-discharged between 4.8–2.0 V at C/3 rate. The TSB based LRLO cathode cells exhibited much lower Coulombic efficiency at 55.7 % (Figure 5.1b), compared to 79.3 % of the reference cells based on conventional PVDF (Figure 5.1a), which resulted into the lower reversible capacity from the starting cycles. It may be attributed to the more active interaction between electrolyte and the highly amorphous regions of TSB at the high operating voltage (over 4.7 V), forming thicker SEI layers. This phenomenon could be observed via a much longer charging time, i.e. higher charge capacity, in the first cycle of the TSB based cell. Regardless, the capacity retention of the TSB-based LRLO cell was quite good, indicating the satisfactory compatibility of the TSB with the high-energy LRLO material (Figure 5.1c).

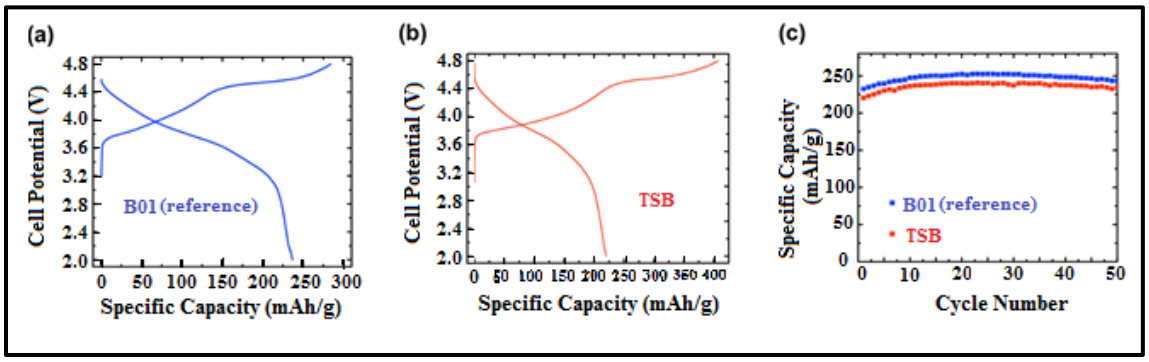

Figure 5.1. First cycle voltage profiles of (a) PVDF binder and (b) T2-20 binder coin cells. (c) The cycling performance of coin cells with LRLO cathodes based on different binders (Figure courtesy of Dr. Hyojung Yoon)

Figure 5.2a illustrates the first electrochemical charge and discharge voltage profiles for the *P*-LNMO based cathode half cells with 10 wt% conventional PVDF and T2-20 binders. Two different TSB contents were tested for the TSB electrodes: 10 wt% and 4 wt% T2-20. The voltage window was 3.5-4.85 V and the constant current rate was C/3. With 10 wt% TSB, the initial capacity of the coin cell was about the same as that of the reference cell, but the capacity degraded continuously over 100 cycles (Figure 5.2b). After the first 100 cycles, the capacity retention of a 10 wt% T2-20 cell was only 81.7 %, compared to 92.8 % for a reference cell based on conventional PVDF binder. It should be related to the thicker and more uniform SEI layer formed through the more active interaction between TSB and electrolyte, which led to a lower electrical conductivity of electrode as cycling proceeded. With 4 wt.% TSB, the charge-discharge profiles of the TSB-based cell was quite similar with that of the reference cell, and the capacity retention was much-improved. Even though the cycling performance was somewhat less stable compared to that of the reference cell, the TSB cell retained 90.5 % of the initial capacity after 100 cycles (Figure 5.2b). This result agreed with our previous study on optimized binder and carbon black content for the TSB system (Chapter 4). That is, the reduction of TSB content by ~50% (from 10wt% to 4wt%) helped stabilize the cycling performance of the electrode.

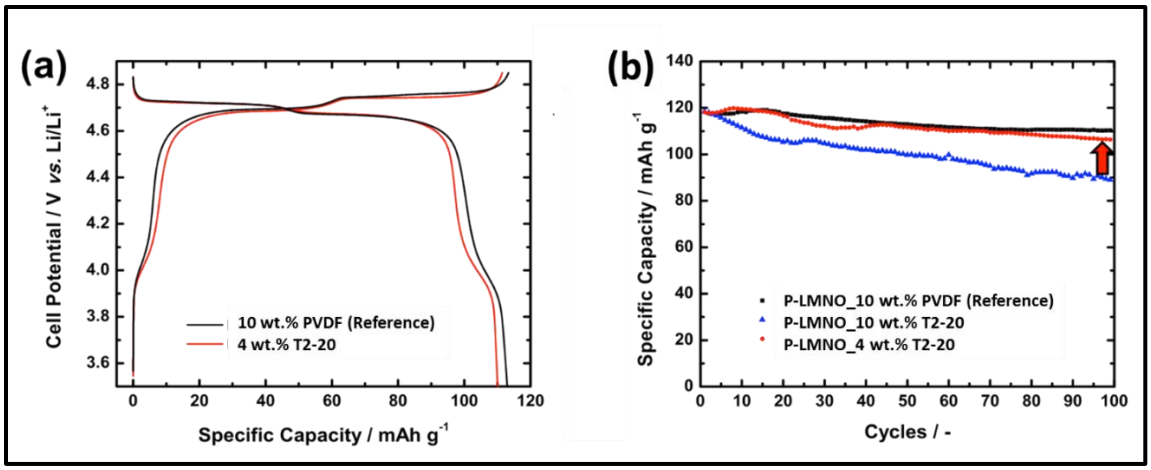

Figure 5.2 (a) First cycle voltage profiles and (b) cycling performance of the *P*-LNMO cathode coin cells based on different binders. (Figure courtesy of Dr. Hyojung Yoon)

Figure 5.3 shows the typical cycling performance of the reference and the modified cells based on *P*-NMC333. Two different compositions for the TSB electrodes were tested: 10 wt% and 4wt % T2-20. When the TSB was used at 10 wt.%, the initial capacity of the cell was relatively low, followed by continuous capacity degradation for 50 cycles. When the TSB was used at 4 wt.%, the charge-discharge profiles of the TSB-based cell were almost identical to those of the reference cells. However, a slight initial voltage drop in the discharge profile of the TSB-based cell led to a slightly lower capacity compared to that of the reference cell with conventional PVDF (Fig. 5.3.a). The voltage drop indicated that the TSB might not be as stable as PVDF, at high voltage with *P*-NMC333 as the active material. The cycling performance of the TSB-based cell was slightly unstable in the first 15 cycles. Nevertheless, the capacity retention of the 4 wt% T2-20 based cell was about the same as that of the reference cell. As observed for *P*-LNMO, the reduction of TSB from 10wt% to 4wt% helped stabilize the cycling performance of the electrode (Fig. 5.3b).

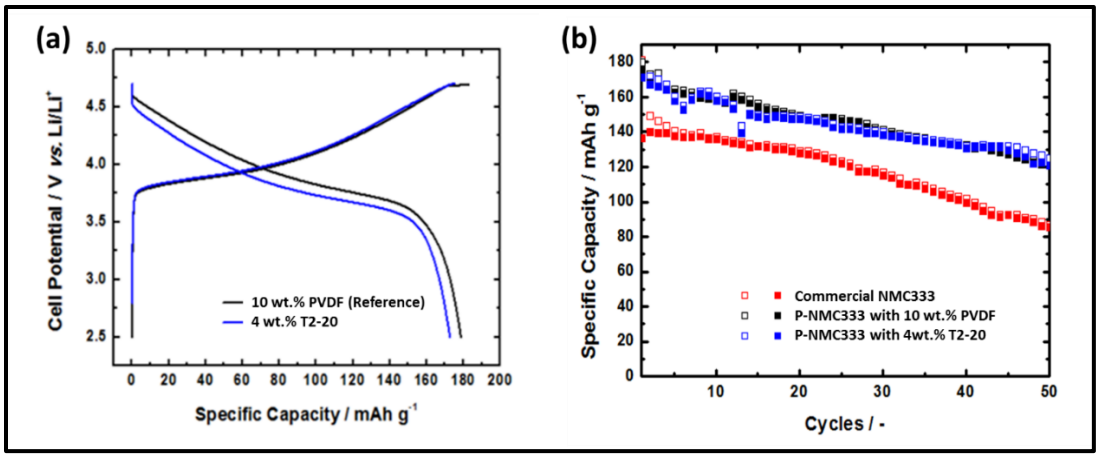

Figure 5.3. (a) First cycle voltage profiles and (b) cycling performance of the *P*-NMC333 cathode coin cells based on different binders. (Figure courtesy of Ms. Hyesung Chung)

5.3. Nail Penetration Test

Prior to nail penetration testing, the coin cells were pre-conditioned, following a procedure similar to that established for NMC cells (Chapter 2), except that the voltage windows were extended for the respective material (Table 5.1). For instance, the LRLO cells were first charged to 4.85 and discharged to 2.0 V for 1 cycle at C/10 rate, and then cycled between 4.85-2.0 V at C/2 rate, followed by charging to 4.85 V at C/10 rate. The final charge capacity was typically ~ 1.0 mAh/cell. The charged cells were heated to 110 ^{o}C on a hot plate for 1 minute, air-cooled, and rested for 10 minutes, after which the voltage stabilized at ~ 4.65 V. Nail penetration tests were carried out on fully charged cells using the same testing setup as described in Chapter 2.

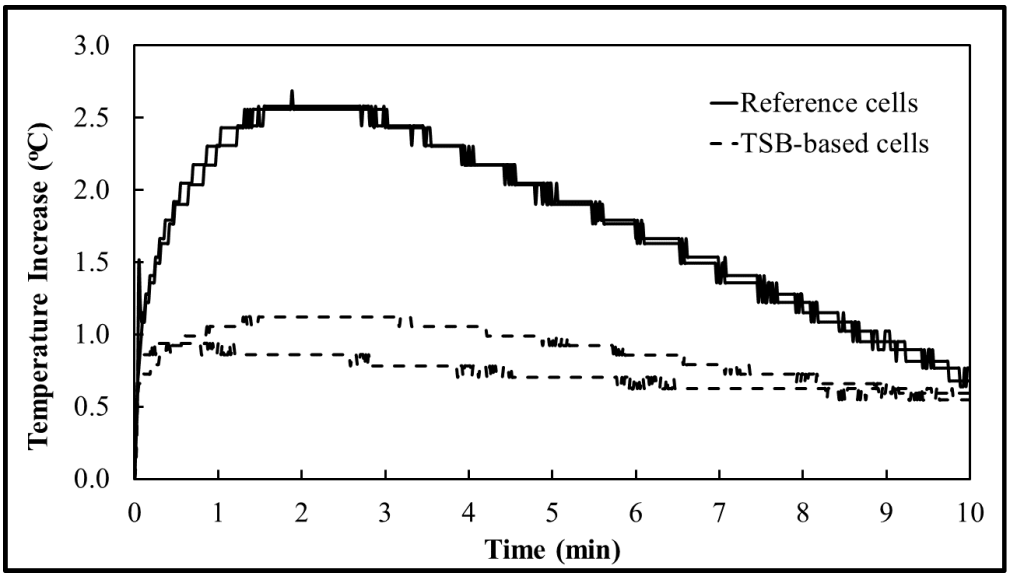

Figure 5.4. Typical temperature increase profiles of LRLO cathode half-cellsin nail penetration test. (LRLO was provided by LESC)

Figure 5.4 shows the typical temperature increase profiles in nail penetration for reference and modified cells with LRLO active material. The reference cells showed consistent temperature increase profiles, both reaching the peak temperature increase around 4 ^{o}C after ~2 minutes, and then dropped back to room temperature within the next 12 minutes. Because the conventional PVDF binder of the reference electrode did not melt upon preheating, the structural integrity of the electrode remained intact and thus, the charge flows across the cathode as well as between cathode and current collector were not hindered. This allowed a large discharge current from anode to cathode, resulting into a higher Joule heating rate and a higher peak temperature increase. As the stored energy was quickly dissipated via Joule heating, heat generation eventually stopped and the temperature began to descend. The TSB-based cells showed different temperature profiles, with the peak values of only 1.4to 1.7 ^{o}C. The peak temperature was reached at different times, but both within the first 2 minutes. The cooling tails of temperature profiles of the

modified cells were more gradual compared to that of the reference cell, as Joule heat was continuously generated at a slower rate, even after 20 minutes.

ACKNOWLEDGEMENT

This research is supported by the Advanced Research Projects Agency – Energy (ARPA-E) under Grant No. DE-AR0000396, for which we are grateful to Dr. Ping Liu, Dr. John Lemmon, Dr. GrigoriiSoloveichik, Dr. Chris Atkinson, and Dr. Dawson Cagle. Special thanks are also due to Dr. Jiang Fan and Dr. Dengguo Wu for the help with lithium-ion battery design and processing.

Chapter 5, in parts, is currently being prepared for submission for publication of the material: Le, Anh V.; Chung, Hyeseung; Wang, Meng; Noelle, Daniel J.; Shi, Yang; Yoon, Hyojung; Meng, Ying S.; Qiao, Yu. “Effects of Electrode Composition on Lithium-ion Battery Based on Thermally Sensitive Binder.” The dissertation author was the primary investigator and author of this material.

CHAPTER 6 – SUMMARY AND FUTURE WORKS

6.1. SUMMARY OF OUR FINDINGS

6.1.1. CRACKING/DEBONDING INITIATION (CDI) ADDITIVES

Using stress concentrating additives is a thermal-runaway mitigation (TRM) method based on mechanically-triggered cracking/debonding initiation (CDI) mechanisms. The CDI materials of interests are carbon and silica, for their inertness within the lithium-ion battery (LIB) environment. We investigated several carbon-based and silica-based materials with varied particle sizes, shapes, surface areas and hydrophilicity (Table 1.1). Blunt impact tests on electrode stacks were conducted to select the best performing CDI systems. The testing results showed that upon impact, a couple of CDI candidates, namely CGR and KBG, could efficiently promote cracking/debonding of active materials layers in electrodes.

We then tested the CDI-modified electrodes in coin cell. Cycle life test showed that the content of CDI additives must not exceed 1 wt.% of the combined masses of other electrode components, i.e. active material (AM), binder (B), and carbon black (CB). This limitation ensured the homogeneity of the electrode, which was necessary for a satisfactory electrochemical performance. However, it also rendered the CDI mechanism less effective, showing no reduction in peak temperature increase compared to reference cell in both nail penetration (Figure 3.7) and blunt impact tests (Figure 3.9).

In conclusion, highly porous carbon-based additives are effective CDI candidates. However, incorporating them into LIB electrodes is a challenging task, due to the altered microstructure of active material layer. Limiting the content of CDI additives to less than 1 wt% can help avoid the detrimental effects on cycling performance, but also renders the CDI mechanism ineffective for TRM.

6.1.2. THERMALLY SENSITIVE BINDERS (TSB)

Thermally sensitive binder (TSB) was another TRM method based on CDI mechanisms. The investigation on TSB was performed mainly for positive electrodes, i.e. cathodes. Because the electrical conductivity of cathode active material was lower than that of graphite in anode, it could be more sensitive to the TSB. In addition, the CMC/SBR had been commonly used as anode binder in most industrial processes for economic and environmental purposes, so that changing anode binder may require extensive modifications of production procedure of LIB cells.

The TSB candidates were selected from the group of poly(vinylidene fluoride – co – hexafluoropropylene) (PVDF-HFP), with various molecular weights (Table 1.2). First, we performed nail penetration tests on cathode half-cells to select the baseline material for the TSB system. Its TRM mechanism must be triggered at ~110 ^{o}C. The testing results suggested that only when the HFP content was sufficiently high, e.g. ~ 32wt%, could the binder be effective for heat mitigation in a shorted battery cell. The high HFP-content polymer was referred to as B03, a highly amorphous PVDF-HFP copolymer which could absorb a large amount of electrolyte, making the electrode more ionically conductive.

However, B03 was prone to swelling after several charge-discharge cycles, resulting into poor long-term cycling performance of the LIB cell.

To improve the cycling performance, we tested a series of modification methods on B03: refining molecular weight, crosslinking, polymer blending, and thermal treatment (Table 4.1). Among these methods, the thermally treated B02/B03 blends at 1:4 w/w ratio exhibited satisfactory performance in both nail penetration and cycle life experiments. The top TSB candidate was labelled as T2-20.

Further optimization was performed on T2-20 based LIB cells by adjusting the contents of the T2-20 binder and carbon black (CB). Cycle life testing and nail penetration testing were performed and their results suggested that there were two effective routes to reduce the peak temperature increase of a nail penetrated LIB cell: (i) increasing the content of the T2-20 binder, while keeping the content of the CB constant at ~3 wt.%.; (ii) reducing the contents of both TSB and CB, while keeping the mass ratio between them constant at B:CB = 4:3. Cycle life measurement at 60 ^{o}C revealed that the AM:binder:CB mass ratio must be 93:2:1.5 to maintain the satisfactory performance (Figure 4.7), indicating that a constant B:CB ratio of 4:3 was necessary to ensure the high electrical conductivity of positive electrode. Long-term cycling at ambient temperature confirmed this conclusion (Figure 4.8). The T2-20 based electrode with the AM:binder:CB mass ratio of 93:2:1.5 can be referred to as the “optimized TSB” (o-TSB) based electrode.

The SEM images of B01 (reference), B03 (baseline), and T2-20 based cathodes at different stages of nail penetration tests showed well packed electrode microstructures after

pre-cycling and charging. Upon preheating of the charged cell, pronounced swelling was observed for both B03 and T2-20 binders, while B01 remained intact. However, the swollen regions of T2-20 were larger in size and scattered across the electrode, while those of the B03 were relatively small and were distributed uniformly across the electrode. As a result, the B03-based electrode became more vulnerable to nail loading and showed pronounced cracking; T2-20 based electrode remained structurally integral without evident cracks after the test. Therefore, the heat mitigation effect of T2-20 was somewhat less than that of B03, and should be attributed to the swollen binder–CB regions with reduced electrical conductivity.

Differential Scanning Calorimetry (DSC) results of bulk polymers showed that blending and thermally treating the high HFP-content copolymer B03 and the highly crystalline, linear PVDF homopolymer B02 increased the crystallinity of the B02 phase by more than 50 % in both dry and electrolyte soaked states (Table 4.3). On the one hand, even though the crystallinity of the B03 phase remained unaffected, the increased crystallinity of B02 considerably suppressed the swelling of B03, and thus improved the structural integrity of the composite electrode over charge-discharge cycles. On the other hand, the unchanged amorphous B03 component helped preserve the high thermal sensitivity of the binder, critical to the TRM performance. The swelling index (SI) measurement also confirmed the effect of polymer blending and thermal treatment on the B03-based system (Table 4.4). Note that these mechanism studies were focused on bulk polymer samples. Therefore, the results were only valid for comparing among different

types of polymer binders, and may be different from their actual behaviors in electrodes, especially when subjected to electrochemical reactions within LIB cell.

To investigate the influence of the binder types subjected to external loading, we measured the internal resistances of half-cells before and after impact (Table 4.5). The reference and o-TSB based cells showed similar values of internal resistance before preheating, indicating similar states of health. After preheating, the resistances of both reference and o-TSB based cells increased, but the latter was milder. After being impacted, the internal resistance of the o-TSB based cell increased to twice as much as the value of the reference cell. This result suggests that the binder melts/swells upon preheating, weakening and altering the microstructure of the TSB-based electrode, so that it becomes more vulnerable to external loading.

6.1.3. Compatibility with High-Energy Battery Chemistry

High-voltage cathode materials were synthesized at the Laboratory for Energy Storage and Conversion (LESC) led by Professor Ying Shirley Meng of the University of California – San Diego. The high-energy cathode materials included polyol-synthesized lithium nickel manganese oxide (P-LMNO), polyol-synthesized lithium nickel manganese cobalt oxide (P-NMC333), and lithium-rich layered oxide (LRLO). The reference binder material was conventional PVDF. T2-20 was chosen for compatibility study.Overall, the testing results showed that T2-20, when used at reduced content, i.e. about 50% of the regular amount, was compatible with the high-energy materials. The thermal sensitivity was also preserved for TRM.

6.2. Future Work

6.2.1. Revisiting Silica-based CDI

The highly porous and hydrophilic carbon-based CDI additives, CBR and KBG, were shown to be ineffective for heat reduction in mechanical abuse tests. However, the major reason could be the high electrical conductivity of the base material, which facilitated the initial heating rate due to charge transfer across the electrodes. The silica-based CDI additives were shown to be either non-compatible with the battery environment or ineffective for cracking/debondingmechanism in preliminary blunt impact test on free electrode stack. However, no coin cell testing has been performed on silica-based CDI. Silica is non-electrically conductive, so it may not have the problem regarding high initial heat generation in short circuit. However, the electrical nonconductivity may impose unfavorable effect onto the performance of the batter in normal condition. Therefore, it is of our high interest to revisit and further investigate the silica-based CDI system.

6.2.2. Pouch Cell Testing

In the current study, the size of battery cells was small, with the capacity of about 5 mAh/cell and the energy of 20-25 mWh/cell. In the actual energy storage system (ESS) of an electric vehicle (EV), the battery cells store a much larger amount of energy, much higher than 11 Wh/cell (Lambert, 2016). Therefore, it is critical to investigate the compatibility and functionality of TSB in higher-capacity pouch cells. Regardless of the cell geometry, the stacking configuration should be the same. That is, multiple layers of cathode-separator-anode form a flat prismatic. In chapter 4, we tested large pouch cells

contained 10 layers of electrodes welded together, with the layer size of 76.2×76.2 mm. The first charge capacity was around 2 Ah/cell. Similar cell assembly may be employed for the future large cell testing. Cycle life, vibration, nail penetration, and crush tests should be performed, and the testing conditions should conform with the well-recognized standards in the LIB and the EV industry, e.g. IEC, ISO, SAE, and UL (Lawson, 2005).

6.2.3. Compatibility of TSB with Other Battery Safety Mechanisms

It is of high interest to investigate the compatibility of TSB with other internal safety mechanisms, such as modified current collector (Qiao, et al., 2016; Wang, et al., 2016) and thermal-runaway retardant (TRR) additives (Shi, et al., 2016). In this study, we have showed that TSB effectively reduced the Joule heating rate during the initial stage of short circuit, thus limiting the peak temperature increase. However, due to the high energy density of large LIB systems, the dynamic nature of battery failures, as well as the requirement of short response time (Balakrishnan, et al., 2006), there is a need to combine multiple TRM mechanisms in a single LIB cell.

The work may begin with understanding the compatibility of TSB with each of other safety systems individually. The combined systems can be first tested at low capacity level, i.e. in coin cells with regular NMC active materials. The next step can be integrating more than two systems into the battery. Once the compatibility among different safety systems is confirmed, large-scale systems, i.e. pouch cells, should be tested. At the same time, it is also beneficial to study the compatibility to the near-future high energy active materials.

REFERENCES

3M, 2003. *Dyneon Fluoroplastics - Product Comparison Guide.* [Online]
Available at:
http://solutions.3m.com/3MContentRetrievalAPI/BlobServlet?lmd=1200919558000&locale=cs_CZ&univid=1180594859500&fallback=false&assetType=MMM_Image&blobAttribute=ImageFile
[Accessed 15 11 2016].

3M, 2016. *Product Catalogue: THV Polymer - 3M.* [Online]
Available at:
http://solutions.3m.com/wps/portal/3M/en_WW/3M_Dyneon/Home/Products/one/?PC_Z7_RJH9U5230GL610IK6R52382044000000_nid=H8D54D09WMbeSMR0VJH59Pgl
[Accessed 9 11 2016].

Abdel-Rahman, A. A., 1998. On the Emission from Internal Combustion Engines: A Review.. *International Journal of Energy Research,* 22(6), pp. 483-513.

Alves, N., Plepis, A., Giacometti, J. & Oliveira Jr., O., 1998. Influence of preparation methods and thermal treatment in melt-solidified and cast films of poly (vinylidene fluoride-trifluorethylene) copolymers. *Ferroelectrics Letters Section,* 23(5-6), pp. 99-105.

Ameduri, B., 2009. From Vinylidene Fluoride (VDF) to the Application of VDF-Containing Polymers and Copolymers: Recent Development and Future Trends. *Chem. Rev.,* Volume 109, pp. 6632-6686.

An, S.J., Li, J., Daniel, C., Mohanty, D., Nagpure, S. and Wood, D.L., 2016. The state of understanding of the lithium-ion-battery graphite solid electrolyte interphase (SEI) and its relationship to formation cycling. *Carbon,* Volume 105, pp. 52-76.

Arencón, D. & Velasco, J., 2009. Fracture toughness of polypropylene-based particulate composites. *Materials,* 2(4), pp. 2046-2094.

Arkema, 2016. *Kynar/KynarFlex - Polyvinylidene Fluoride (PVDF) Resins for Batteries.* [Online]
Available at: http://americas.kynar.com/export/sites/kynar-americas/.content/medias/downloads/literature/2016-kynar-battery-brochure.pdf[Accessed 9 11 2016].

Aurbach, D., Zinigrad, E., Cohen, Y. & Teller, H., 2002. A short review of failure mechanisms of lithium metal and lithiated graphite anodes in liquid electrolyte solutions. *Solid State Ionics,* Volume 148, p. 405–416.

Automotive Energy Supply Corporation (AESC) , 2013. *Mechanism Behind Rechargeable Lithium-ion Batteries.* [Online]
Available at: http://www.eco-aesc-lb.com/en/about_liion/
[Accessed 10 11 2016].

Baginska, M., Blaiszik, B.J., Merriman, R.J., Sottos, N.R., Moore, J.S. and White, S.R., 2012. Autonomic Shutdown of Lithium-Ion Batteries Using Thermoresponsive Microspheres. *Advanced Energy Materials*, 2(5), pp. 583-590.

Balakrishnan, . P. G., Ramesh, R. & Prem Kumar., T., 2006. Safety mechanisms in lithium-ion batteries. *Journal of Power Sources*, 155(2), pp. 401-414.

Barsoum, M., Kangutkar, P. & Wang, A., 1992. Matrix crack initiation in ceramic matrix composites Part I: Experiments and test results. *Composites science and technology*, 44(3), pp. 257-269.

Binotto, G., Genies, S. & Morcrette, M., 2011. *Review Thermal Runaway Reactions Mechanisms.* [Online]
Available at: http://www.transport-research.info/sites/default/files/project/documents/20130118_155818_74779_HELIOS_D6.1_PublicVersion%5BJan2011%5D.pdf
[Accessed 10 11 2016].

Blaine, R. L. & Waguespack, L. E., TA276. *Determination of Polymer Crystal Molecular Weight.* [Online]
Available at: http://www.tainstruments.com/pdf/literature/TA276.pdf
[Accessed 9 11 2016].

Brand, M., Gläser, S., Geder, J., Menacher, S., Obpacher, S., Jossen, A. and Quinger, D., 2013. Electrical safety of commercial Li-ion cells based on NMC and NCA technology compared to LFP technology. *Electric Vehicle Symposium and Exhibition (EVS27), IEEE.*, Volume 2013 World, pp. 1-9.

Brice, C. W., Dougal, R. A. & Hudgins, J. L., 1996. Review of technologies for current-limiting low-voltage circuit breakers. *IEEE Transactions on Industry Applications*, 32(5), pp. 1005-1010.

Broberg, K., 1968. Critical review of some theories in fracture mechanics. *International Journal of Fracture Mechanics*, 4(1), pp. 11-19.

Chalk, S. G. & Miller, J. F., 2006. Key challenges and recent progress in batteries, fuel cells, and hydrogen storage for clean energy systems. *Journal of Power Sources*, 159(1), pp. 73-80.

Chan, C. C., 2007. The state of the art of electric, hybrid, and fuel cell vehicles.. *Proceedings of the IEEE,* 95(4), pp. 704-718.

Andrews, S.C., Liu, J., Cui, Y. and Bao, Z., 2016. Fast and reversible thermoresponsive polymer switching materials for safer batteries. *Nature Energy*, Volume 1, p. 15009.

Choi, N.S., Chen, Z., Freunberger, S.A., Ji, X., Sun, Y.K., Amine, K., Yushin, G., Nazar, L.F., Cho, J. and Bruce, P.G., 2012. Challenges Facing Lithium Batteries and Electrical Double-Layer Capacitors. *Angewandte Chemie International Edition*, 51(40), pp. 9994-10024.

CN102924732B, 2013. *Method for preparing polyvinylidene fluoride (PVDF)-hexafluoropropylene (HFP) modification membrane of high energy density through hot pressing cross linking.* China, Patent No. CN102924732B.

da Silva, C. & Faria, J., 2003. Photochemical and photocatalytic degradation of an azo dye in aqueous solution by UV irradiation. *Journal of Photochemistry and Photobiology A: Chemistry*, 155(1), pp. 133-143.

Doh, C.H., Kim, D.H., Kim, H.S., Shin, H.M., Jeong, Y.D., Moon, S.I., Jin, B.S., Eom, S.W., Kim, H.S., Kim, K.W. and Oh, D.H., 2008. Thermal and electrochemical behaviour of C/Li x CoO 2 cell during safety test. *Journal of Power Sources*, 175(2), pp. 881-88.

Doughty, D. H. & Roth, E., 2012. Doughty, D.H. and Roth, E.P., 2012. A general discussion of Li ion battery safety. *The Electrochemical Society Interface*, 21(2), pp. 37-44.

Electropaedia, 2005. *Electropaedia - Battery and Energy Technologies.* [Online]
Available at: http://www.mpoweruk.com/standards.htm#automotive
[Accessed 7 12 2016].

EnerDel Corporation, 2005. *EnerDel Technical Presentation (PDF). EnerDel Corporation.*. [Online]
Available at:
http://web.archive.org/web/20080414071700/http://enerdel.com/pdfs/EnerDelTechnicalPresentation.pdf
[Accessed 10 11 2016].

Etacheri, V., Marom, R., Elazari, R., Salitra, G. and Aurbach, D., 2011. Challenges in the development of advanced Li-ion batteries: a review. *Energy & Environmental Science*, 4(9), pp. 3243-3262.

Frackowiak, E. & Beguin, F., 2001. Carbon materials for the electrochemical storage of energy in capacitors. *Carbon,* 39(6), pp. 937-950.

Golubkov, A.W., Fuchs, D., Wagner, J., Wiltsche, H., Stangl, C., Fauler, G., Voitic, G., Thaler, A. and Hacker, V., 2014. Thermal-runaway experiments on consumer Li-ion batteries with metal-oxide and olivin-type cathodes. *RSC Advances,* 4(7), pp. 3633-3642.

Goriparti, S., Miele, E., De Angelis, F., Di Fabrizio, E., Zaccaria, R.P. and Capiglia, C., 2014. Review on recent progress of nanostructured anode materials for Li-ion batteries. *Journal of Power Sources, ,* Volume 257, pp. 421-443.

Gozdz, A. S., Schmutz, C. N. & Tarascon, J.-M., 1994. *Rechargeable lithium intercalation battery with hybrid polymeric electrolyte.* US, Patent No. US 5296318 A.

Gray, A. P., 1970. Polymer crystallinity determinations by DSC. *Thermochimica Acta,* 1(6), pp. 563-579.

Green Car Congress, 2005. *A123Systems Launches New Higher-Power, Faster Recharging Li-Ion Battery Systems.* [Online]
Available at: http://www.greencarcongress.com/2005/11/a123systems_lau.html
[Accessed 10 11 2016].

Hammami, A., Raymond, N. & Armand, M., 2003. Lithium-ion batteries: Runaway risk of forming toxic compounds. *Nature,* 424(6949), pp. 635-636.

He, L., Xu, Q., Hua, C. & Song, R., 2010. Effect of multi-walled carbon nanotubes on crystallization, thermal, and mechanical properties of poly (vinylidene fluoride). *Polymer Composites,* 31(5), pp. 921-927.

Hilding, J., Grulke, E. A., Zhang, Z. G. & Lockwood, F., 2003. Dispersion of Carbon Nanotubes in Liquids. *Journal of Dispersion Science and Technology,* 24(12), pp. 1-41.

Hou, P., Wang, X., Song, D., Shi, X., Zhang, L., Guo, J. and Zhang, J., 2014. Design, synthesis, and performances of double-shelled LiNi 0.5 Co 0.2 Mn 0.3 O 2 as cathode for long-life and safe Li-ion battery. *Journal of Power Sources,* Volume 265, pp. 174-181.

J Carpenter Environmental, LLC., 2013. *Cabot Norit Activated Carbon – DARCO ® FGD.* [Online]
Available at: http://www.jcarpenterenvironmental.com/pdf/Cabot_Darco_FGD.pdf
[Accessed 9 11 2016].

Katsurao, T., Horie, K., Nagai, A. & Ichikawa, Y., 2002. *Vinylidene fluoride copolymer for gel-form solid electrolyte formation, solid electrolyte, and battery.* U.S., Patent No. US6372388 B1.

Keyser, M. & Kim, G.-H., 2011. *Numerical and Experimental Investigation of Internal Short Circuits in a Li-ion Cell.* [Online]
Available at: http://www.nrel.gov/transportation/energystorage/pdfs/50917.pdf
[Accessed 10 11 2016].

Khaligh, A. & Li, Z., 2010. Battery, ultracapacitor, fuel cell, and hybrid energy storage systems for electric, hybrid electric, fuel cell, and plug-in hybrid electric vehicles: State of the art.. *IEEE transactions on Vehicular Technology*, 59(6), pp. 2806-2814.

Kim, G.-H., Pesaran, A. & Spotnitz, R., 2007. A three-dimensional thermal abuse model for lithium-ion cells. *Journal of Power Sources*, 170(2), pp. 476-489.

Kim, G.-H., Smith, K. & Pesaran, A., 2009. *Lithium-Ion Battery Safety Study Using Multi-Physics Internal Short-Circuit Model.* [Online]
Available at: http://www.nrel.gov/transportation/energystorage/pdfs/45856.pdf
[Accessed 9 12 2017].

Kim, T., Lu, W., Lim, H., Han, A. and Qiao, Y., 2011. Electrically controlled hydrophobicity in a surface modified nanoporous carbon. *Applied Physics Letters*, 98(5), p. 053106.

Lambert, F., 2016. *Tear down of 85 kWh Tesla battery pack shows it could actually only be a 81 kWh pack [Updated]*. [Online]
Available at: https://electrek.co/2016/02/03/tesla-battery-tear-down-85-kwh/
[Accessed 7 12 2016].

Larcher, D. & Tarascon, J. M., 2015. Towards greener and more sustainable batteries for electrical energy storage.. *Nature Chemistry*, 7(1), pp. 19-29.

Lawson, B., 2005. *Electropaedia - Battery and Energy Technologies.* [Online]
Available at: http://www.mpoweruk.com/lithium_failures.htm
[Accessed 9 11 2016].

Le, A. V., Wang, M., Shi, Y., Noelle, D., Qiao, Y. and Lu, W., 2015, a. Effects of additional multiwall carbon nanotubes on impact behaviors of LiNi0.5Mn0.3Co0.2O2 battery electrodes. *Journal of Applied Physics*, 118(8), p. 085312.

Le, A. V., Le, A.V., Wang, M., Shi, Y., Noelle, D.J. and Qiao, Y. 2015, b. Heat generation of mechanically abused lithium-ion batteries modified by carbon black micro-particulates.. *Journal of Physics D: Applied Physics*, 48(38), p. 385501.

Le, A. V., Wang, M., Shi, Y., Noelle, D.J., Yoon H., Meng, Y.S., Wu, D., Fan, J. and Qiao, Y., To be published, a. Heat generation of mechanically abused lithium-ion battery cell based on thermally sensitive cathode binder.

Le, A. V., Wang, M., Noelle, D.J., Shi, Y., Yoon H., Zhang, M., Meng, Y.S. and Qiao, Y., To be published, b. Effects of Macromolecular Configuration of Thermally Sensitive Binder in Lithium Ion Battery.

Le, A. V., Wang, M., Noelle, D.J., Shi, Y., Meng, Y.S. and Qiao, Y., To be published, c. Mitigating Thermal Runaway of Lithium-ion Battery by Using Thermally Sensitive Binder.

Le, A. V.,Chung, H., Wang, M., Noelle, D.J., Shi, Y., Yoon H., Meng, Y.S. and Qiao, Y., To be published, d. Effects of Electrode Composition on Lithium-ion Battery Based on Thermally Sensitive Binder.

Lin, C.C.,Wu, H.C., Pan, J.P., Su, C.Y., Wang, T.H., Sheu, H.S. and Wu, N.L., 2013. Investigation on suppressed thermal runaway of Li-ion battery by hyper-branched polymer coated on cathode. *Electrochimica Acta*, Volume 101, pp. 11-17.

Lisbona, D. & Snee, T., 2011. A review of hazards associated with primary lithium and lithium-ion batteries. *Process Safety and Environmental Protection*, 89(6), pp. 434-442.

Luntz, A., 2015. Beyond Lithium Ion Batteries. *The journal of physical chemistry letters*, 6(2), pp. 300-301.

Marks, T., Trussler, S., Smith, A.J., Xiong, D. and Dahn, J.R., 2011. A guide to Li-ion coin-cell electrode making for academic researchers. *Journal of The Electrochemical Society*, 158(1), pp. A51-A57.

Martinez, A.B., Gamez-Perez, J., Sanchez-Soto, M., Velasco, J.I., Santana, O.O. and Maspoch, M.L., 2009. The essential work of fracture (EWF) method–analyzing the post-yielding fracture mechanics of polymers. *Engineering failure analysis*, 16(8), pp. 2604-2617.

Matouš, K., 2003. Damage evolution in particulate composite materials. *International journal of solids and structures*, 40(6), pp. 1489-1503.

Ma, W., Yuan, H. & Wang, X., 2014. The Effect of Chain Structures on the Crystallization Behavior and Membrane Formation of Poly (Vinylidene Fluoride) Copolymers. *Membranes*, 4(2), pp. 243-256.

Ma, W., Zhang, J. & Wang, X., 2007. Effect of Initial Polymer Concentration on the Crystallization of Poly (Vinylidene Fluoride)/Poly (Methyl Methacrylate) Blend from Solution Casting. *Journal of Macromolecular Science, Part B - Physics*, 47(1), pp. 139-149.

Mikolajczak, C., Kahn, M., White, K. & Long, R., 2012. *Lithium-ion batteries hazard and use assessment.*. s.l.:Springer Science & Business Media.

Miyazaki, T., Takeda, Y., Akasaka, M., Sakai, M. and Hoshiko, A., 2008. Preparation of isothermally crystallized γ-form poly (vinylidene fluoride) films by adding a KBr powder as a nucleating agent. *Macromolecules*, 41(7), pp. 2749-2753.

MTI Corp., 2013, a. *R&D Scale Cylinder/Coin/Pouch Cell Flow-Chart with MTI's Battery Equipment.* [Online]
Available at:
http://www.mtixtl.com/xtlflyers/Flow%20Chart%20of%20Pouch,%20Cylinder%20and%20Coin%20Cell%20by%20MTI's%20Battery%20Equipment.pdf
[Accessed 16 11 2016].

MTI Corp., 2013, b. *Artificial Graphite Powder for Li-ion Battery Anode, EQ-Lib-CMSG.* [Online]
Available at: http://www.mtixtl.com/ArtificialGraphitePowderforLi-ionbatteryAnode150g/bag-EQ-Lib-CMSG.aspx[Accessed 9 11 2016].

MTI Corp., 2013, c. *LiNiCoMnO2 (NCM) Powder for High Power Li-ion Battery Cathode EQ-Lib-LNCM523.* [Online]
Available at: http://www.mtixtl.com/LiNiCoMnO2powderforLi-ionpowerbatterycathode200g/bottleNiCoMn.aspx[Accessed 9 11 2016].

MTI Corp., 2013, d. *A Step by Step Recipe for Preparing Water-based Electrode Slurry (Graphite Anode).* [Online]
Available at:
http://www.mtixtl.com/documents/Step%20by%20Step%20Recipe%20for%20Preparing%20Anode%20%20Cathode%20Electrode%20Slurry.pdf
[Accessed 9 12 2016].

Nakagawa, K. & Ishida, Y., 1973. Annealing effects in poly (vinylidene fluoride) as revealed by specific volume measurements, differential scanning calorimetry, and electron microscopy. *Journal of Polymer Science: Polymer Physics Edition*, 11(11), pp. 2153-2171.

Nakagawa, K. & Ishida, Y., 1973. Annealing effects in poly (vinylidene fluoride) as revealed by specific volume measurements, differential scanning calorimetry, and electron microscopy.". *Journal of Polymer Science: Polymer Physics*, 11(11), pp. 2153-2171.

Neese, B., 2009. Investigations of structure-property relationships to enhance the multifunctional properties of PVDF-based polymers. *Doctoral dissertation, The Pennsylvania State University.*

Nielsen , L. E., 1969. Cross-Linking–Effect on Physical Properties of Polymers. *Journal of Macromolecular Science, Part C - Polymer Reviews*, 3(1).

Nunes, R. W., Martin, J. R. & Johnson, J. F., 1982. Influence of molecular weight and molecular weight distribution on mechanical properties of polymers." Polymer Engineering & Science 22, no. 4 (1982): 205-228.. *Polymer Engineering & Science*, 22(4), pp. 205-228.

Orendorff, , C. J., Roth, E. P. & Nagasubramanian, G., 2011. Experimental triggers for internal short circuits in lithium-ion cells. *Journal of Power Sources*, 196(15), pp. 6554-6558.

Orendorff, C., Lamb, J., Steele, L.A.M., Spangler, S.W. and Langendorf, J.L., 2016. *Quantification of Lithium-ion Cell Thermal Runaway Energetics.* [Online]
Available at: http://prod.sandia.gov/techlib/access-control.cgi/2016/160486.pdf
[Accessed 10 11 2016].

Pacific Rim Oenology Services, 2007. *Norit Activated Carbon – DARCO ® KB-G.* [Online]
Available at: http://www.pros.co.nz/PDF/PDS/Carbon%20KB-G%20Tech%20Sheet%2007-07.pdf
[Accessed 9 11 2016].

Panasonic, 2011. *Overview of lithium ion batteries (PDF).* [Online]
Available at: https://industrial.panasonic.com/cdbs/www-data/pdf/ACA4000/ACA4000PE3.pdf
[Accessed 10 11 2016].

Park, J., Endo, T., Nam, J.H., Park, J.H. and Fukuchi, I., Samsung Sdi Co., Ltd., 2014. *Binder composition, separator including binder formed from the binder composition,*

lithium battery including the separator, and method of preparing the binder composition. US, Patent No. US 20150155539 A1.

Park, K., 2010. Spectroscopy characteristics for interlamellar silylation of H+-titanosilicate using dodecylamine and octyltriethoxysilane. *Microporous and mesoporous materials,*, 127(1), pp. 142-146.

Park, M., Zhang, X., Chung, M., Less, G.B. and Sastry, A.M., 2010. A review of conduction phenomena in Li-ion batteries. *Journal of Power Sources,* 195(24), pp. 7904-7929.

Pesaran, A. A., 2001. Battery thermal management in EV and HEVs: issues and solutions. *Battery Man,* 43(5), pp. 34-49.

PiezoTech, 1993. *P(VDF-TrFE) Ferrolelectric & Piezoelectric copolymers.* [Online]
Available at: http://www.piezotech.fr/fr/2-products-piezoelectric-polymers/news/news-32-p-vdf-trfe-ferrolelectric-&-piezoelectric-copolymers.html
[Accessed 10 11 2016].

Quantum Advanced Engineering Plastics, 2009. *KYNAR® & KYNAR FLEX® PVDF - Performance Characteristics & Data.* [Online]
Available at: http://www.quantum-polymers.com/pdf/KynarBrochure.pdf
[Accessed 10 11 2016].

Raghavan, P., Zhao, X., Choi, H., Lim, D.H., Kim, J.K., Matic, A., Jacobsson, P., Nah, C. and Ahn, J.H., 2014. Electrochemical characterization of poly (vinylidene fluoride-co-hexafluoro propylene) based electrospun gel polymer electrolytes incorporating room temperature ionic liquids as green electrolytes for lithium batteries. *Solid State Ionics,* Volume 262, pp. 77-82.

Roth, E. & Orendorff, C., 2012. How electrolytes influence battery safety. *The Electrochemical Society Interface,* 21(2), pp. 45-49.

Roth, E. & Orendorff, C., 2012. How electrolytes influence battery safety. *The Electrochemical Society Interface,* 21(2), pp. 45-49.

Sahagian, K. & Bair, H., 2012. *Transition Temperature Microscopy:*. [Online]
Available at: http://www.anasysinstruments.com/an14.pdf
[Accessed 20 12 2016].

Sahu, S. & Broutman, L. J., 1972. Mechanical properties of particulate composites. *Polymer Engineering & Science,* 12(2), pp. 91-100.

Santhanagopalan, S., Ramadass, P. & Zhang, J., 2009. Analysis of internal short-circuit in a lithium ion cell. *Journal of Power Sources,* 194(1), pp. 550-557.

Schweiger, H.G., Obeidi, O., Komesker, O., Raschke, A., Schiemann, M., Zehner, C., Gehnen, M., Keller, M. and Birke, P., 2010. Comparison of several methods for determining the internal resistance of lithium ion cells. *Sensors,* 10(6), pp. 5604-5625.

Scrosati, B. & Garche, J., 2010. Lithium Batteries: Status, Prospect and Future. *Journal ò Power Sources,* 195(9), pp. 2419-2430.

Shi, Y., Noelle, D.J., Wang, M., Le, A.V., Yoon, H., Zhang, M., Meng, Y.S. and Qiao, Y., 2016. Role of Amines in Thermal-Runaway-Mitigating Lithium-Ion Battery. *ACS Applied Materials & Interfaces 8(45).*

Singh, M., Kaiser, J. & Hahn, H., 2015. Thick electrodes for high energy lithium ion batteries. *Journal of The Electrochemical Society,* 162(7), pp. A1196-A1201.

Sivakumar, P., Gunasekaran, M., Sasikumar, M. & Jagadeesan, A., 2013. PVDF-HFP Based Porus Polymer Electrolyte For Lithium Battery Applications. *International Journal of Science and Research (IJSR),* pp. 22-25.

Song, M.K., Kim, Y.T., Kim, Y.T., Cho, B.W., Popov, B.N. and Rhee, H.W., 2003. Thermally stable gel polymer electrolytes. *Journal of the Electrochemical Society,* 150(4), pp. A439-A444.

St. John, A., 2016. *Why Lithium-Ion Batteries Still Explode, and What's Being Done to Fix the Problem,* s.l.: Consumer Reports.

Stephan, A. M., 2006. Review on gel polymer electrolytes for lithium batteries. *European Polymer Journal,* 42(1), pp. 21-42.

Taguet, A., Ameduri, B. & Boutevin, B., 2005. Crosslinking of vinylidene fluoride-containing fluoropolymers. In: *Crosslinking in Materials Science.* s.l.:Springer Berlin Heidelberg, pp. 127-211.

Takahashi, M., Ohtsuka, H., Akuto, K. & Sakurai, Y., 2005. Confirmation of long-term cyclability and high thermal stability of LiFePO4 in prismatic lithium-ion cells. *Journal of the Electrochemical Society,* 152(5), pp. A899-A904.

Templeton, G., 2015. *Accidental nanoparticles could let lithium ion batteries live another day.* [Online]
Available at: https://www.extremetech.com/extreme/212388-accidental-nanoparticles-

could-let-lithium-ion-batteries-live-another-day
[Accessed 10 11 2016].

Teng, H., 2012. Overview of the Development of the Fluoropolymer Industry. *Applied Sciences,* 2(2), pp. 496-512.

Terasawa, N., Ono, N., Hayakawa, Y., Mukai, K., Koga, T., Higashi, N. and Asaka, K., 2011. Effect of hexafluoropropylene on the performance of poly (vinylidene fluoride) polymer actuators based on single-walled carbon nanotube–ionic liquid gel. *Sensors and Actuators B: Chemical,* 160(1), pp. 161-167.

Teyssedre, G., Bernes, A. & Lacabanne, C., 1993. Influence of the crystalline phase on the molecular mobility of PVDF. *Journal of Polymer Science Part B: Polymer Physics,* 31(13), pp. 2027-2034.

Thostenson, . E., Ren, Z. & Chou, T., 2001. Advances in the science and technology of carbon nanotubes and their composites: a review.. *Composites science and technology,* 61(13), pp. 1899-1912.

Ueberreiter, K., 1968. The solution process. In: *Diffusion in polymers.* New York: Academic Press, pp. 219-257.

Viera, J., Gonzalez, M., Anton, J. & Campo, J., 2006. NiMH vs NiCd batteries under high charging rates.. *INTELEC 06-Twenty-Eighth International Telecommunications Energy Conference IEEE,* pp. 1-6.

Waldmann, T., Wilka, M., Kasper, M., Fleischhammer, M. and Wohlfahrt-Mehrens, M.., 2014. Temperature dependent ageing mechanisms in Lithium-ion batteries–A Post-Mortem study. *Journal of Power Sources,* Volume 262, pp. 129-135.

Wang, A., Huang, X. & Barsoum, M., 1992. Matrix crack initiation in ceramic matrix composites Part II: Models and simulation results. *Composites science and technology, ,* 44(3), pp. 271-282.

Wang, M., Le, A.V., Shi, Y., Noelle, D.J., Yoon, H., Zhang, M., Meng, Y.S. and Qiao, Y., 2016. Effects of angular fillers on thermal runaway of lithium-ion battery. *Journal of Materials Science & Technology.*

Wang, M.X., Liu, Q., Sun, H.F., Ogbeifun, N., Xu, F., Stach, E.A. and Xie, J., 2010. Investigation of carbon corrosion in polymer electrolyte fuel cells using steam etching. *Materials Chemistry and Physics,,* 123(2), pp. 761-766.

Wensley, C. G. & Chambers, K. D., 2010. *Battery separator for lithium polymer battery.* U.S., Patent No. 7,794,511. 14.

Whisnant, D., 2000. *Polymer Chemistry: Crystallization Tendency.* [Online] Available at: http://faculty.uscupstate.edu/llever/polymer%20Resources/Tendency.htm [Accessed 10 11 2016].

Wilson, K., 2013. *Automotive Industry Standards for the Safe Use of Lithium-Ion Battery Packs.* [Online]
Available at:
http://www.ntsb.gov/news/events/Documents/2013_Lithium_Batteries_FRM-Panel2e-Wilson.pdf
[Accessed 10 11 2016].

World Bank Group, 2012. Layered lithium transition metal oxide cathodes towards high energy lithium-ion batteries. *Journal of Materials Chemistry,* 5, 22(9), pp. 3680-3695.

Xia, L., Zhu, L., Zhang, H. & Ai, X., 2012. A positive-temperature-coefficient electrode with thermal protection mechanism for rechargeable lithium batteries. *Chinese Science Bulletin,* 57(32), pp. 4205-4209.

Yeow, K., Teng, H., Thelliez, . M. & Tan, E., 2012. 3D Thermal Analysis of Li-ion Battery Cells with Various Geometries and Cooling Conditions Using Abaqus. *2012 SIMULIA Community Conference.*

Yoshio, M., Brodd, R. J. & Kozawa, A., 2009. *Lithium-Ion Batteries - Science and Technologies. Vol. 1.* New York: Springer.

Yoshio, M., Brodd, R. J. & Kozawa, A., 2009. *Lithium-Ion Batteries. Vol. 1.* New York: Springer.

Zhang, S. S., 2007. A review on the separators of liquid electrolyte Li-ion batteries. *Journal of Power Sources,* 164(1), pp. 351-364.

Zhang, Z., Zeng, T., Lai, Y., Jia, M. and Li, J., 2014. A comparative study of different binders and their effects on electrochemical properties of LiMn2O4 cathode in lithium ion batteries. *Journal of Power Sources,* Volume 247, pp. 1-8.

Zheng, H., Li, J., Song, X., Liu, G. and Battaglia, V.S., 2012. A comprehensive understanding of electrode thickness effects on the electrochemical performances of Li-ion battery cathodes. *Electrochimica Acta,* Volume 71, pp. 258-265.

Zhong, H., Kong, C., Zhan, H., Zhan, C. and Zhou, Y., 2012. Safe positive temperature coefficient composite cathode for lithium ion battery. *Journal of Power Sources*, Volume 216, pp. 273-280.